

Locally Optimized B_1 Field for MRI Systems

BY

GIUSEPPE CARLUCCIO

Laurea Politecnico di Milano, Italy, 2005

Laurea Specialistica. Politecnico di Milano, Italy, 2010

Master of Science, University of Illinois at Chicago, IL, USA, 2011

THESIS

Submitted as partial fulfillment of the requirements
for the degree of Doctor of Philosophy in Electrical and Computer Engineering
in the Graduate College of the
University of Illinois at Chicago, 2011

Chicago, Illinois

Defense Committee:

Danilo Erricolo, Chair and Advisor

Rashid Ansari

Piergiorgio L. E. Uslenghi

Christopher M. Collins, Pennsylvania State University

Paolo F. Maccarini, Duke University

To my parents, who have always cared and supported me.

ACKNOWLEDGMENTS

First, I would like to thank Prof. Danilo Erricolo not only for all the helpful suggestions, all the guidance, all the mentorship that I have received since the start of my PhD program, but also because our collaboration showed me what team work means in the search of both solutions to technical problems and best words for publications.

I am extremely thankful to Prof. Christopher M. Collins for his kindness in welcoming me, for making possible all these projects and for spontaneously supporting my attendance to events useful to my integration in the MRI community.

I am also very grateful to Prof. Piergiorgio Uslenghi for the good suggestions for the development of the analytical solutions and to Prof. Rashid Ansari and Prof. Paolo Maccarini, my committee members.

In addition, thanks to all the Pennsylvania State University CNMRR group at Hershey, especially Prof. Qing X. Yang, Dr. Sukhoon Oh, Dr. Christopher Sica, Dr. Yeun Chul Ryu, Zhipeng Cao, Rahul Dewal, Ray Weiluo, Zachary Herse, who significantly helped me to develop my projects through intense discussions and who were always genuine friends.

GC

TABLE OF CONTENTS

<u>CHAPTER</u>	<u>PAGE</u>
1 PRINCIPLES OF MAGNETIC RESONANCE IMAGING.....	1
1.1 Introduction	1
1.2 MRI Overview	2
1.3 Physical principles of Magnetic Resonance.....	4
1.4 The FID signal	9
1.5 Hardware for MRI	17
1.6 Imaging Techniques	18
1.7 Some useful parameters	27
1.8 Sequences of RF pulses	30
2 RF COILS IN MRI.....	35
2.1 Introduction	35
2.2 The RF coils.....	35
2.3 The resonant circuits	36
2.4 The surface coil	38
2.5 The saddle coil.....	39
2.6 The birdcage coil	40
2.7 The phased array	46
3 2-D ANALYTICAL SOLUTIONS TO SIMPLIFY THE ANALYSIS OF THE B_1 FIELD DISTRIBUTION IN THE HEAD	50
3.1 Introduction	50
3.2 The circular 2-D model	50
3.3 The elliptic 2-D model	55
4 A FAST ANALYTICAL METHOD TO OPTIMIZE LOCAL TRANSMIT EFFICIENCY ...	68
4.1 Introduction	68
4.2 The locally optimized B_1 field	68
4.3 The optimization of the current phases.....	69
4.4 The optimization of the current amplitudes	70
4.5 Case 1: negligible mutual coupling	71
4.6 Case 2: mutual coupling non negligible	72
4.7 The parameter α	74
4.8 Evaluation of the algorithm	75
4.9 Comparisons using the parameter α	81
4.10 The factor C.....	83
5 A METHOD TO COMPUTE LOCAL AVERAGE SAR BASED ON ADAPTIVE SPHERICAL MASKS	85
5.1 Introduction	85
5.2 Safety requirements.....	85
5.3 The cubical average SAR	86
5.4 The spherical average SAR	89

TABLE OF CONTENTS

<u>CHAPTER</u>	<u>PAGE</u>
6 A FAST ALGORITHM TO COMPUTE TEMPERATURE INCREASE DUE TO SAR ABSORPTION	96
6.1 Introduction	96
6.2 SAR and temperature estimation	96
6.3 The low-pass filter	98
6.4 The low-pass filter applied to a simple geometry	100
6.5 The low-pass filter applied to more complex geometries.....	110
6.6 Conclusions.....	116
REFERENCES.....	119
VITA.....	129

LIST OF TABLES

<u>TABLE</u>	<u>PAGE</u>
1. GYROMAGNETIC RATIOS OF SOME NUCLEI. THE DIFFERENCE OF THESE VALUES CAN BE USED TO MAKE A SPECTROSCOPIC ANALYSIS.	5
2. MAGNITUDE OF THE B_1^+ FIELD PRODUCED BY THREE DIFFERENT CURRENT DISTRIBUTIONS INCLUDING OPTIMIZATIONS FOR AN ROI NEAR THE HEART AND IN THE SHOULDER FOR A TRANSMIT ARRAY HAVING NEGLIGIBLE COUPLING AMONG ITS ELEMENTS. IN EACH CASE THE TRANSMITTED POWER IS ABOUT 1KW.	77
3. MAGNITUDE OF THE B_1^+ FIELD PRODUCED BY THREE DIFFERENT CURRENT DISTRIBUTIONS INCLUDING OPTIMIZATIONS FOR AN ROI NEAR THE HEART AND IN THE SHOULDER FOR A TRANSMIT ARRAY HAVING NON NEGLIGIBLE COUPLING AMONG ITS ELEMENTS. IN EACH CASE THE TRANSMITTED POWER IS ABOUT 1KW.	79
4. MATERIAL PROPERTIES OF THE BODY TISSUES: PERFUSION BLOOD, MATERIAL DENSITY, HEAT CAPACITY, HEAT CONDUCTIVITY, HEAT OF METABOLISM.	99
5. VALUES OF THE OPTIMUM PARAMETERS OF THE FILTER FOR A TWO MINUTES HEATING TIME.	103

LIST OF FIGURES

<u>FIGURE</u>	<u>PAGE</u>
1. Casual orientation of the spins in absence of applied external magnetic field	5
2. Rotation and precession of the atoms in presence of an applied external magnetic field	6
3. Relation between the applied field and the difference in energy between the states.	8
4. Resulting magnetization vector as sum of the magnetic moment.	9
5. End of the equilibrium condition due to the effect of the RF signal	10
6. Rotation of the magnetization vector in the transverse plane, to be measured.....	11
7. RF pulses: (a) 90 degrees pulse. (b) 180 degrees pulse	12
8. Classical FID signal	13
9. 90 degrees RF pulse trajectory in the cartesian coordinates system (a) and in the rotating frame (b)	17
10. Sequence of signals for 1-D imaging	24
11. Sequence of pulses for back-projection imaging	25
12. (a) Acquisition of the projected signal along three different gradients. (b) Reconstruction of the object starting from the projection. Increasing the number of angles of projection, the image becomes more and more similar to the original.	26
13. Sequence of pulses for spin-warp imaging	27
14. Description of the k-space and its resolution	29
15. RF sequence for inversion recovery	31
16. RF sequence for spin-echo recovery	32
17. Temporal analysis of the magnetic moments in: (a) Application of the 90 degree pulse; (b) Rotation of the moments due the molecular interactions; (c) Application of the 180 degree pulse; (d) Rotation of the moments that return in phase.	33
18. Schematic of a resonant circuit	37
19. Schematic of a surface circuit	39
20. Schematic of a saddle circuit	40

LIST OF FIGURES(continued)

<u>FIGURE</u>	<u>PAGE</u>
21. Schematic of (a) Highpass Birdcage coil. (b) Lowpass Birdcage coil.....	41
22. Metallic cylinder with current $J_s = J_0 \sin \phi$	42
23. Transmission and reception in a quadrature system.....	46
24. Geometric representation of the circular cylindrical model.....	51
25. Expressions of the total electric field as series of Bessel functions inside the different materials of the circuit model.....	53
26. Elliptic Cylindrical coordinates.....	56
27. Expressions of the total electric field as series of Mathieu functions inside the different materials of the elliptical model.....	58
28. Comparison of the magnetic field computed by the analytical solution of the circular cylindrical model, the analytical solution of the elliptic cylindrical model, the numerical solution of the high fidelity model of the head.....	64
29. Geometry of the model used in simulations: a body-sized 8-element array of stripline elements spaced equidistantly on the surface of a cylinder within a large cylindrical shield and loaded with a human body model positioned with its heart near the center of the array.....	76
30. Plot of the amplitude of the impedance matrix of the transmit array in case of weak coupling (left) and strong coupling (right).....	77
31. Comparison of the spatial distribution of the magnetic field B_{1+} obtained with the transmit array having all the elements weakly coupled among them, and with the driving currents equal to the three compared methods. For the same location of interest, the three B_{1+} field distributions have been normalized so that the total generated power by the transmit array is the same.....	78
32. Comparison of the spatial distribution of the magnetic field B_{1+} obtained with the transmit array having all the elements strongly coupled among them, and with the driving currents equal to the three compared methods. For the same location of interest, the three B_{1+} field distributions have been normalized so that the total generated power by the transmit array is the same.....	79
33. Comparison of the maximum gain in percentage obtainable with the optimization of both amplitudes and phases respect the birdcage coil (a), and the phase-only optimization (b).	81

LIST OF FIGURES(continued)

<u>FIGURE</u>	<u>PAGE</u>
34. Percentage variation of the B1+ field (blue) and the generated power (red) respect to parameter α in eq. (4.18) for an optimized location close to the heart (a), and close to the arm (b).....	82
35. Plot of the variation of the cost function f respect to the parameter α for a location close to the heart. It is possible to see the improvement in the cost function when α becomes closer to 1 respect to the case of the phase-only optimization that corresponds to $\alpha=0$	83
36. Examples of averaging volumes. In the upper square the average SAR is calculated using the gray voxels and the calculated value is assigned to the center volume in black. In the middle square the average SAR is calculated using the cubical volume built around the black voxel and it is also assigned to the voxel in red because it is not possible to build a cubical volume centered in the red voxel and that does not have a boundary surface with at least one voxel internal to the body. In the bottom square the built volume is invalid because it has an external surface with no voxels internal to the body.	88
37. Examples of averaging volumes. In the upper volume center the average SAR is calculated using the gray voxels and the calculated value is assigned to the center volume in black. In the lower volume square the average SAR is calculated using the expanding spherical volume in the sample, built around the black voxel. In this way, we are able to adapt the mask of the object to the geometry of the sample, and each voxel of the sample is potentially a valid average SAR Volume Center.....	91
38. 3-D section of the spherical averaging mask applied on the border of a body tissue. The red voxels are used in the averaging method, while the external voxels in blue will be weighted if necessary, as explained in eq. (5.2), to reach the required n-grams averaging mass.	92
39. Geometry of the model used in simulations: a 16-element birdcage coil loaded with a cubical water sample positioned near the center of the volume coil.....	93
40. For a cube of water plots of (a) the 10 g averaged SAR distribution computed by XFDTD, (b) the 10 g averaged SAR distribution computed with the algorithm proposed in this Chapter based on spherical masks.	93
41. GUI of the SAR calculation tool with unaveraged SAR displayed and (right) detail of the displayed SAR data. Bottom: SAR distributions from the proposed method for 1g, 4.5g, and 10g averaged SAR as well as 10g average SAR calculated with the conventional cubical method.....	95
42. For a cube of water plots of (a) the 10 g averaged SAR distribution, (b) temperature increase calculated with an FD method (5 minutes heating time).	98

LIST OF FIGURES(continued)

<u>FIGURE</u>	<u>PAGE</u>
43. For a phantom cube, temperature increase distributions for a phantom having heat conductivity $k=0.6$ (a), and one with $k=2$ (b). Both temperature distributions have been computed with an FDTD solver for a 15 minutes heating time.	100
44. For a cube of water plots of (a) the unaveraged SAR distribution, (b) temperature increase calculated with a rigorous finite difference algorithm (15 minutes heating time), (c) 10 g average SAR distribution, (d) temperature increase calculated with the proposed rapid digital filter algorithm (15 minutes heating time).	104
45. Scheme of the determination of the transfer function to estimate Temperature profile from unaveraged SAR. Running only once the FD code allows obtaining a temperature profile. From the unaveraged SAR and the computed FD profile, it is possible to calculate the transfer function of the filter. Then, the obtained transfer function is used to estimate temperature profiles from several SAR profiles without to run again the FD code.....	105
46. For a box of water, starting from four unaveraged SAR distributions (a), the corresponding 10 g average SAR distributions (b), the temperature increase calculated with a rigorous finite difference algorithm (15 minutes heating time) (c), temperature increase calculated with the proposed rapid digital filter algorithm (15 minutes heating time) (d).	107
47. For a sphere of water, starting from four unaveraged SAR distributions (a), the corresponding 10 g average SAR distributions (b), the temperature increase calculated with a rigorous finite difference algorithm (15 minutes heating time) (c), temperature increase calculated with the proposed rapid digital filter algorithm (15 minutes heating time) (d).	108
48. For a box of water, plots of temperature distributions with 15 minutes heating time (a), and with 5 minutes heating time (b).The strong difference between them does not allow to find one single filter for both.....	109
49. For a quadrature surface about the occipital lobe, plots of (a) the unaveraged SAR distribution, (b) temperature increase calculated with a rigorous finite difference algorithm (1 hour heating time), (c) 10 g average SAR distribution, (d) temperature increase calculated with the filtered SAR without blood perfusion rate contribution (1 hour heating time).	111
50. For a quadrature surface about the occipital lobe, plots of (a) the unaveraged SAR distribution, (b) temperature increase calculated with a rigorous finite difference algorithm (1 hour heating time), (c) 10 g average SAR distribution, (d) temperature increase calculated with the filtered SAR without blood perfusion rate contribution (1 hour heating time).	115

LIST OF ABBREVIATIONS

BOLD	Blood Oxygenation Level-Dependent
CAT	Computer Axial Tomography
DP	Protonic Density
FID	Free Induction Decay
FOV	Field of View
FT	Fourier Transform
FFT	Fast Fourier Transform
IEC	International Electrotechnical Commission
LPF	Low-Pass Filter
MRI	Magnetic Resonance Imaging
NMR	Nuclear Magnetic Resonance
RF	Radiofrequency
SAR	Specific Absorption Rate
SNR	Signal to Noise Ratio

SUMMARY

A current challenge for high-field Magnetic Resonance Imaging Systems is the non-uniformity of the excitation B_1 RF magnetic field. This is a particular problem because at high magnetic fields the required B_1 field has a relatively short wavelength. A superposition of fields from different sources or current elements results in standing waves that causes a non-uniform excitation and ultimately affects the quality of the final images.

Optimization of the currents in transmit arrays is nowadays the most common way to compensate the inhomogeneities of the magnetic field distribution, and highly homogeneous fields have been obtained at high operating frequencies in the brain. However, it is not always possible to achieve high homogeneity of the B_1 distribution and low Specific Absorption Rate, which is a necessary condition to not overheat the patient. These requirements are specifically hard to satisfy in tissues having large cross-sections such as the torso or the abdomen. For these regions it is suggested to reduce the region of interest, focusing on only one localized volume, with a diameter comparable with half-wavelength in the medium. We present in this thesis an analytical method able to provide the best set of currents to optimize the transmit efficiency of the transmit array for a desired small region of interest, maximizing the transmitted field strength and minimizing the total power generated by the array, which is an upper bound to the maximum power absorbed by the patient.

In addition, this thesis presents a new method helpful to compute the Pennes' bioheat equation, which is the most used relation between temperature increase in body tissues and Specific Absorption Rate, based on the sequential application of a filter in the spatial frequency domain. The main advantage of this method is to provide results very similar to the ones obtained with rigorous methods based on Finite Difference analysis but in an extremely short computation

SUMMARY(continued)

time, resulting in a very helpful tool in optimization algorithms based on the designs of transmit arrays satisfying safety requirements.

Furthermore, in this thesis are also presented (1) two 2-D analytical solutions able to rapidly compute the distribution of both the electric and the magnetic fields in lossy cylinders having circular and elliptic bases are provided in the presence of a wide variety of excitation sources; and (2) a new method to compute local average Specific Absorption Rate using adaptive spherical masks which provide higher accuracy respect to the methods implemented in numerical electromagnetic simulators for biological applications.

CHAPTER 1

PRINCIPLES OF MAGNETIC RESONANCE IMAGING

1.1 Introduction

Nowadays Magnetic Resonance Imaging (MRI) is one of the most useful diagnostic imaging tools in medicine: it can provide high resolution images with high contrast, spectroscopic analyses, spatial distribution of several parameters allowing different approaches to the diagnosis of the disease, and it is non invasive.

An MRI system is composed of a strong magnet able to create a continuous magnetic field B_0 to align the atomic spins and create a net magnetization vector. Through the use of Radiofrequency (RF) coils operating at the Larmor frequency (proportional to the field B_0 applied) through the generation of the so called B_1 RF magnetic field it is possible to detect a signal containing information about the inspected tissue: with post-processing techniques we can then obtain the final images. In this dissertation some physical principles of an MRI system, the equations that describe the resonance condition and the basic techniques to obtain images are described in **Chapter 1**, while the design of the RF coils most commonly used in MRI systems, the birdcage coils, is described in **Chapter 2**. In addition, the dependence of the inhomogeneities of the B_1 field at the increase of B_0 has been shown in detail.

Currently, research is focused on using stronger magnetic fields B_0 to obtain higher resolution images and higher SNR. Higher B_0 fields lead to higher Larmor frequencies, and consequently the RF field B_1 has a relatively short wavelength, compared with the size of human tissues. A superposition of such fields from different sources or current elements creates a non uniform distribution of the fields and ultimately affects the quality of the final images. RF shimming is a

promising technique to solve this challenge: applying concepts of antenna array theory, it suggests to control separately the currents in the elements of the MRI RF coils like in a transmit array to obtain a desired magnetic field B_1 distribution.

The goal of the first applications of RF shimming techniques was to obtain higher B_1 homogeneity. In regions of the body that have large cross-sections, such as torso or abdomen, where it is hard to obtain homogeneous excitation field and to keep low SAR levels, it is more advantageous to do RF shimming over a volume smaller than the total volume of the sample. Starting from an analysis of the position of the peaks of B_1 field presented in **Chapter 3** with the aid of two simplified 2-D analytical models, one with a circular infinite cylinder and one for an elliptic base cylinder, in **Chapter 4** we propose a fast method to control the inhomogeneity of the B_1 field, increasing the value of the B_1 field in a specific location while minimizing the generated power, which may cause overheating and may damage some tissues. There are, in fact, safety policies that regulate the RF power absorption by body tissues defined in terms of the Specific Absorption Rate (SAR) and consequent maximum temperature increase. In **Chapter 5** we presented a new method to estimate average absorbed SAR, parameter present in safety regulations, while in **Chapter 6** we focused on temperature increase in body tissues by RF power absorption, proposing a new algorithm able to drastically speed up computation of temperature increase given the SAR distribution and the geometry of the body.

1.2 MRI Overview

MRI is a technique used mainly in the medical field to obtain high definition images of the internal tissues of human body. MRI is based on the principles of Nuclear Magnetic Resonance (NMR)[1], a spectroscopic technique that is used to obtain information about the microscopic chemical and physical structure of the molecules.

MRI is based on the analysis of the response of the nuclei due to an external RF excitation having frequency equal to the precessional frequency of the nuclei, and each nucleus has a different

precessional frequency. Commonly the chosen operating frequency is the one that excites hydrogen atoms, because they are the most abundant elements in human tissue [64], not only as part of water molecules but they are also present in larger organic molecules as lipids and proteins.

An MRI system can be used even to do spectroscopic analysis: the main difference between spectroscopy and the classical MRI image is that in spectroscopy not only hydrogen protons are excited, but using different excitation frequencies are examined also signals coming from other elements that are present in the human body, which are called metabolites. In MRI the intensity of the signal gives the information about the concentration of hydrogen atoms in each unit volume, in spectroscopy the intensity of the signal at different precessional frequencies indicates which chemical elements (H, P, Na, ...) are present in a unit volume. This can be obtained examining the frequency spectrum distribution of the detected signals, because each element has a different excitation frequency.

An MRI system is mainly composed of a magnet able to create a strong continuous magnetic field, some gradient coils to excite atoms that have different spatial position with a slightly different frequency, and some RF coils operating at the resonance frequency of the nuclei. To obtain a clear image, a series of events have to be adequately controlled, from the alignment of the magnetic moments to the excitation sequence by the RF signal, from the filtering of the received signal to conversion to digital signal to be reconstructed by computers, etc.

There are several reasons why magnetic resonance is becoming so popular nowadays in medical fields: unlike diagnosis techniques based on X-rays (CAT for example), MRI does not use ionized radiations and so it does not damage directly the human tissues. In addition, with MRI it is easy to discern different tissues, obtaining very high contrast images, because there are several parameters that affect the final image, and so it is even possible to have additional information that can be specific and useful for the recognition of pathologies. Besides, with some computer post

processing, it is possible to reconstruct MRI images taken on different planes of the patient, without to ask him to be repositioned, obtaining a 3D analysis of the sample.

Even if MRI has, with no doubts, several advantages and it is non-invasive, there are some risks linked to the use of the MRI hardware: the presence of some metallic material inside the patient (pacemakers or prostheses for example) can dangerously interact with the strong continuous magnetic field being attracted by that, and can even interact with the RF fields because they can induce surface currents on the metallic plates, and consequently dissipation of power and temperature increase. In addition MRI hardware cannot interact with other electric machines that are close to the scanner: in other words it has to satisfy several Electromagnetic Compatibility tests before being used.

1.3 **Physical principles of Magnetic Resonance**

The NMR is mainly based on the physical properties of the nuclei of atoms, which are made by protons and neutrons and can be considered as small electrically charged spheres rotating on their own axis, according to the value of the spin quantum number. This rotation movement makes them similar to small magnets with their magnetic moments. Consequently, an angular momentum ρ can be associated to each nucleus given by:

$$\rho = \frac{h}{2\pi} I \quad (1.1)$$

where h is the Plank constant and I is the spin quantum number. Since the nucleus is associated with an electric charge, it generates a magnetic dipole moment μ :

$$\mu = \gamma \rho \quad (1.2)$$

where γ is called gyromagnetic ratio and it is a characteristic of each nucleus.

Element	symbol	$\frac{\gamma}{2\pi}$ (MHz/T)
Hydrogen	^1H	42.575
Carbon	^{13}C	10.7
Fluorine	^{19}F	40.05
Sodium	^{23}Na	11.26
Phosphorus	^{31}P	17.235

Table 1.1: Gyromagnetic ratios of some nuclei. The difference of these values can be used to make a spectroscopic analysis.

In absence of an external magnetic field, there is no energy difference between the spin levels: hence, the direction of the magnetic axes of the nuclei is random as we can see in Fig. 1.1.

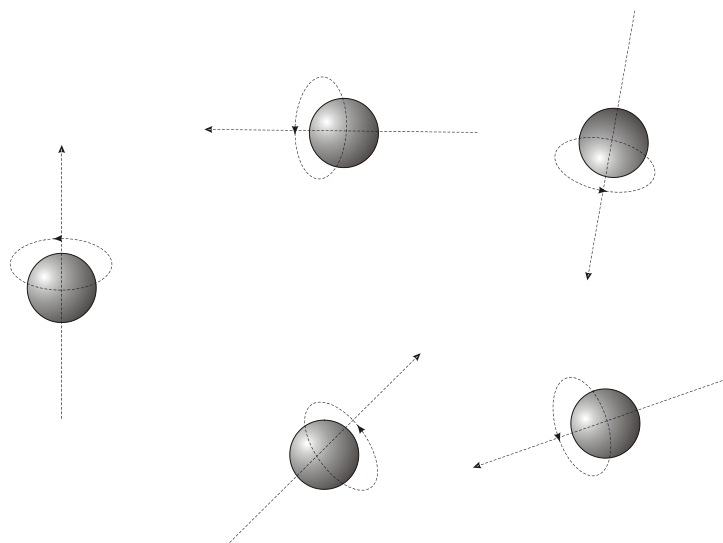


Figure 1.1: Casual orientation of the spins in absence of applied external magnetic field

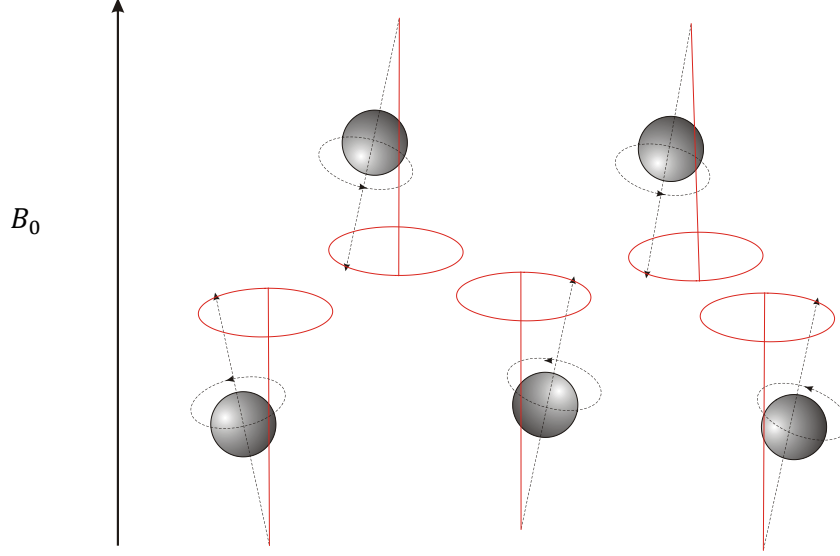


Figure 1.2: Rotation and precession of the atoms in presence of an applied external magnetic field

On the contrary, if we apply a constant magnetic field B_0 , the nuclear magnetic moments rotate around an axis that is aligned with the main magnetic field. This movement of the nuclei is called “precession”, and it is similar to the one of a spinning top around its axis. The frequency of the precession rotation is given by the Larmor equation

$$\omega_0 = \gamma B_0 \quad (1.3)$$

and it is called Larmor frequency.

Let us analytically justify what has been described up to now. Each atom has a magnetic moment $\boldsymbol{\mu}$; let us assume that the initial condition of the magnetic moment is:

$$\boldsymbol{\mu}(0) = \hat{x}\mu_{x0} + \hat{y}\mu_{y0} + \hat{z}\mu_{z0} \quad (1.4)$$

The torque due to the magnetic field is given by

$$\boldsymbol{\tau} = \boldsymbol{\mu} \times \mathbf{B}_0 \quad (1.5)$$

and $\boldsymbol{\tau}$ is related to the definition of angular momentum by

$$\boldsymbol{\tau} = \frac{d\boldsymbol{\rho}}{dt} \quad (1.6)$$

Equating the two previous equations yields

$$\frac{d\boldsymbol{\mu}}{dt} = \gamma(\boldsymbol{\mu} \times \mathbf{B}_0) \quad (1.7)$$

Assuming \mathbf{B}_0 is parallel to the z axis we can write:

$$\frac{d\mu_x}{dt} = \gamma\mu_y B_0 \quad (1.8a)$$

$$\frac{d\mu_y}{dt} = -\gamma\mu_x B_0 \quad (1.8b)$$

$$\frac{d\mu_z}{dt} = 0 \quad (1.8c)$$

From (1.8a) and (1.8b) we obtain :

$$\frac{d^2}{dt^2} \begin{pmatrix} \mu_x \\ \mu_y \end{pmatrix} + (\gamma B_0)^2 \begin{pmatrix} \mu_x \\ \mu_y \end{pmatrix} = 0 \quad (1.9)$$

Using the previous initial conditions, the solution of this differential equation is:

$$\boldsymbol{\mu}(t) = \hat{\mathbf{x}}(\mu_{x0} \cos \omega t + \mu_{y0} \sin \omega t) + \hat{\mathbf{y}}(\mu_{y0} \cos \omega t - \mu_{x0} \sin \omega t) + \hat{\mathbf{z}}\mu_{z0} \quad (1.10)$$

where $\omega = \gamma B_0$ as in (1.3). The precession movement is given by the time-variation of $\boldsymbol{\mu}(t)$.

Fig. 1.2 shows that, once an external field is applied, two orientations of the nuclei are allowed: one parallel (up) and one antiparallel (down) depending on the energy level of the nuclei[44, 105]: the difference in energy between the two states is linearly proportional to the intensity of the applied magnetic field

$$\Delta E = \frac{\gamma h}{2\pi} B_0. \quad (1.11)$$

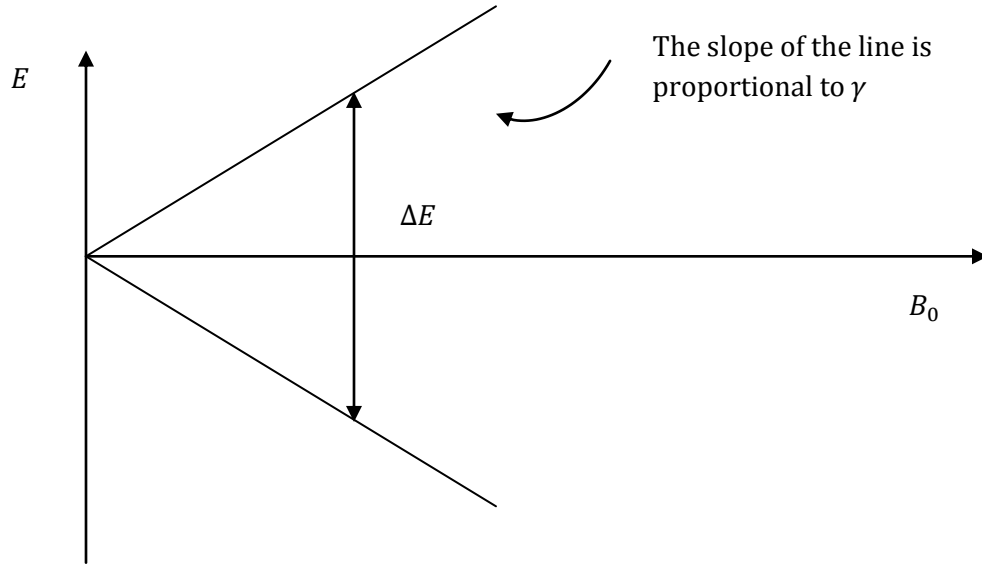


Figure 1.3: Relation between the applied field and the difference in energy between the states.

At thermal equilibrium the number of nuclei that belong to the higher energy level is smaller than the number of the atoms belonging to the lower, and the distribution of the atoms in the two levels is given by the Boltzmann statistics:

$$\frac{N_{up}}{N_{down}} = e^{-\frac{\Delta E}{kT}} \quad (1.12)$$

It is interesting to notice that, since ΔE is proportional to B_0 , increasing the value of B_0 we increase the difference in population of the two energy levels. Since each atom has a magnetic dipole moment, and the moment is parallel to B_0 , we obtain the macroscopic value of the net magnetization M_0 summing all the dipole moments:

$$M_0 = \sum \mu = \mu(N_{down} - N_{up}) \quad (1.13)$$

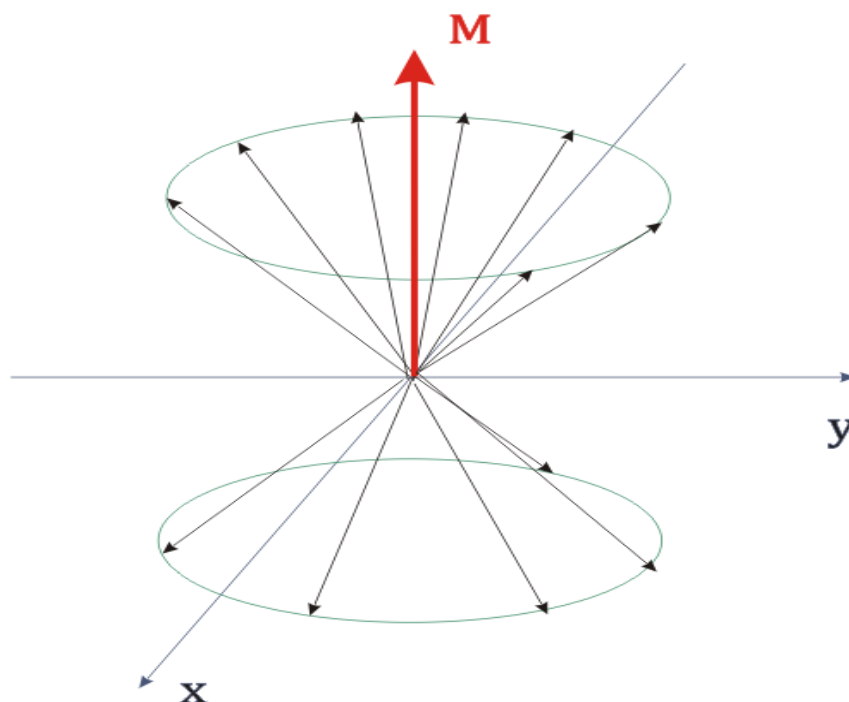


Figure 1.4: Resulting magnetization vector as sum of the magnetic moments

Therefore, by increasing the value of B_0 we produce a larger value of the net magnetization M_0 with a consequent stronger useful signal for the images.

However, since the vector M_0 is parallel to the strong field B_0 , it is very difficult to measure because M_0 is much smaller than the field B_0 . One way to measure M_0 is to re-orient it so that it is no longer parallel to B_0 and this is discussed next.

1.4 The FID signal

The term "resonance" refers to a physical phenomenon where two systems are able to exchange energy, and that happens with higher efficiency when their structural affinity is high, or in other words they are closer to the resonance condition. In the case of magnetic resonance, the system that receives energy is represented by the nuclei of the inspected object aligned with the

magnetic field B_0 , and the system that gives energy is represented by the RF magnetic field called B_1 .

The resonance condition occurs when the frequency of the field B_1 is the same as the Larmor frequency of the excited atoms. After the nuclei acquire energy from the RF field, they are not in thermal equilibrium. Referring to Fig. (1.5), the B_1 field is oriented orthogonal to the z-axis: in this condition B_1 is able to rotate the magnetization vector M . The longitudinal net magnetization decreases since the B_1 field changes the direction of the net magnetization from the direction of the B_0 field to the B_1 field direction: now we are in a condition of transversal net magnetization. The intensity and the length of the B_1 field (RF pulse) determine the so called “flip angle”, that is the angle of the precession movement.

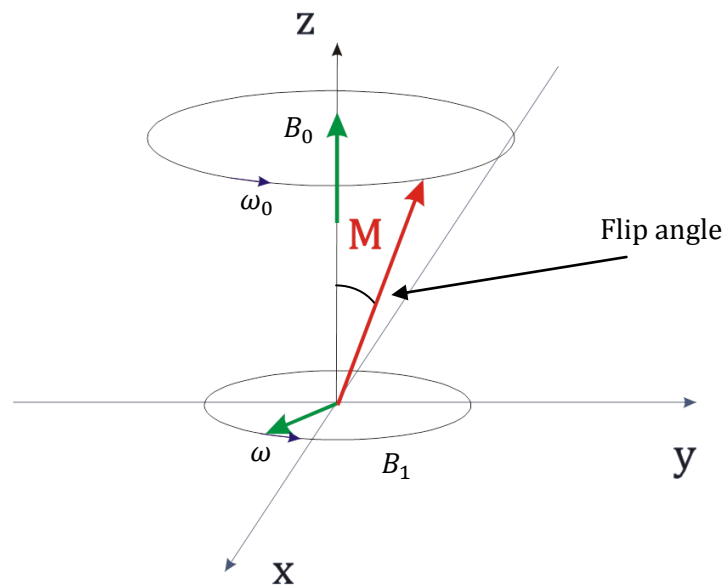


Figure 1.5: End of the equilibrium condition due to the effect of the RF signal

When we are in the condition that the magnetization vector lies completely in the B_1 plane, the pulse is called “90 degree pulse”, because it causes a sinusoidal rotation of the magnetization vector of 90 degrees (for example if before the direction was the z axis, now it is the xy plane). Now that M is in a plane perpendicular to the one of B_0 , it is possible to measure M with an antenna: the analyzed RF signal at Larmor frequency is called Free Induction Decay (FID). A “180 degree pulse”, instead, makes an inversion of the vector M : in other words, at the end of the pulse M is oriented parallel to the z axis but pointing in opposite direction.

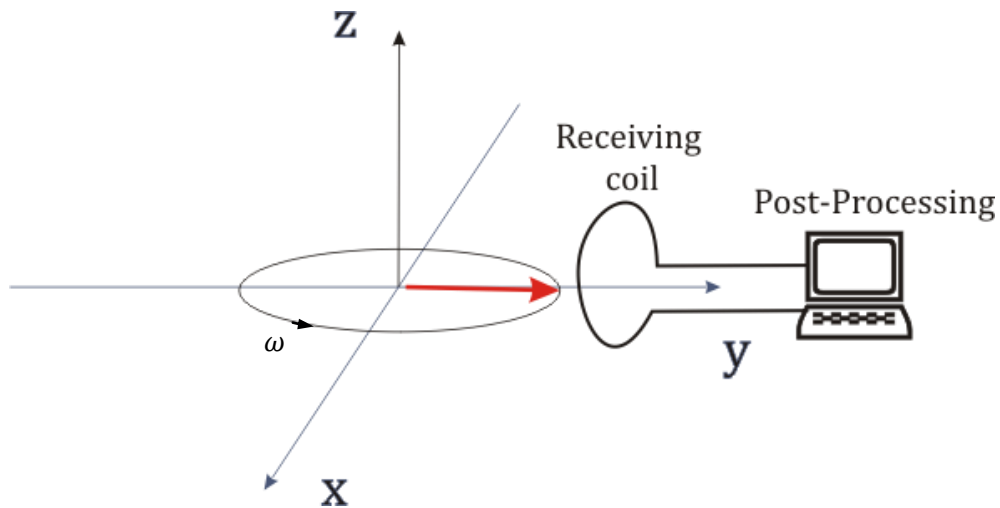


Figure 1.6: Rotation of the magnetization vector in the transverse plane, to be measured

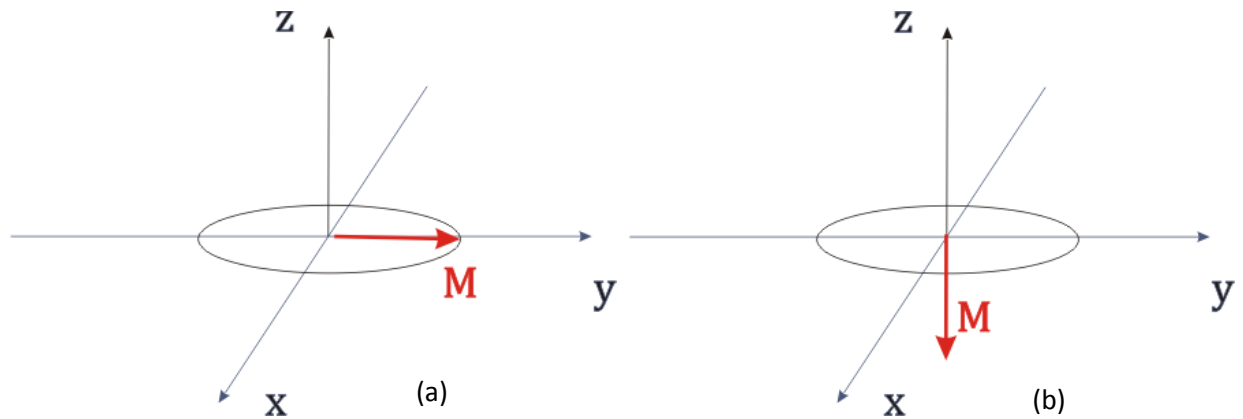


Figure 1.7 RF pulses: (a) 90 degrees pulse. (b) 180 degrees pulse

At the end of the pulses, through a relaxation process, the system tends to return to the original condition of thermal equilibrium. Since the hydrogen nuclei (the most used) belong to different molecular structures, they will have different ways to release the acquired energy, depending on the interactions of each hydrogen nucleus with the surrounding atoms which are different for different tissues. These differences are quantifiable using some characteristic MRI parameters: the proton density (DP), the relaxation time T_1 and the relaxation time T_2 .

The proton density is the quantity of the resonant hydrogen protons per unitary volume (voxel), and it is responsible for the amplitude of the detected signal. The relaxation times T_1 and T_2 represent respectively the time necessary to have the 63% of the original value of the projection of M_0 on the z axis (M_z) after an RF pulse and the time after which the transverse magnetization decreases of a factor e : commonly T_1 is longer than T_2 and this depends only by the molecular structure where the protons are situated (T_1 and T_2 are similar only in pure liquids). T_1 describes the tendency of a system to realign the direction of the magnetization vector M to the original z-axis direction, while T_2 describes the decay of the transverse component of the magnetization vector M : in the transverse plane, each nucleus is affected by the magnetic field of surrounding nuclei, causing

the loss of coherency among the signals coming from each atom. For this reason, after relaxation occurs, the signal becomes dephased. In addition, another source of dephasing is due to the inhomogeneities of the field \mathbf{B}_0 , and the parameter T_2^* includes also the dephasing caused by the inhomogeneity of the static field.

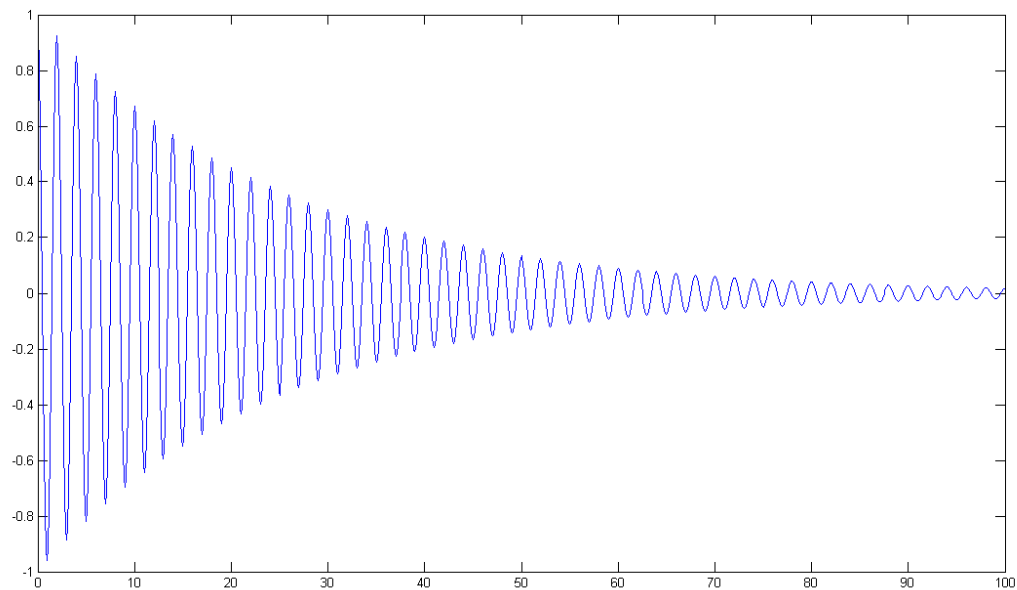


Figure 1.8: Classical FID signal

Analysis of the relaxation times is important because it provides the key to increase the contrast between different tissues, or to recognize some pathologies: for example, relaxation times are different in healthy tissues and tissues affected by cancer.

Let us derive analytically the Bloch equations that describe the movement of the net magnetization vector [29, 101]. Since $\mathbf{M} = \sum \boldsymbol{\mu}$, all the previous relations found for the magnetic moment ($\frac{d\boldsymbol{\mu}}{dt} = \gamma(\boldsymbol{\mu} \times \mathbf{B}_0)$) are valid for the net magnetization

$$\frac{d\mathbf{M}}{dt} = \gamma \mathbf{M} \times \mathbf{B} = \gamma \det \begin{pmatrix} i & j & k \\ M_x & M_y & M_z \\ B_x & B_y & B_z \end{pmatrix}, \quad (1.14)$$

$$\frac{d\mathbf{M}}{dt} = \gamma \left(\hat{x}(M_y B_z - M_z B_y) + \hat{y}(M_z B_x - M_x B_z) + \hat{z}(M_x B_y - M_y B_x) \right). \quad (1.15)$$

Let us first examine the case where just the constant field \mathbf{B}_0 is applied: we can easily see that it is equivalent to the precession movement, because $\mathbf{M} = \sum \boldsymbol{\mu}$, and we already studied what happens to the single magnetic moment $\boldsymbol{\mu}$ when we apply the field \mathbf{B}_0 .

Let us consider now the case where:

$$\mathbf{B} = \mathbf{B}_0 + \mathbf{B}_1 = \begin{pmatrix} B_x \\ B_y \\ B_z \end{pmatrix} = \begin{pmatrix} B_1 \cos \omega t \\ B_1 \sin \omega t \\ B_0 \end{pmatrix} \quad (1.16)$$

Substituting the relation (1.16) in equation (1.15) we have

$$\begin{aligned} \frac{dM_x}{dt} &= \gamma(M_y B_0 - M_z B_1 \sin \omega t), \\ \frac{dM_y}{dt} &= \gamma(M_z B_1 \cos \omega t - M_x B_0), \\ \frac{dM_z}{dt} &= \gamma(M_x B_1 \sin \omega t - M_y B_1 \cos \omega t). \end{aligned} \quad (1.17)$$

To be more accurate, to the previous relations we need to add the relaxation terms that influence the exponential decay of each component, due to the interactions among the atoms, after the application of a RF B_1 field, obtaining:

$$\begin{aligned}
\frac{dM_x}{dt} &= \gamma(M_y B_0 - M_z B_1 \sin \omega t) - \frac{M_x}{T_2} \\
\frac{dM_y}{dt} &= \gamma(M_z B_1 \cos \omega t - M_x B_0) - \frac{M_y}{T_2} \\
\frac{dM_z}{dt} &= \gamma(M_x B_1 \sin \omega t - M_y B_1 \cos \omega t) - \frac{(M_z - M_0)}{T_1}
\end{aligned} \tag{1.18}$$

With the relations (1.18), in theory it is possible to have a complete description of the movement of the magnetization vector, but it is not the easiest way to approach the problem. It is much easier to rewrite (1.18) in a new different reference frame called the rotating frame, where the axes rotate with an angular frequency ω . This can be described mathematically as:

$$\begin{aligned}
\mathbf{x}' &= \frac{\partial \hat{\mathbf{x}}}{\partial t} = \omega \times \hat{\mathbf{x}}, \\
\mathbf{y}' &= \frac{\partial \hat{\mathbf{y}}}{\partial t} = \omega \times \hat{\mathbf{y}}, \\
\mathbf{z}' &= \frac{\partial \hat{\mathbf{z}}}{\partial t} = \omega \times \hat{\mathbf{z}},
\end{aligned} \tag{1.19}$$

where $\hat{\mathbf{x}} = \mathbf{x}' / \|\mathbf{x}'\|$, $\hat{\mathbf{y}} = \mathbf{y}' / \|\mathbf{y}'\|$, $\hat{\mathbf{z}} = \mathbf{z}' / \|\mathbf{z}'\|$ represent the unit vectors of the axes of the rotating frame.

The time derivative of the vector \mathbf{M} in terms of the rotating system must be written as

$$\begin{aligned}
\frac{d\mathbf{M}}{dt} &= \frac{\hat{\mathbf{x}} dM_x}{dt} + \frac{\hat{\mathbf{y}} dM_y}{dt} + \frac{\hat{\mathbf{z}} dM_z}{dt} + M_x \frac{\partial \hat{\mathbf{x}}}{\partial t} + M_y \frac{\partial \hat{\mathbf{y}}}{\partial t} + M_z \frac{\partial \hat{\mathbf{z}}}{\partial t} \\
&= \frac{\partial \mathbf{M}}{\partial t} + \omega \times (M_x \hat{\mathbf{x}} + M_y \hat{\mathbf{y}} + M_z \hat{\mathbf{z}}) \\
&= \left(\frac{\partial \mathbf{M}}{\partial t} \right)_{\text{rotating}} + \omega \times \mathbf{M} = \gamma \mathbf{M} \times \mathbf{B}
\end{aligned} \tag{1.20}$$

In the previous expression,

$$\left(\frac{\partial \mathbf{M}}{\partial t}\right)_{rotating} = -\omega \times \mathbf{M} + \gamma \mathbf{M} \times \mathbf{B} = \gamma \mathbf{M} \times \mathbf{B} - \gamma \mathbf{M} \times \frac{\omega}{\gamma} = \gamma \mathbf{M} \times \left(\mathbf{B} - \frac{\omega}{\gamma}\right) \quad (1.21)$$

Since we are in a rotating frame, our \mathbf{B} field ($\mathbf{B} = B_1 \cos(\omega t) \hat{\mathbf{x}} + B_1 \sin(\omega t) \hat{\mathbf{y}} + B_0 \hat{\mathbf{z}}$) can be rewritten as

$$\mathbf{B}_{rot} = B_0 \hat{\mathbf{z}} + B_1 \hat{\mathbf{x}}. \quad (1.22)$$

If we are in a condition of resonance ($\omega = \gamma B_0$), things simplify a lot because

$$\begin{aligned} \left(\frac{\partial \mathbf{M}}{\partial t}\right)_{rotating} &= \gamma \mathbf{M} \times \left(\mathbf{B}_0 - \frac{\omega}{\gamma} + \mathbf{B}_1\right) = \gamma \mathbf{M} \times \mathbf{B}_1 \\ &= \gamma \det \begin{pmatrix} i & j & k \\ M_x & M_y & M_z \\ B_1 & 0 & 0 \end{pmatrix} \end{aligned} \quad (1.23)$$

$$\begin{aligned} \frac{dM_x}{dt} &= 0 \\ \frac{dM_y}{dt} &= \gamma(M_z B_1) \\ \frac{dM_z}{dt} &= \gamma(-M_y B_1) \end{aligned} \quad (1.24)$$

Since our initial condition is that \mathbf{M} is parallel to the z axis, the solution of the (1.24) is

$$M_y = M_z \sin(\gamma B_1 t) \quad (1.25)$$

We can easily see that there is a rotation from the z axis toward the y axis with an angle of rotation given by:

$$\theta = \gamma B_1 t \quad (1.26)$$

According to the duration of the RF pulse B_1 , it is possible to obtain a rotation of the magnetization vector of 90, 180, ... degrees. As we saw before, the case with $\theta = 90^\circ$ is very

important because it leads to a rotation of the vector \mathbf{M} in the xy plane, and so it is easier to detect because it is orthogonal to the strong applied magnetic field \mathbf{B}_0 .

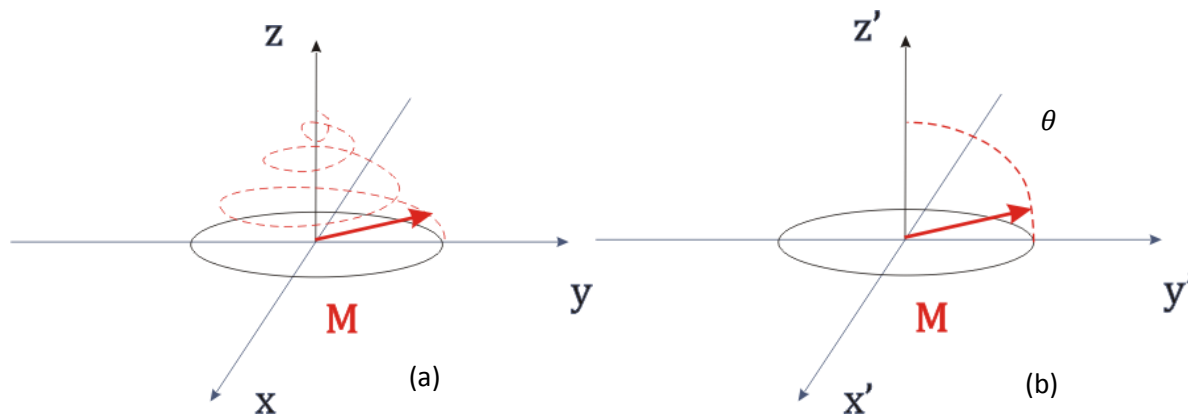


Figure 1.9 90 degrees RF pulse trajectory in the cartesian coordinates system (a) and in the rotating frame (b)

1.5 Hardware for MRI

Let us now analyze briefly the components that are the fundamental for an MRI system.

The static magnet is the main component of an MRI system: it has to generate a magnetic field of a proper intensity, with high homogeneity and stability in time: homogeneity is fundamental because with low homogeneity we have low quality images since the protons are not excited uniformly, and that corresponds to a slightly different resonance frequency, and consequently to a different excitation in terms of flip angle. There are several types of magnets, the most common are:

- Permanent magnet: it is built with several blocks with high magnetic hysteresis, so that, once they are excited, they keep constant the magnetic field for an indefinite time: this guarantees low maintenance costs because they do not need electric current to operate. The low cost is paid in terms of low intensity and homogeneity of the generated fields.

- Resistive magnet: it is comparable to an electromagnet, made with a coil with a high intensity current. The main problem of this magnet is the high quantity of generated heat due to the current. It requires a lot of energy and it cannot produce high magnetic fields.
- Superconducting magnet: it is built with materials that operate at temperatures close to 0 K. This leads to very low resistances in the coils, allowing circulation of very high currents without high dissipation of energy: these high currents can create very strong magnetic fields.
- Hybrid magnet: magnet created using the technologies relative to permanent and resistive magnets.

Shimming magnets are coils that are used to increase homogeneity of the static magnetic field. They can be made either during the construction of the magnets to reduce the nonhomogeneities of the magnet, or using proper coils inside the system[40].

The RF coils are the antennas that are used to transmit and to detect the oscillating fields: they will be discussed more deeply in the next chapter.

The gradient coils are used to alter the spatial and temporal homogeneity of the B_0 field. They are positioned along the x , y and z axes around the magnet and they can be used to recognize the position of a voxel and, consequently, to reconstruct the image.

Lastly, a computer controls each component of the MRI system, the RF pulse sequences, the gradient coils, and it reconstructs the images from the received signals.

1.6 Imaging Techniques

Up to now we just examined the behavior of the magnetization vector of a single voxel, now we should examine how the magnetization vector behaves in different spatial voxels, and from these differences how to reconstruct the spatial distribution of the materials of each voxel in one image, as suggested in [10].

First of all, let us write the solution of the Bloch equation referred to the transverse plane as

$$M_{xy}(\mathbf{r}, t) = M_x(x, y, z, t) + i M_y(x, y, z, t), \quad (1.27)$$

where \mathbf{r} indicates the space position. Now, let us apply with the gradient coils a variable magnetic field oriented in the z direction

$$\mathbf{B}(\mathbf{r}, t) = (B_0 + \Delta B(\mathbf{r}, t))\hat{\mathbf{z}} \quad (1.28)$$

The Bloch equation relative to the xy component can be written as

$$\frac{dM_{xy}(\mathbf{r}, t)}{dt} = \left(-i\gamma(B_0 + \Delta B(\mathbf{r}, t)) + \frac{1}{T_2(\mathbf{r})} \right) M_{xy}(\mathbf{r}, t) \quad (1.29)$$

With $M_{xy}(\mathbf{r}, 0) = M_0(\mathbf{r})$, we have as solution:

$$M_{xy}(\mathbf{r}, t) = M_0(\mathbf{r}) e^{-i\omega t} e^{-\frac{t}{T_2(\mathbf{r})}} e^{-i\gamma \int_0^t \Delta B(\mathbf{r}, t') dt'} \quad (1.30)$$

In the rotating frame this equation can be rewritten as

$$M_{x'y'}(\mathbf{r}, t) = M_0(\mathbf{r}) e^{-\frac{t}{T_2(\mathbf{r})}} e^{-i\gamma \int_0^t \Delta B(\mathbf{r}, t') dt'} \quad (1.31)$$

It is important to notice that time t starts after the application of a 90 ° RF pulse, when the magnetization vector has been brought in the transverse plane.

Now, let us consider the case of a spatial time invariant gradient G_x , in the x direction:

$$\Delta B(\mathbf{r}, t) = G_x \cdot \hat{\mathbf{x}} \quad (1.32)$$

the solution of the Bloch equation is then:

$$M_{xy}(\mathbf{r}, t) = M_0(\mathbf{r}) e^{-i\omega_0 t} e^{-\frac{t}{T_2(\mathbf{r})}} e^{-i\gamma G_x x t} = M_0(\mathbf{r}) e^{-i\omega_0 t} e^{-\frac{t}{T_2(\mathbf{r})}} e^{-i\gamma \Delta\omega(x) t} \quad (1.33)$$

where we can see the presence of a spatial difference of the resonance excitation frequency of the spins in the x direction ($\Delta\omega(x) = \gamma G_x x$).

Generalizing to the case of a gradient along an arbitrary direction, the relation between the frequency and the position is $\Delta\omega(\mathbf{r}) = \gamma \mathbf{G} \cdot \mathbf{r}$ and the solution of the Bloch equation is:

$$M_{xy}(\mathbf{r}, t) = M_0(\mathbf{r}) e^{-i\omega_0 t} e^{-\frac{t}{T_2(\mathbf{r})}} e^{-i\gamma \Delta\omega(\mathbf{r}) t} \quad (1.34)$$

Lastly, we can have a time varying gradient $\Delta\omega(\mathbf{r}, t) = \gamma \mathbf{G}(t) \cdot \mathbf{r}$ having as Bloch equation:

$$M_{xy}(\mathbf{r}, t) = M_0(\mathbf{r})e^{-i\omega_0 t}e^{-\frac{t}{T_2(\mathbf{r})}}e^{-i\gamma\Delta\omega(\mathbf{r}, t)t} = M_0(\mathbf{r})e^{-i\omega_0 t}e^{-\frac{t}{T_2(\mathbf{r})}}e^{-i\phi(\mathbf{r}, t)t} \quad (1.35)$$

where $\phi(\mathbf{r}, t)$ is a phase variation of the vector that depends on the space and the time.

The detected signal is a voltage induced on a coil due to the variations of the magnetic flux because of the precession of the magnetization of the inspected object. This voltage can be expressed as

$$E = -\frac{d\Phi}{dt} \quad (1.36)$$

where Φ is the flux in the coil. Commonly, the same coil is used in transmission and in detection; let us assume that for a given configuration of a coil and a current I_1 , the generated field is \mathbf{B}_1 . For the reciprocity principle, as explained in [70] the sensitivity of the coil can be defined as $\mathbf{C}_1 = \frac{\mathbf{B}_1}{I_1}$. The increment of the voltage due to the magnetization of an element $d\mathbf{r}$ is equal to:

$$dE = -\left[\mathbf{C}_1(\mathbf{r}) \cdot \frac{\partial}{\partial t}\mathbf{M}(\mathbf{r}, t)\right]d\mathbf{r} \quad (1.37)$$

The received signal is:

$$s_r(t) = E = \int_V dE = -\int_V \left[\mathbf{C}_1(\mathbf{r}) \cdot \frac{\partial}{\partial t}\mathbf{M}(\mathbf{r}, t)\right]d\mathbf{r} \quad (1.38)$$

The variation in time of the gradient ($\frac{\partial}{\partial t}M_z$) is of the order of $\frac{1}{T_1}$ (1 Hz), while $\frac{\partial}{\partial t}M_{xy}$ varies as ω_0 that is on the order 10^8 Hz. This means that the voltage induced by the xy components is about 7 orders of magnitudes higher than the one due to the variations along z . In other words, we can consider only the components xy of the sensitivity and of the magnetization in the expression of the received signal, obtaining:

$$s_r(t) = -\int_V \text{Re}\left[C_{xy}(\mathbf{r})\frac{\partial}{\partial t}M_{xy}(\mathbf{r}, t)\right]d\mathbf{r} \quad (1.39)$$

where $C_{xy} = C_x + iC_y$. The derivative of the magnetization is

$$\begin{aligned}
\frac{\partial}{\partial t} M_{xy}(\mathbf{r}, t) &= \frac{\partial}{\partial t} \left[M_0(\mathbf{r}) e^{-i\omega_0 t} e^{-\frac{t}{T_2(\mathbf{r})}} e^{-i\gamma \int_0^t \Delta B(\mathbf{r}, t') dt'} \right] \\
&= \left(-i\omega_0 - \frac{1}{T_2(\mathbf{r})} - i\gamma \Delta B(\mathbf{r}, t) \right) M_0(\mathbf{r}) e^{-i\omega_0 t} e^{-\frac{t}{T_2(\mathbf{r})}} e^{-i\gamma \int_0^t \Delta B(\mathbf{r}, t') dt'}
\end{aligned} \tag{1.40}$$

Now, considering that $\omega_0 \gg \frac{1}{T_2}$ and $\omega_0 \gg \gamma \Delta B = \gamma \mathbf{G} \cdot \mathbf{r}$ the first term can be approximated with $-i\omega_0$. In addition, we temporarily neglect the decay with T_2 and we assume that the sensitivity of the coil is constant along the whole object ($C = i\omega_0 C_{xy}(\mathbf{r})$) and that M_0 lies in the transverse plane x-y ($M_0(\mathbf{r}) = M(\mathbf{r})e^{-i\phi_0}$), the received signal is:

$$\begin{aligned}
s_r(t) &= C \int_V \text{Re} \left[M(\mathbf{r}) e^{-i\omega_0 t - i\gamma \int_0^t \Delta B(\mathbf{r}, t') dt' - i\phi_0} \right] d\mathbf{r} \\
&= C \int_V M(\mathbf{r}) \cos \left(\omega_0 t + \gamma \int_0^t \Delta B(\mathbf{r}, t') dt' - i\phi_0 \right) d\mathbf{r} \\
&= C \int_V M(\mathbf{r}) \cos(\omega_0 t + \phi(\mathbf{r}, t) + \phi_0) d\mathbf{r}
\end{aligned} \tag{1.41}$$

The received signal is a real value voltage. Let us transform it in a base-band signal through a complex demodulation, that corresponds to:

$$LPF\{s_r(t)e^{-i\omega_0 t}\} = s_1(t) + is_2(t) \tag{1.42}$$

where LPF indicates the operation of low-pass filter, and $s_1(t) = M(\mathbf{r}) \cos(\phi(\mathbf{r}, t) + \phi_0)$ and $s_2(t) = -M(\mathbf{r}) \sin(\phi(\mathbf{r}, t) + \phi_0)$.

$$s(t) = s_1(t) + is_2(t) = M(\mathbf{r}) e^{-i\phi(\mathbf{r}, t) - i\phi_0} = M_0(\mathbf{r}) e^{-i\phi(\mathbf{r}, t)} \tag{1.43}$$

For pass-band signals we can invert the order of the operation of demodulation and integration, obtaining the equation of the MRI signal[29]:

$$s(t) = C \int_V M_0(\mathbf{r}) e^{-i\phi(\mathbf{r}, t)} d\mathbf{r} = C \int_V M_{x'y'}(\mathbf{r}, t) d\mathbf{r} \tag{1.44}$$

Now, the base-band signal $s(t)$ can be represented by the integral of the transverse magnetization in the rotating frame. Let us consider the case of a planar image, in other words let us suppose that $M_{x'y'}(\mathbf{r}, t) = M_{x'y'}(x, y, t)$ the received signal is:

$$s(t) = C \iint M_{x'y'}(x, y, t) dx dy \quad (1.45)$$

Let us consider a magnetic field varying in space and time through the application of the gradients $G_x(t)$ and $G_y(t)$:

$$B(r, t) = B(x, y, t) = B_0 + G_x(t) \cdot x + G_y(t) \cdot y \quad (1.46)$$

The resonance frequency in each point is then:

$$\gamma B(x, y, t) = \gamma(B_0 + G_x(t) \cdot x + G_y(t) \cdot y) \quad (1.47)$$

the spatial variation of the frequency is:

$$\Delta\omega(x, y, t) = \gamma(G_x(t) \cdot x + G_y(t) \cdot y) \quad (1.48)$$

and the phase distribution is given by:

$$\phi(r, t) = \phi(x, y, t) = \int_0^t \gamma(G_x(t) \cdot x + G_y(t) \cdot y) d\tau \quad (1.49)$$

where the time t starts when the magnetization vector lies in the xy plane, or in other words, at the end of the 90 degree pulse. A further simplification is to consider $C = 1$.

$$\begin{aligned} s(t) &= \iint M(x, y) e^{-i\gamma \left(\int_0^t \gamma(G_x(t) \cdot x + G_y(t) \cdot y) d\tau \right)} dx dy \\ &= \iint M(x, y) e^{-i\gamma \left(\int_0^t \gamma(G_x(t) d\tau \cdot x) + \int_0^t \gamma(G_y(t) d\tau \cdot y) \right)} dx dy \end{aligned} \quad (1.50)$$

where we can define the two quantities[84]:

$$\begin{aligned} k_x(t) &= \frac{\gamma}{2\pi} \int_0^t G_x(\tau) d\tau \\ k_y(t) &= \frac{\gamma}{2\pi} \int_0^t G_y(\tau) d\tau \end{aligned} \quad (1.51)$$

and substituting them into (1.52) yields:

$$\begin{aligned}
s(t) &= \iint M(x, y) e^{-i2\pi(xk_x(t) + yk_y(t))} dx dy = F_{2D}\{M(x, y)\}_{u=k_x(t), u=k_y(t)} \\
&= M(k_x(t), k_y(t))
\end{aligned} \tag{1.52}$$

where F_{2D} indicates the 2-D Fourier Transform. This means that the received signal is equal to the Fourier Transform of the magnetization evaluated in points defined by k_x and k_y : that should not be too surprising because the Fourier Transform in each point is the integral of the object, modified by a varying spatially rotation in the complex plane. In MRI, integration is done through the integration of the voltages of the RF coils, while the variation of phase is done by the gradient coils: in fact, shifting the field and the frequency linearly in a time interval, the magnetization rotates toward the new orientation in the complex plane. In this way the MRI has the same effect of the Fourier Transform.

Starting from the relation of the received signal, the object $M(x, y)$ can be simply reconstructed applying the inverse 2-D Fourier Transform to the received signal:

$$M(x, y) = F_{2D}^{-1}\{M(k_x(t), k_y(t))\} \tag{1.53}$$

Now, applying to the object a constant gradient, we have a so called frequency coding, because each spatial position is coded with a specific frequency.

The negative part of the gradient allows us to acquire even negative spatial frequencies.

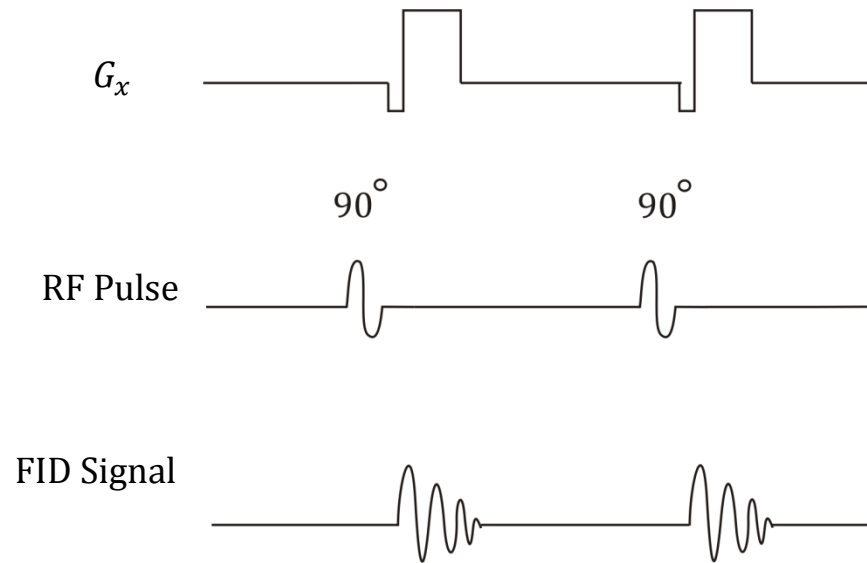


Figure 1.10: Sequence of signals for 1-D imaging

The first 2-D imaging technique used in MRI was based on a sequence of 1-D acquisitions with several gradients in different directions and it is called back-projection. We can see that, applying simultaneously 1-D gradients along x and y , and changing the values at each repetition, we have a 1-D gradient at an angle $\theta = \tan^{-1}\left(\frac{G_x}{G_y}\right)$. In this way, we have several projections of the object from different angles. The projection of the object along one angle θ is called the Radon Transform.

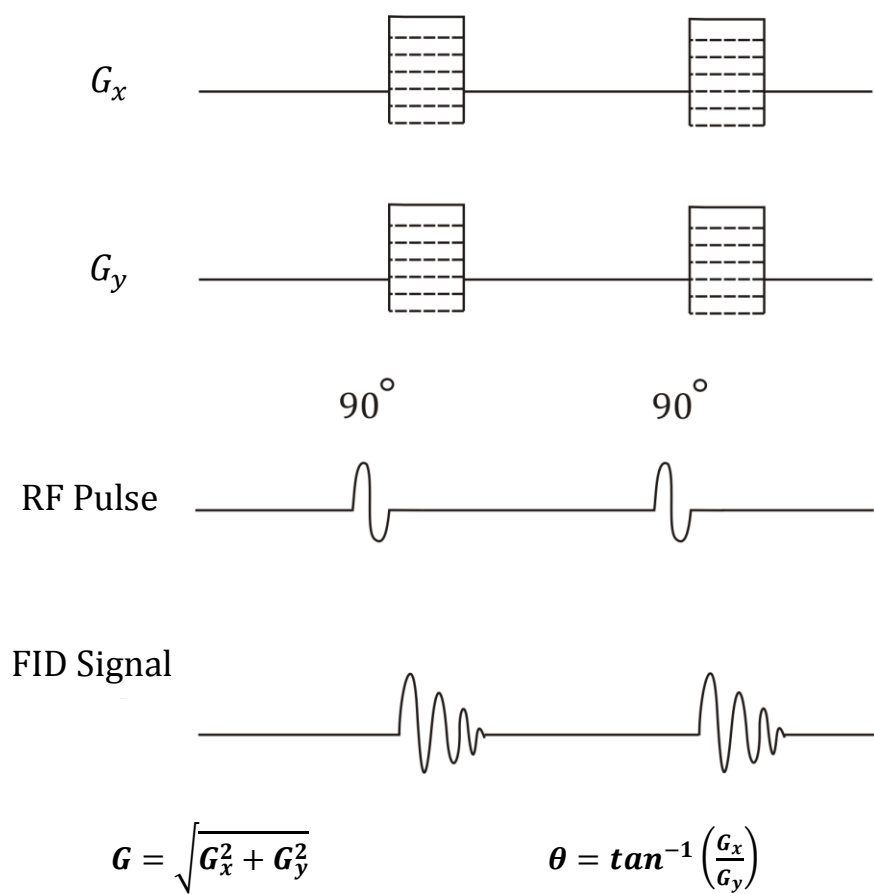


Figure 1.11: Sequence of pulses for back-projection imaging

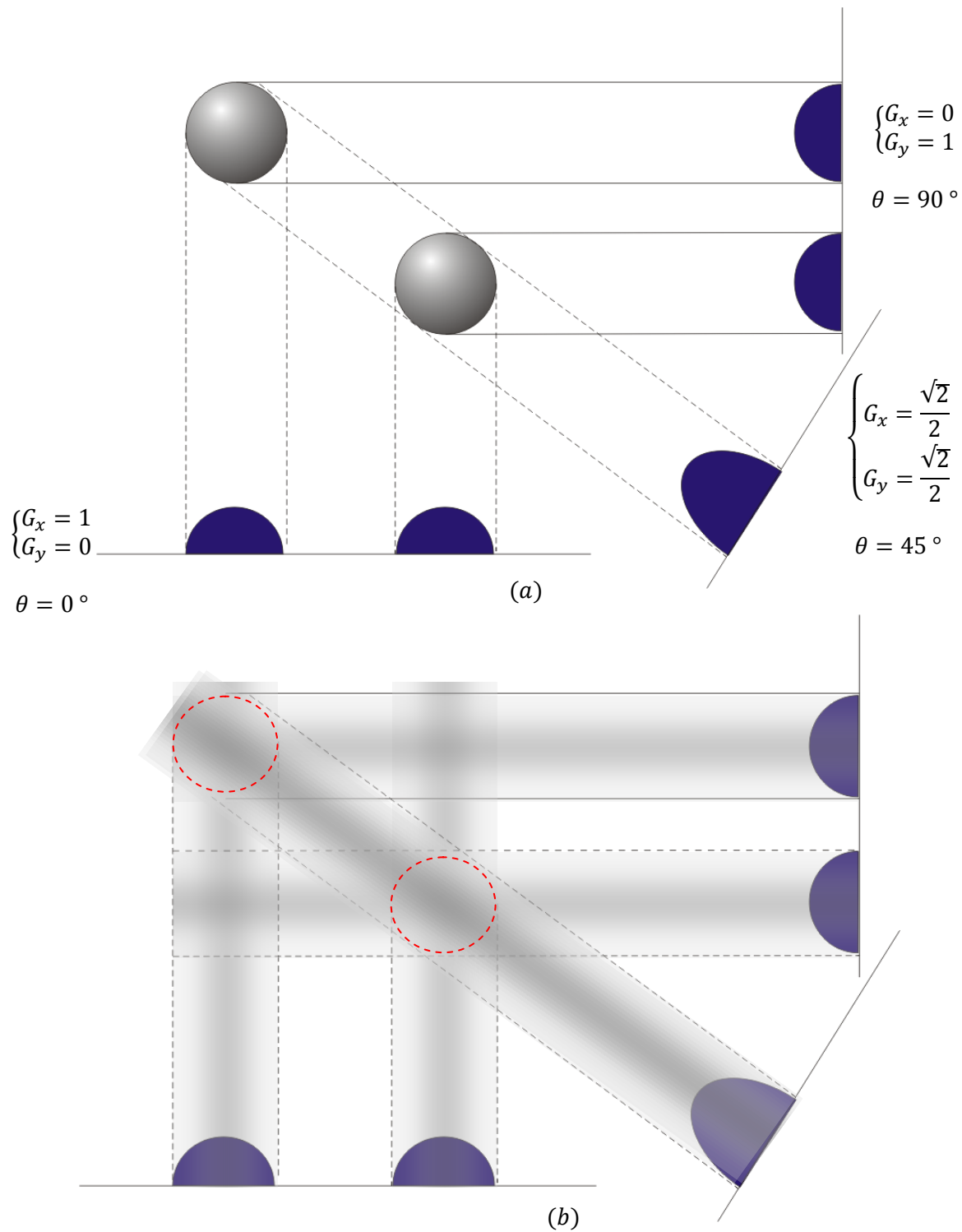


Figure 1.12: (a) Acquisition of the projected signal along three different gradients. (b) Reconstruction of the object starting from the projection. Increasing the number of angles of projection, the image becomes more and more similar to the original.

Now, let us consider a common imaging method used in MRI, the so called spin-warp imaging [107]: this is done with a series of repeated pulses with different values of the gradient field along \hat{y} per each RF pulse (after T_R long time intervals). The gradient on the \hat{x} direction does the frequency coding and \hat{x} is called “frequency direction”. The \hat{y} gradient is on before the acquisition of the data, and it forces a spatial distribution of the phases. Since the G_y is off during the data acquisition, the phase is constant during that time: \hat{y} is called “phase direction”.

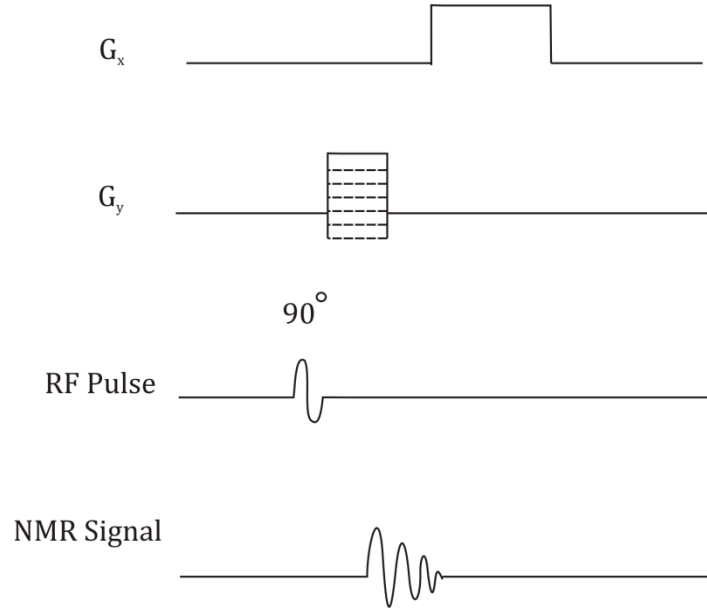


Figure 1.13: Sequence of pulses for spin-warp imaging

1.7 Some useful parameters

Moreover, let us define some parameters that are commonly used in MRI and that describe the spatial resolution of the acquired image, as shown in Fig. 1.14.

$$\Delta k_x = \frac{\gamma}{2\pi} G_x \Delta t \quad (1.54)$$

$$\Delta k_y = \frac{\gamma}{2\pi} G_y \Delta t \quad (1.55)$$

$$W_{k_x} = N_x \Delta k_x = \gamma / 2\pi G_x T_{read} \quad (1.56)$$

$$W_{k_y} = N_y \Delta k_y = \frac{\gamma}{2\pi} 2G_{y,max} T_y \quad (1.57)$$

The sampling in the Fourier domain leads to have a series of images separated in frequency by $(\frac{1}{\Delta k_x}, \frac{1}{\Delta k_y})$. The Field of View (FOV) is defined commonly as:

$$FOV_x = \frac{1}{\Delta k_x} \quad (1.58)$$

$$FOV_y = \frac{1}{\Delta k_y} \quad (1.59)$$

and according to the Shannon's Theorem [104] we don't have aliasing if:

$$x_{\max} \leq \frac{1}{2} FOV_x \quad (1.60)$$

$$y_{\max} \leq \frac{1}{2} FOV_y \quad (1.61)$$

where x_{\max} is the highest spatial position in the x direction and y_{\max} the highest in the y . Commonly, to reconstruct the object a 2-D-FFT is done on a grid of $N \times N$ voxels in the k -space. We can relate the spatial resolution and FOV through:

$$\Delta x = \frac{1}{\Delta W_{k_x}} \quad (1.62)$$

$$\Delta y = \frac{1}{\Delta W_{k_y}} \quad (1.63)$$

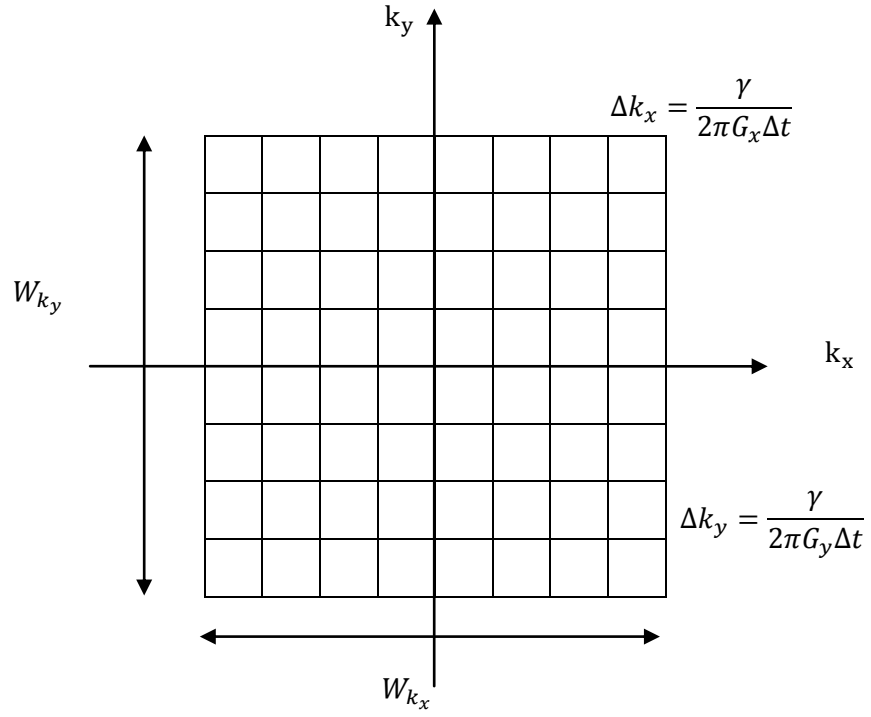


Figure 1.14: Description of the k-space and its resolution

Besides, the total time T necessary to the acquisition of the data for a single image is given by:

$$\Delta y = \frac{1}{\Delta W_{k_y}} \quad (1.63)$$

$$T = T_R N n_{acq}$$

where

- T_R = time of a single sequence
- N = number of points to sample on a coding axis
- n_{acq} = number of acquisitions of the signal repeated to reduce the measure error.

1.8 Sequences of RF pulses

With different RF pulses it is possible to measure the values of T_1 , T_2 , and to obtain MRI images.

A commonly used sequence is the so called inversion recovery, and it is mainly used to measure the value of T_1 and the concentration of the materials. First a 180 degree pulse is applied to direct the magnetization vector towards the z direction so that it does not allow any acquisition of the FID, since there is no signal in the transverse plane. Then, the M vector moves toward the original position along the longitudinal direction, and after the time T_I the intensity of the M vector is:

$$M_z(t) = M_0 \left(1 - 2e^{-\left(\frac{T_I}{T_1}\right)} \right) \quad (1.64)$$

Now we apply a 90 degree pulse to bring the vector $M_z(t)$ in the transverse plane to measure it. When we have a delay of $T_I = \ln 2 T_1$ we have no signal because $M_z(\ln 2 T_1) = 0$ and that means it is a method to have an estimate of the relaxation time T_1 .

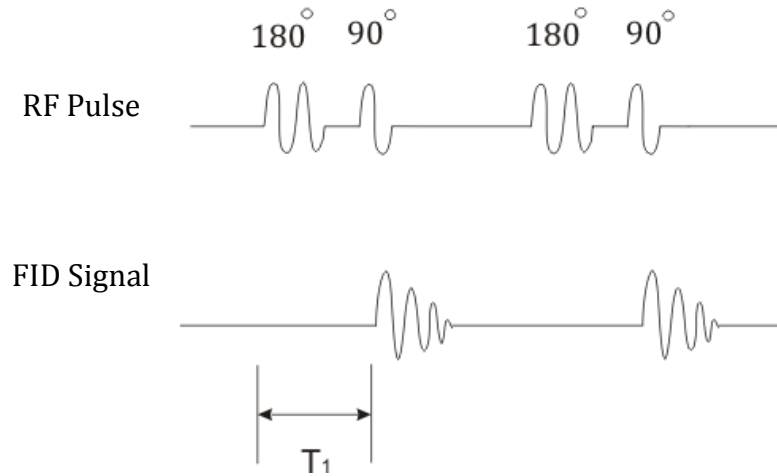


Figure 1.15: RF sequence for inversion recovery

A method to measure the relaxation time T_2 is the so called spin echo sequence[52]. A 90 degrees pulse is first applied, then a delay $\frac{T_E}{2}$, a 180 degrees pulse, and another delay $\frac{T_E}{2}$. To understand better this sequence, let us suppose we apply the 90 degree pulse along the x' axis (x axis in the rotating frame), and consequently the magnetization vector lies on the y' axis. Now, the nuclei that are under the influence of stronger fields will rotate at higher speed, leading to a rotation according the Larmor frequency, slower nuclei will rotate in opposite direction (Fig. 1.17). Since the coherence is broken the FID will tend to 0. However, if we apply a 180 degree pulse (always along the x' axis) every single magnetic moment will be rotated by 180 degrees inverting the situation and leading to recreate the coherence. Since there is the relaxation of the spins, the amplitude of the maximum signal (when the coherence is forced again) will not be the same but it will decay according to the relation

$$FID = M_0 e^{-\frac{T_E}{T_2}} . \quad (1.65)$$

With several measures with different delays T_E it is possible to estimate the value of T_2 .

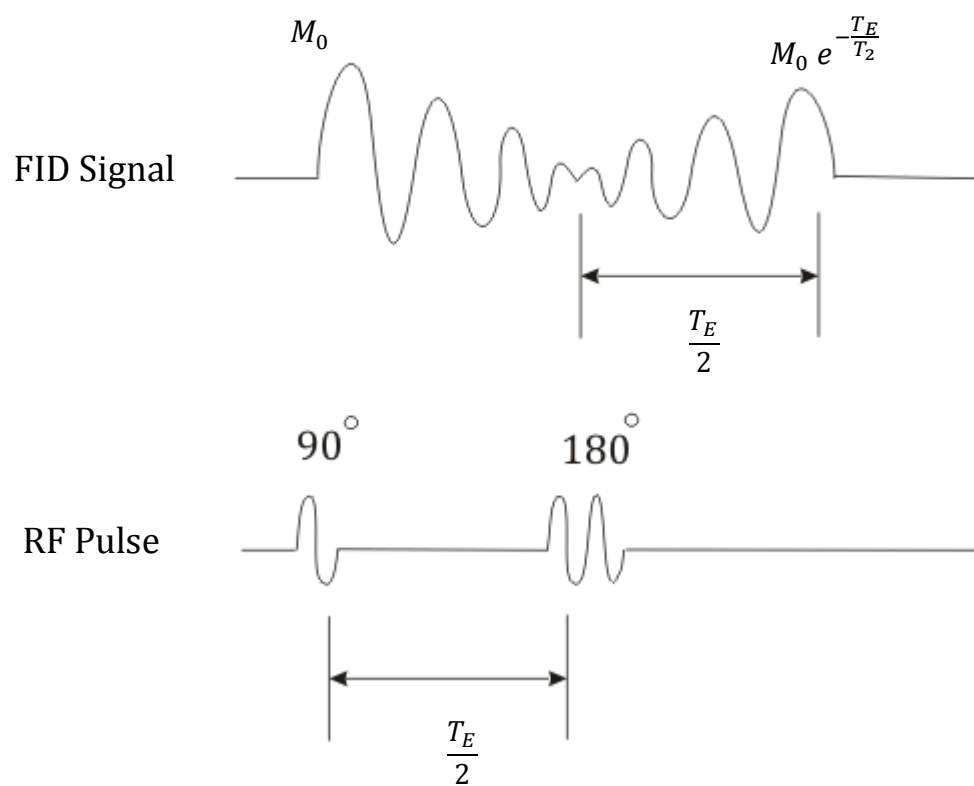


Figure 1.16: RF sequence for spin-echo recovery

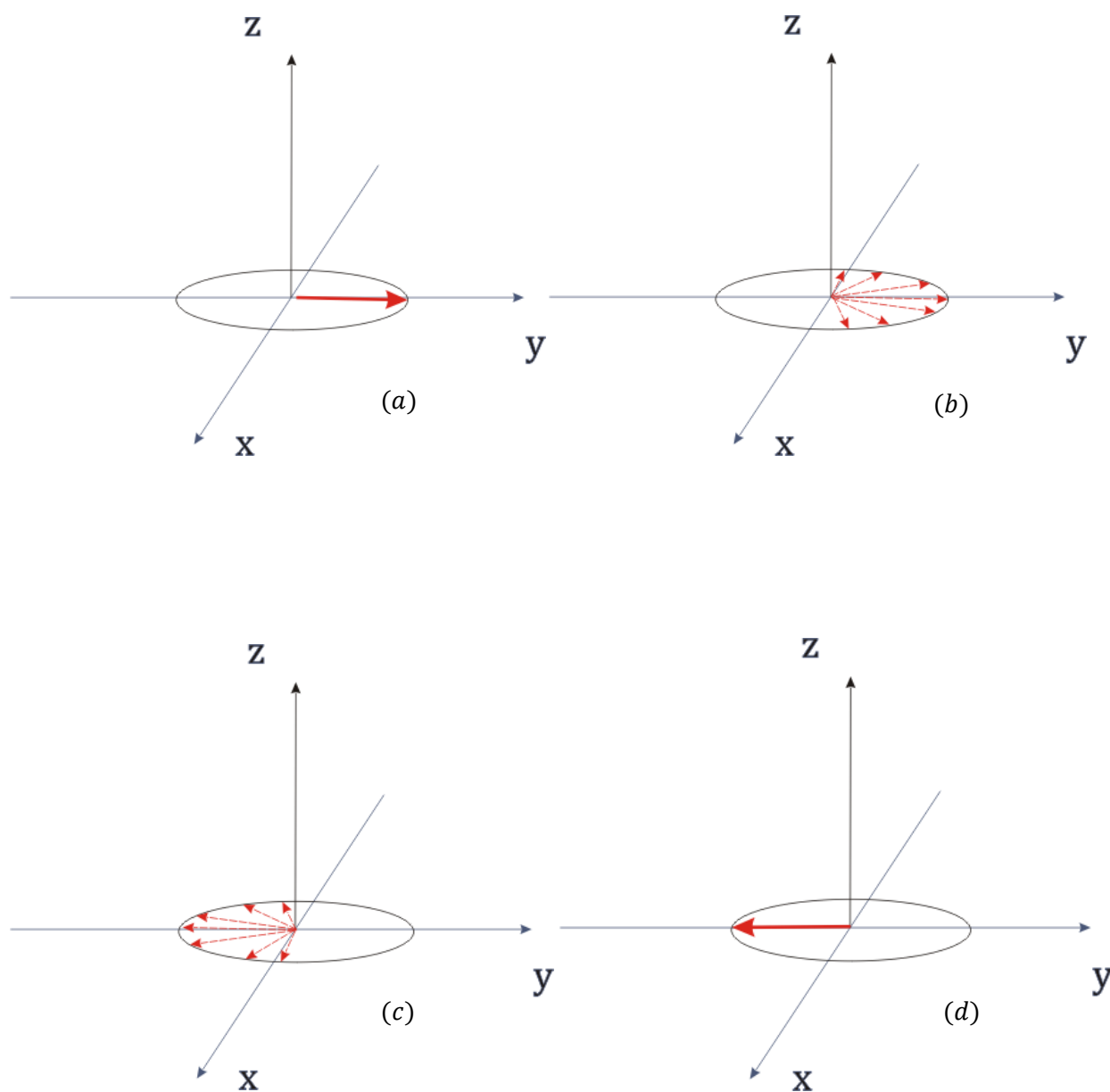


Figure 1.17: Temporal analysis of the magnetic moments in: (a) Application of the 90 degree pulse; (b) Rotation of the moments due the molecular interactions; (c) Application of the 180 degree pulse; (d) Rotation of the moments that return in phase.

With a special RF sequence, it is possible to measure the flip angle in each location of the patient. From the flip angle it is easy to have information about the RF transmitted field distribution, very useful in the design and optimization of the transmitting antennas as we will see in the next chapters. Different solutions have been presented to map the B_1 field [60, 67, 120], and they are mainly based on the differences between the images obtained with two specific excitations. For example, if two images are acquired with two different flip angles α_1 and $\alpha_2 = 2\alpha_1$, the value of α_1 can be calculated with simple trigonometric operations voxel by voxel of the two images.

Also temperature increase can be measured with an MRI experiment: the sequence is based on the temperature dependence of the gyromagnetic ratio γ [46, 38, 115]. This dependence affects the phase of the acquired images, and the method to measure the temperature increase simply consists to acquire an initial image and another image of the same sample after a specific heating time. The difference in phase between the two images is voxel by voxel proportional to the temperature increase in the sample. The method works well especially in presence of high temperature changes, because the relative change in γ is very small (it is about of only $10^{-8} \gamma$ per $^\circ\text{C}$), and so the measurement is highly affected by a strong noise background. Use of temperature measurement is very relevant in MRI systems, because it allows to design MRI sequences and to monitor the safety of the patient affected by RF power absorption during MRI acquisition. This method has also been widely used in monitoring temperature during surgical removal of tumors [49, 73], where the difference in temperature increase is significant.

CHAPTER 2

RF COILS IN MRI

2.1 Introduction

In Chapter 1 the B_1 field for an MRI system has been introduced to rotate the magnetization vector M toward the transverse plane. After a short introduction of the main features of the resonant circuits, some of the most common hardware solutions responsible to generate the B_1 field and to detect the signal are presented in this Chapter, from the simplest surface coils to the more advanced antenna design involving transmit array, very useful in high-field MRI systems where the higher Larmor frequency causes a non-uniform distribution of the field B_1 .

2.2 The RF coils

The RF coils are one basic component of the MRI system, because they generate and receive back the RF signal that excites the spins and causes the rotation of the net magnetization vector. The RF coils can be divided in three subgroups:

- 1) Transmit-only coils;
- 2) Receive-only coils;
- 3) Transmit/Receive coils.

Obviously with transmitting coils we mean the coils that excite the spins, and with receiving coils the ones that detect the signal of the spins. As explained in Chapter 1, the operating frequency of the coils used in an MRI system to generate the RF field B_1 is the Larmor precession frequency of the nucleus of interest, that is set by the value of the applied continuous magnetic field B_0 . A good transmitting coil should guarantee at the Larmor frequency a desired magnetic field distribution in

the volume of interest (most of the times the goal will be to reach a homogeneous field in the region of interest), while a good receiving coil should guarantee a high SNR and be able to receive with the same intensity the signal coming from each point of the volume of interest. If a coil is used both in transmission and reception it has to be able to provide a homogeneous magnetic field and a significantly high SNR : nowadays, several coils are used both for transmission and reception.

There are different types of RF coils used in MRI, but they can be divided in two main groups: volume and surface coils. The volume coils are able to produce a homogeneous B_1 field over a large volume in the coil, and often they are used both in transmission and in reception. The surface coils are much smaller than the volume coils and they are good as receiving coils for their small size, because they pick up noise just from close regions guaranteeing high SNR; however, since they can provide poor homogeneous magnetic fields they are not usually used as transmitting coils [70].

2.3 **The resonant circuits**

Coils are operated as resonant circuits; accordingly we briefly recall a few concepts about resonant circuits. In order to provide maximum efficiency in transmitting and receiving a signal at a specific frequency, we should use a coil having very low electrical impedance at the signal frequency, in our case the Larmor frequency. A simple resonating circuit can be modeled with a voltage generator V , a resistance R , a capacitor C and an inductor L operating at a frequency ω as in Figure (2.1).

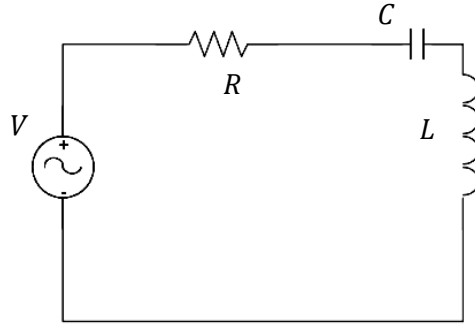


Figure 2.1: Schematic of a resonant circuit

According to the Kirkhoff's laws we can write the current in this circuit in the phasor domain as:

$$V = RI + i\omega LI - \frac{i}{\omega C} I \quad (2.1)$$

If we derive the absolute value of the current from the (2.1) we have:

$$I = \frac{V}{\sqrt{\left(R^2 + \left(\frac{1}{\omega C} - \omega L\right)^2\right)}} \quad (2.2)$$

For which it is easy to see that the current is maximum when

$$\omega = \omega_r = \frac{1}{\sqrt{LC}} \quad (2.3)$$

Since the magnetic field is proportional to the current, resonant circuits are used to provide strong magnetic fields with a relatively small voltage source. The strength of the current is limited by the series resistance that is present in every electric circuit, and its influence on the behavior of the resonant circuit is measured with the so called quality factor:

$$Q = 2\pi \frac{\text{max energy stored}}{\text{energy dissipated per cycle}} = \frac{\omega_r}{\Delta\omega} \quad (2.4)$$

where $\Delta\omega$ is the bandwidth of the circuit. For a circuit a higher quality factor corresponds to higher efficiency in transmitting the field.

2.4 The surface coil

A very simple resonating circuit is given by a metallic loop with a capacitor. Referring to the schematic of the resonant circuit shown in Fig. 2.2, the inductor is given by the loop itself, and the capacitor is tuned to match the inductor at the frequency of interest according to eq. (2.3), and the resistance is given by the finite conductivity of the metal of the coil and the impedance from radiation and energy absorbed by near objects. An additional capacitor is added in series to match the resonating circuit to the power source, guaranteeing maximum transmission of the power to the circuit. The magnetic field B_1 generated by a surface coil is oriented along the direction perpendicular to the plane of the loop, and it decays rapidly far from the coil. For this reason, the surface coil is widely used to excite locally the samples in case the region of interest is external, or as a receiving coil. In fact, due to its high sensitivity near the surface of the coil and its weak sensitivity elsewhere, it receives a clear near field signal and it picks low noise in other regions of not interest: commonly, this corresponds to have high SNR in the region of interest, which is a relevant feature of a receiving coil.

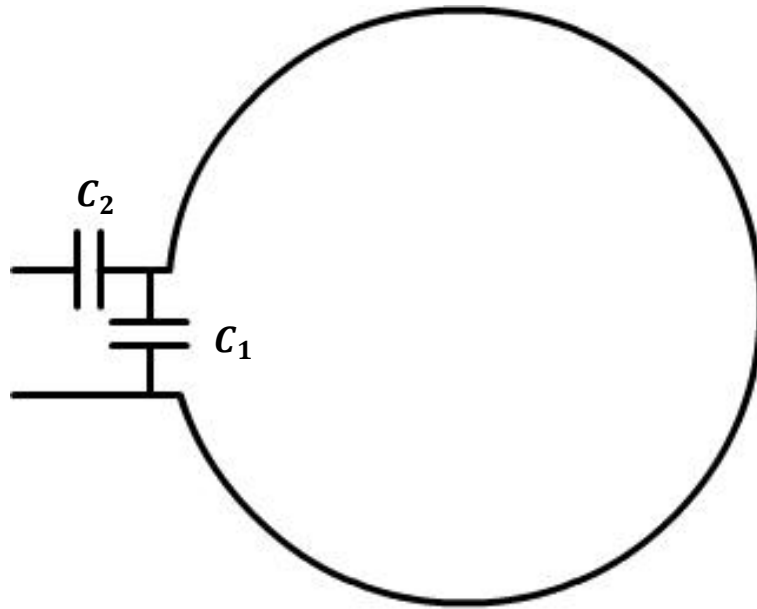


Figure 2.2: Schematic of a surface coil circuit

2.5 **The saddle coil**

Two rectangular loops may be positioned around two opposite sides of a cylinder (as shown in Fig. 2.3), making a volume coil called saddle coil. As a volume coil, it can provide good homogeneity of the field in the sample, and it can be shown that the maximum field homogeneity in the whole sample can be obtained when the azimuthal angle between the legs of the same loop is 120° [72]. The current in the adjacent stripes of opposite loops has to flow in the same direction, and the matching capacitors are placed equivalently to what shown for the single surface coil.

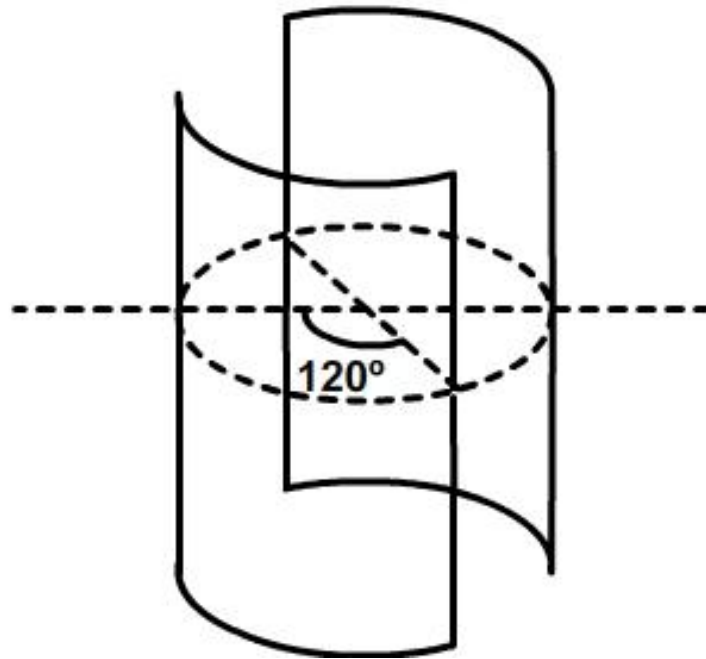


Figure 2.3 Schematic of a saddle circuit

2.6 The birdcage coil

Another very common volume coils, especially for brain applications, is the so called birdcage coil[55]. The birdcage coil is a resonant circuit composed of N thin parallel conductor strips that are positioned along a cylindrical surface and parallel to its axis. If the ends of the strips are short circuited and on the strips are positioned N capacitors we have a lowpass birdcage coil, otherwise if the ends are connected by N capacitors we have a highpass birdcage coil (Fig. 2.4). In literature the conducting strips are called “legs” and the connecting end loops “end-rings”.

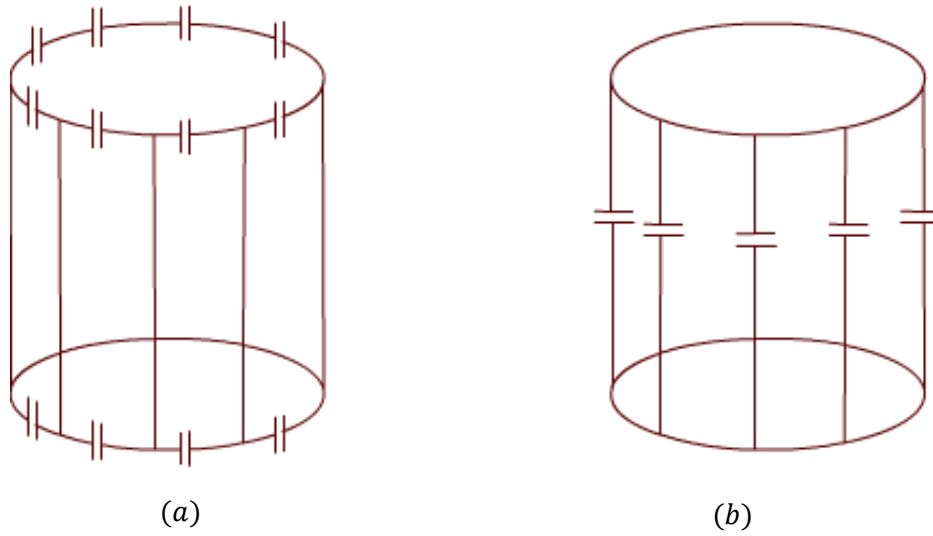


Figure 2.4: (a) Highpass Birdcage coil. (b) Lowpass Birdcage coil.

It is possible to tune the coil to make it work at the desired frequency by varying the values of the capacitors, the length and the width of the legs (that correspond to inductances). In addition, several techniques are used to reduce the impedance (and so increasing the quality factor) of the coil: capacitors in parallel, shorter length of the legs, larger width of the legs, etc.

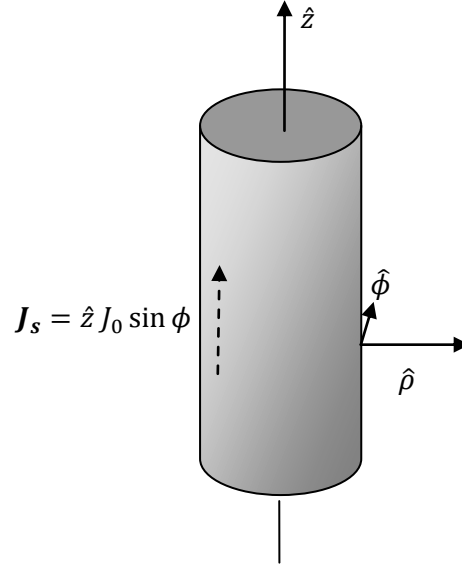


Figure 2.5: Metallic cylinder with current $J_s = J_0 \sin \phi$.

The birdcage coil is a resonant circuit, and its "mode 1" emulates the behavior of a conducting cylinder of infinite length carrying a longitudinal current having an angular distribution given by

$$J_s = \hat{z} J_0 \sin \phi \quad (2.5)$$

At low frequency fields, in a source free region, we can write the Maxwell's equations as

$$\nabla \cdot \mathbf{B} = 0 \quad (2.6)$$

$$\nabla \times \mathbf{B} = 0 \quad (2.7)$$

Because of (2.7), it is possible to introduce a scalar potential defined as

$$\mathbf{B} = -\nabla \psi \quad (2.8)$$

as explained in [70]. Then, substituting Eq. (2.8) in Eq. (2.6) yields

$$\nabla \cdot (-\nabla \psi) = 0 \quad (2.9)$$

or equivalently:

$$\nabla^2 \psi = 0 \quad (2.10)$$

that is the Laplace equation and it can be solved with the method of separation of variables. Assuming there is no variation in the \hat{z} direction, the general solution in cylindrical coordinates is given by

$$\psi(\rho, \phi) = \sum_{m=-\infty}^{+\infty} \rho^m (A_m \cos m\phi + B_m \sin m\phi) \quad (2.11)$$

where A_m and B_m are constants to be determined basing on the boundary conditions. From the given definition of the potential, we obtain

$$\begin{aligned} \mathbf{B}(\rho, \phi) = & -\hat{\rho} \sum_{m=-\infty}^{+\infty} m\rho^{m-1} (A_m \cos m\phi + B_m \sin m\phi) \\ & + \hat{\phi} \sum_{m=-\infty}^{+\infty} m\rho^{m-1} (A_m \sin m\phi - B_m \cos m\phi) \end{aligned} \quad (2.12)$$

If we consider now the presence of the conducting cylinder, supposing its radius is a , we can compute the value of the coefficients analyzing the field outside and inside the cylinder, and imposing the boundary conditions at the interface of the cylinder.

Since the field has to decay as ρ increases, we have to neglect all the terms with $m \geq 1$ imposing $A_m = 0$ and $B_m = 0$ for $m \geq -1$ ($m = 0$ does not give any contribute). Indicating with \mathbf{B}_{out} the \mathbf{B} field outside the cylinder,

$$\begin{aligned} \mathbf{B}_{out}(\rho, \phi) = & -\hat{\rho} \sum_{m=-\infty}^{-1} m\rho^{m-1} (A_m \cos m\phi + B_m \sin m\phi) \\ & + \hat{\phi} \sum_{m=-\infty}^{-1} m\rho^{m-1} (A_m \sin m\phi - B_m \cos m\phi) \end{aligned} \quad (2.13)$$

Inside the cylinder, the field has to be finite for $\rho = 0$, and this can be achieved by imposing $A_m = 0$ and $B_m = 0$ for $m \leq 1$. Calling \mathbf{B}_{in} the \mathbf{B} field inside the cylinder

$$\begin{aligned}
\mathbf{B}_{in}(\rho, \phi) = & -\hat{\rho} \sum_{m=1}^{+\infty} m \rho^{m-1} (A_m \cos m\phi + B_m \sin m\phi) \\
& + \hat{\phi} \sum_{m=1}^{+\infty} m \rho^{m-1} (A_m \sin m\phi - B_m \cos m\phi)
\end{aligned} \tag{2.14}$$

Now we need to impose the boundary conditions

$$\begin{cases} (\mathbf{B}_{out} - \mathbf{B}_{in}) \cdot \hat{n} = 0 \\ \hat{n} \times (\mathbf{B}_{out} - \mathbf{B}_{in}) = \mu_0 J_0 \sin \phi \hat{z} \end{cases} \tag{2.15}$$

that correspond to

$$\begin{cases} \sum_{m=-\infty}^{-1} m a^{m-1} (A_m \cos m\phi + B_m \sin m\phi) = \sum_{m=1}^{+\infty} m a^{m-1} (A_m \cos m\phi + B_m \sin m\phi) \\ \frac{1}{a^2} \sum_{m=-\infty}^{-1} m a^{m-1} (A_m \sin m\phi - B_m \cos m\phi) - \sum_{m=1}^{+\infty} m a^{m-1} (A_m \sin m\phi - B_m \cos m\phi) = \mu_0 J_0 \sin \phi \end{cases} \tag{2.16}$$

The only nonzero terms are A_{-1} and A_1 and are

$$\begin{cases} -\frac{A_{-1}}{a^2} = A_1 \\ \frac{A_{-1}}{a^2} - A_1 = \mu_0 J_0 \end{cases} \tag{2.17}$$

$$\begin{aligned}
A_{-1} &= \mu_0 \frac{J_0 a^2}{2} \\
A_1 &= -\mu_0 \frac{J_0}{2}
\end{aligned} \tag{2.18}$$

The field inside the cylinder is given by:

$$\mathbf{B}_{in}(\rho, \phi) = \hat{\rho} \mu_0 \frac{J_0}{2} \cos \phi - \hat{\phi} \mu_0 \frac{J_0}{2} \sin \phi = \hat{x} \mu_0 \frac{J_0}{2} \tag{2.19}$$

and this shows that with the current distribution (2.5) of the cylinder (that is the same current distribution of the first resonant mode of the birdcage coil) it is possible to obtain inside the volume of the cylinder a homogeneous linear magnetic field.

It is important to have a homogeneous B_1 field inside the inspected volume because, according to Eq. (1.26), the flip angle depends on the value of the transmitted B_1 field, in as to guarantee the same transmitted field. However, in the rotating frame we considered an incident circularly polarized transmitted field, but the homogeneous field that the birdcage coil (and the metallic cylinder) can guarantee is linearly polarized: how does it agree with the type of polarization we have in the rotating frame?

A linearly polarized field is equivalent to the sum of two circularly polarized fields: for example, if the transmitted field is $\mathbf{B}_1 = B_1 \cos \omega t \hat{x}$, it can be decomposed as

$$\mathbf{B}_1 = \frac{B_1}{2} [\cos \omega t \hat{x} + \sin \omega t \hat{y}] + \frac{B_1}{2} [\cos \omega t \hat{x} - \sin \omega t \hat{y}] \quad (2.33)$$

Of these two components, only the one that rotates in the direction of the magnetization is in resonance with the magnetization vector, while the other is just dissipated power: this means that providing a circularly polarized field it is obtained an increase in the SNR of a factor $\sqrt{2}$, or in other words generating a circularly polarized wave the same result is achieved using half of the power.

Equivalently, the signal emitted by the nuclei is circularly polarized, which means that the SNR is optimized if the received signal is in quadrature, allowing an increase of the SNR of a factor $\sqrt{2}$. The relation between the efficiency of linearly and circularly polarized fields has been deeply explored in [50].

With a birdcage coil, a circularly polarized in transmission and an optimum detection is obtained using two channels with a 90 degree phase shift between them.

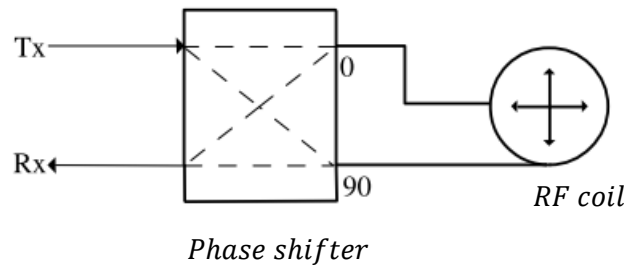


Figure 2.6: Transmission and reception in a quadrature system.

Looking at the classical birdcage coil we can see that it is a structure similar to a phased array, but with some constraints about the difference of phase and amplitude between each element.

2.7 The transmit array

A phased array is a group of antennas that are controlled such that it is possible to produce a specific radiation pattern, forcing constructive interference in some locations and destructive in others, without increasing significantly the size of the antenna. Commonly, all the elements of the array are identical (but driven in a different way), but it is not necessary. Phased arrays are used in a variety of fields: from broadcast radio stations (to provide the best signal in a specific town and a weak signal elsewhere) to naval usage (recognition and tracking of aircrafts and missiles), from weather research to optics, etc.

One very common phased array is the one composed by N parallel wires: controlling the currents in terms of amplitude and phase of each wire, it is possible to produce the desired radiation pattern.

This is the reason why a classical birdcage coil can be seen as a phased array, where the legs are the elements of the arrays (N parallel wires), and with their specific current scheme they are able to provide a homogeneous magnetic field inside the volume as the desired radiation pattern.

However, the relation between the currents of a classical birdcage coil was found in the 70's and was very practical because it makes possible to work having just one power supply (or 2 in case of quadrature excitation). In 40 years, there has been a significant increase in the strength of the continuous magnetic field B_0 with a corresponding increase of the excitation frequency and decrease of the wavelength: when the operating wavelength of a circuit becomes comparable with the size of the inspected object, the distribution of the magnetic field may be different. For example, using a classical birdcage coil to excite a cylinder having a radius of 8 cm with an operating frequency of 64 MHz (corresponding to a magnetic field B_0 1.5 T) the resulting magnetic field distribution inside the cylinder is homogeneous (Figure 2.7 (a)), while exciting in the same way at 400 MHz (corresponding to a magnetic field B_0 of 9.4 T) the distribution depicted Figure (2.7(b)) is obtained. Hence, increasing the frequency, new ways to excite the patient need to be explored, in order to provide a field as homogeneous as the one at lower frequencies. The field not homogeneous may affect the quality of the images, because all the atoms are not excited in the same way: this corresponds to a inhomogeneous spatial distribution of the magnetization vector, leading to areas where the transverse component of the magnetization vector is stronger and areas where it is weaker. Where the signal is weak the SNR is lower, with a consequent lower resolution, and when the interference is highly destructive there are even areas of no signal, where no information on the inspected object is achievable, and those areas are seen as dark spots[33].

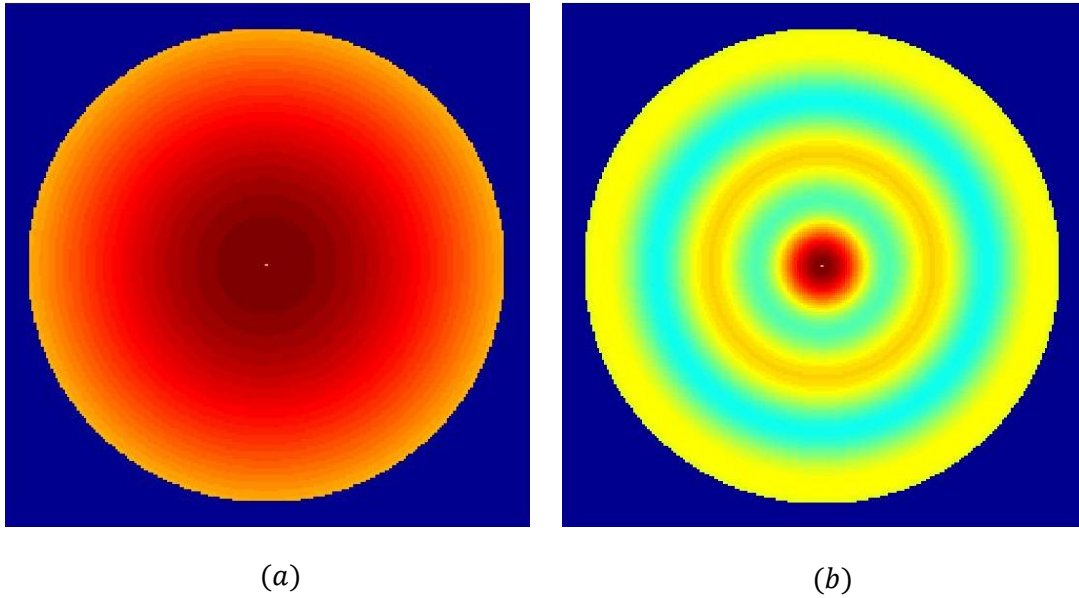


Figure 2.7: Normalized flip angle in the transverse plane with a classic birdcage coil driving at 64 MHz (a), and at 400 Mhz (b)

Even if previous relations are not valid anymore and it is harder to create a homogeneous magnetic field, there are several reasons to increase the value of B_0 , and consequently even the frequency: at higher B_0 fields the net magnetization induced on the inspected object is stronger, and that corresponds to a higher received signal. This leads to have a higher SNR and consequently higher resolution in the images, higher sensitivity to inspect deeply anatomical aspects, and even to open new research fields such as functional MRI with the inspection of the blood oxygenation level-dependent contrast (BOLD) and other brain activities[90, 97]. These new medical research fields require a complete new engineering analysis of the MRI system, from the penetration of the RF fields inside the patient to the different T_2 time, from the design of the B_0 magnet to the design of the coils of the B_1 field. In this research we focused our attention on this last problem. In fact, at higher frequencies we have smaller wavelengths, and at 400 MHz they are comparable with the dimensions of the human body, with the consequent onset of effects like destructive and

constructive interference patterns, making inhomogeneous the magnetic field B_1 in the brain, and yielding bright (hot) and dark (cold) RF spots on the image.

One promising solution to overcome the problem of the homogeneity of the magnetic field is to increase the degrees of freedom in the legs of the birdcage coil. It is called RF shimming and it applies concepts from array antenna theory, suggesting a different improved design for the RF coil, where the coil is designed as a transmit array with its elements separately controlled by different channels. This technique has been presented in [86, 76]. In other words the birdcage coil can be replaced with a phased array where all the magnitudes and phases of the legs have to be optimized. Other methods useful to reduce the field inhomogeneity involve special pulse sequences such as composite pulses [35] and transmit SENSE [77].

CHAPTER 3

2-D ANALYTICAL SOLUTIONS TO SIMPLIFY THE ANALYSIS OF THE B_1 FIELD DISTRIBUTION IN THE HEAD

3.1 Introduction

In Chapter 2 we presented a fairly new concept of a transmit array with the wires aligned and parallel to the z axis, and independently controlled by several channels. In this Chapter we present two 2-D analytical solutions to simplify the analysis of the magnetic field distribution obtained by such a transmit array when loaded with a human head. The main difference between the circular and the elliptic model is the ability of the elliptic model to predict the number and the position of the peaks of magnetic field even if the wires are not aligned along one single axis.

3.2 The circular 2-D model

Our first simplified problem consists of two concentric dielectric circular cylinders, where the inner one represents the brain and the outer the skull. Externally, parallel to the z axis, the axis of symmetry of these cylinders, N conducting wires representing the transmit array are placed around the cylinders, at a distance c from the center of the cylinders, as shown in Fig. 3.1.

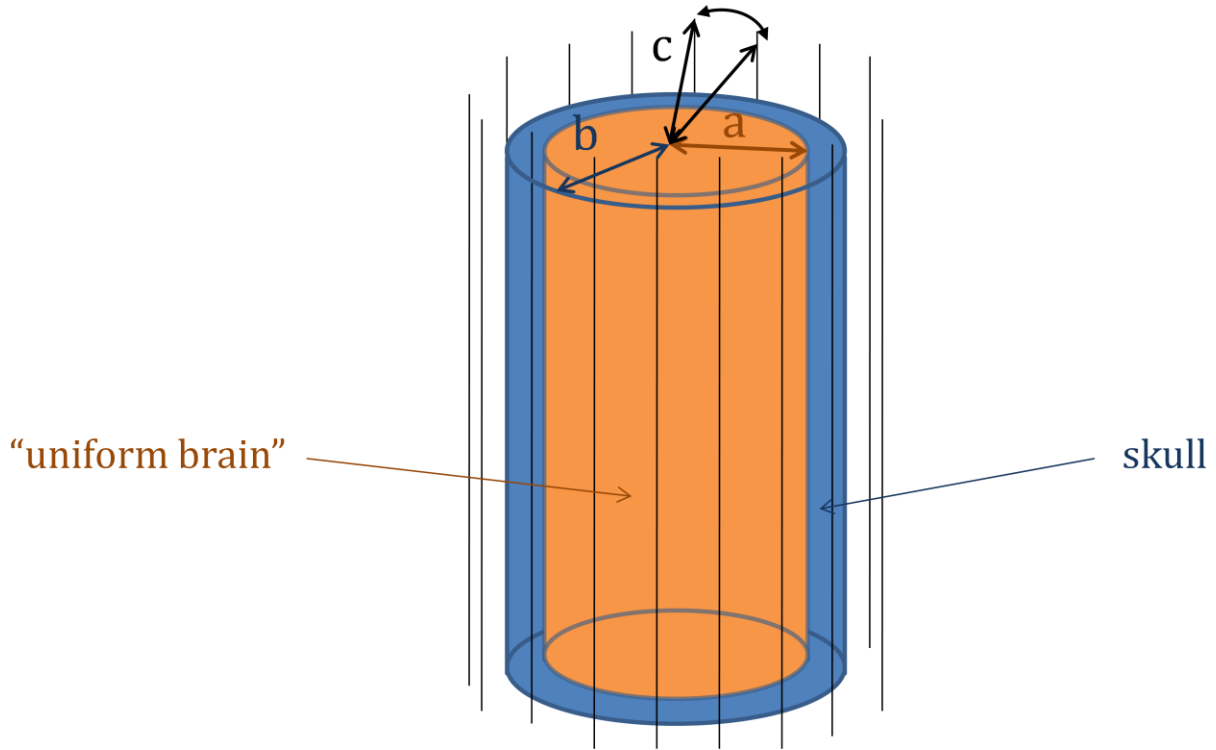


Figure 3.1 Geometric representation of the circular cylindrical model

The conducting wires are parallel to the z -axis, and consequently also the generated electric field is parallel to the z -axis. Given the electrical properties of the material (permittivity ϵ , the conductivity σ and the susceptibility μ) and the frequency ω , the propagation constant k into the material is given by

$$k = j\omega\sqrt{\mu\epsilon} \sqrt{1 - \frac{j\sigma}{\omega\epsilon}} \quad (3.1)$$

Considering the symmetry of our problem, the electric field (E_b) inside the outer dielectric cylinder is given by the superposition of Bessel functions of both the first (J_n) and second kind (Y_n).

$$\begin{aligned}
E_b &= \sum_{n=-\infty}^{+\infty} (b_n J_n(k_b \rho) + c_n Y_n(k_b \rho)) e^{jn\phi} \\
&= \sum_{n=-\infty}^{+\infty} (b_n J_n(k_b \rho) + c_n H_n^{(2)}(k_b \rho)) e^{jn\phi}
\end{aligned} \tag{3.2}$$

where k_b is the propagation constant into the outer cylinder, and b_n and c_n are expansion coefficients to be determined later imposing the boundary conditions at the interfaces.

The two expressions in eq. (3.2), first in terms of superposition of Bessel functions of the second kind and then of Hankel functions ($H_n^{(2)}$), are equivalent because when summed to the Bessel functions of the first kind they span the same functional space: in the rest of the chapter we will only use the Hankel function relation.

Inside the inner dielectric cylinder, the electric field (E_a) is only given by the superposition of Bessel functions of the first kind because the origin of the axis ($\rho = 0$) belongs to the cylinder, and the Hankel functions diverge for $\rho \rightarrow 0^+$. Since we do not have any wave source in the origin of the axes, the electric field has to be finite in that location: hence, the expansion coefficients of the Hankel functions have to be null.

$$E_a = \sum_{n=-\infty}^{+\infty} a_n J_n(k_a \rho) e^{jn\phi} \tag{3.3}$$

where k_a is the propagation constant into the inner cylinder, and a_n are expansion coefficients of the series.

Externally we have the superposition of the Hankel functions representing the incident fields generated by the wires, and the Hankel functions representing the scattered field from the cylinders, because the Hankel functions satisfy the radiation condition at infinite distance from the source.

$$E_c = \sum_{n=-\infty}^{+\infty} d_n H_n^{(2)}(k_0 \rho) e^{jn\phi} - \sum_{i=1}^N \frac{k_0^2 I_i}{4\omega\epsilon_0} H_0^{(2)}(k_0 |\vec{\rho} - \vec{c}|), \tag{3.4}$$

To have a complete description of the electric and magnetic fields we need to find the value of the expansion coefficients a_n , b_n , c_n and d_n .

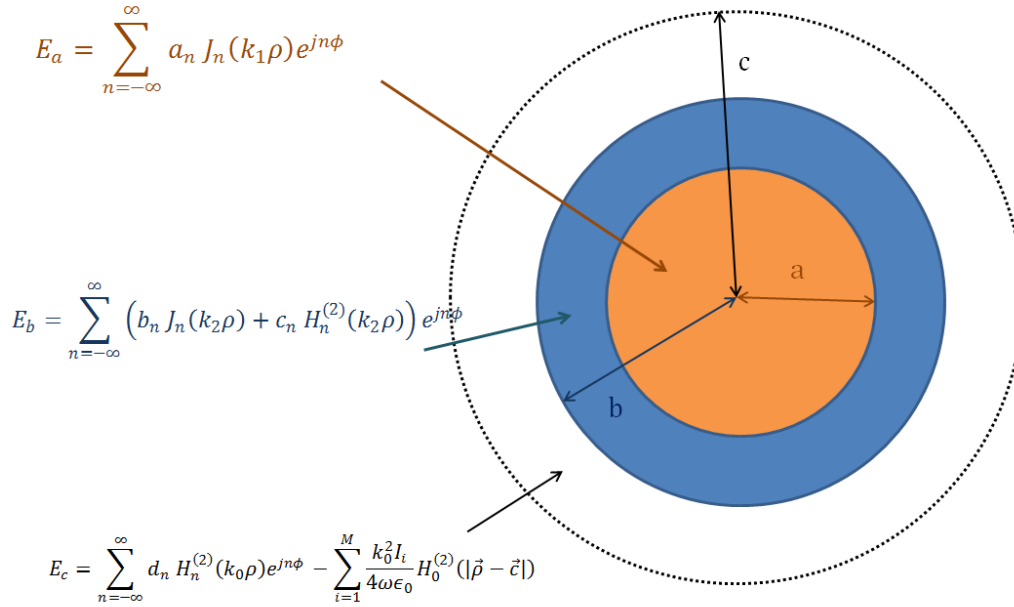


Figure 3.2: Expressions of the total electric field as series of Bessel functions inside the different materials of the circuit model

It is possible to derive the magnetic fields distribution starting from the electric fields, using the Maxwell's equations in cylindrical coordinates. Since the electric field is parallel to the z -axis the magnetic field will be in the xy plane and can be calculated as

$$H_\rho = -\frac{1}{j\omega\mu\rho} \frac{\partial E_z}{\partial \phi}, \quad (3.5)$$

$$H_\phi = \frac{1}{j\omega\mu} \frac{\partial E_z}{\partial \rho}.$$

By imposing the continuity of the tangential components of the electric and magnetic fields across the interfaces of the dielectric cylinders we can find the expansion coefficients solving the system:

$$\begin{bmatrix} J_n(k_a a) & -J_n(k_b a) & -H_n^{(2)}(k_b a) & 0 \\ k_1 J_n'(k_a a) & -k_2 J_n'(k_b a) & -k_2 H_n^{(2)}(k_b a) & 0 \\ 0 & J_n(k_b b) & H_n^{(2)}(k_b b) & -H_n^{(2)}(k_0 b) \\ 0 & k_2 J_n'(k_b b) & k_2 H_n^{(2)'}(k_b b) & -k_0 H_n^{(2)'}(k_0 b) \end{bmatrix} \begin{bmatrix} a_n \\ b_n \\ c_n \\ d_n \end{bmatrix} = \begin{bmatrix} 0 \\ 0 \\ -\frac{k_0^2}{4\omega\epsilon_0} \sum_{i=1}^N I_i J_n(k_0 \rho) H_n^{(2)}(k_0 c) e^{-jn\phi'_i} \\ -\frac{k_0^3}{4\omega\epsilon_0} \sum_{i=1}^N I_i J_n'(k_0 \rho) H_n^{(2)}(k_0 c) e^{-jn\phi'_i} \end{bmatrix} \quad (3.6)$$

where we have used the series expansion of the Hankel functions:

$$H_0^{(2)}(k_0 |\vec{\rho} - \vec{c}|) = \sum_{n=-\infty}^{+\infty} J_n(k_0 \rho) H_n^{(2)}(k_0 c) e^{-jn\phi'_i} \quad (3.7)$$

To check the validity of our model, since we respresented the skull and the brain as two concentric circular cylinders, we compared the magnetic field distribution that we obtain applying the same current schemes to our 2-D model and to a high fidelity model of a brain, in particular the one that is present in the 3-D commercial software xFDTD(Remcom, Inc; State College, PA). Different current schemes are obtained, for example, changing the number and the position of the conducting wires and the difference in phase among them.

The slice of the head that we selected has two axes of symmetry having length of 20 and 16 cm. From the plots in Fig. 3.5 it is possible to see that using a couple of wires that are aligned with one of the axes of symmetry, and setting the diameter of the external cylinder equal to the selected axis of symmetry, it is possible to predict the number and the position of the peaks of intensity of the magnetic field with the 2-D model.

This 2-D circular model fails if the wires are not aligned with only one axis of symmetry, because otherwise it is not possible to select the right value of the diameter of the cylinder.

3.3 **The elliptic 2-D model**

These problems can be overcome using a 2-D elliptic cylindrical model.

Like in the previous model, we have N conducting wires representing the legs of a birdcage coil and 2 concentric cylinders (having elliptic cross-sections) representing the skull and the brain (it is like the geometry represented in Figure 3.2 but with an elliptic base).

To describe the spatial distribution of the fields we used the elliptic coordinate system having two foci located at $(\pm \frac{d}{2}, 0)$ with focal distance d [106]. The relation between the elliptic coordinates (u, v) and the Cartesian coordinates (x, y) is

$$\begin{aligned} x &= \frac{d}{2} \cosh u \cos v, \\ y &= \frac{d}{2} \sinh u \sin v. \end{aligned} \tag{3.8}$$

From this definition, surfaces having $u = \text{constant}$ represent a family of elliptic cylinders having the same foci located at $x = \pm \frac{d}{2}$ on the x axis, while surfaces having $v = \text{constant}$ represent a family of confocal hyperbolic cylinders. The distance between the foci is related to the major (A) and minor (B) axes of the ellipse by

$$d^2 = A^2 - B^2 \tag{3.9}$$

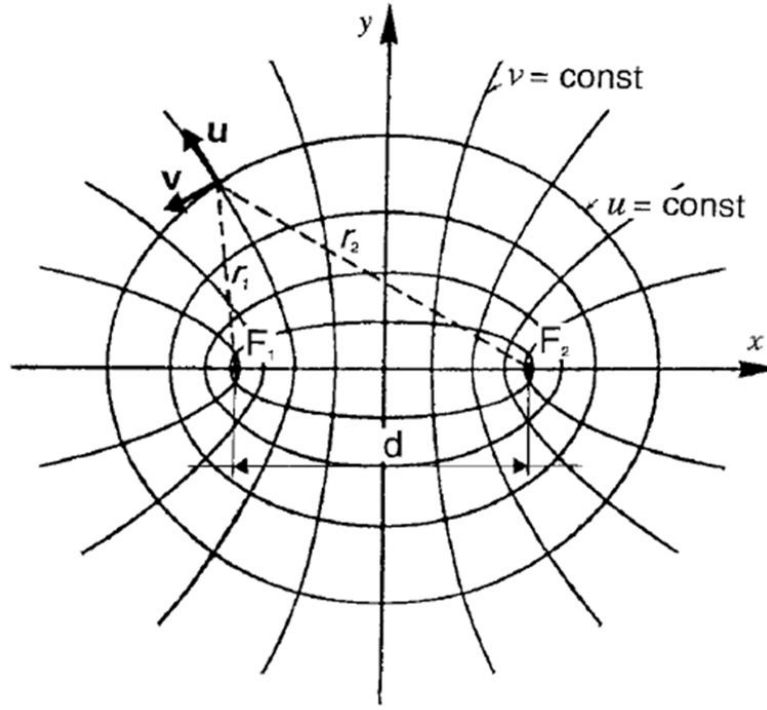


Figure 3.3: Elliptic Cylindrical coordinates

Like the previous model, the electric field is oriented along the z axis, and inside the inner cylinder it is equal to

$$E_a = \sum_{m=0}^{+\infty} \left[a_m Re_m^{(1)}(q_a, u) Se_m(q_a, v) \right] + \sum_{m=1}^{+\infty} \left[b_m Ro_m^{(1)}(q_a, u) So_m(q_a, v) \right] \quad (3.10)$$

while in the outer cylinder it is equal to

$$E_b = \sum_{m=0}^{+\infty} \left[c_m Re_m^{(1)}(q_b, u) Se_m(q_b, v) + d_m Re_m^{(2)}(q_b, u) Se_m(q_b, v) \right] \\ + \sum_{m=1}^{+\infty} \left[e_m Ro_m^{(1)}(q_b, u) So_m(q_b, v) + f_m Ro_m^{(2)}(q_b, u) So_m(q_b, v) \right] \quad (3.11)$$

and externally it is

$$E_c = \sum_{m=0}^{+\infty} \left[g_m Re_m^{(4)}(q_0, u) Se_m(q_0, v) \right] + \sum_{m=1}^{+\infty} \left[h_m Ro_m^{(4)}(q_0, u) So_m(q_0, v) \right] - \sum_{i=1}^N \frac{k_0^2 I_i}{4\omega\epsilon_0} H_0^{(2)}(k_0 |\vec{\rho} - \vec{c}|) \quad (3.12)$$

where $q_i = \frac{(k_i d)^2}{16}$, $Re_m^{(1)}$ and $Ro_m^{(1)}$ denote the even and odd radial Mathieu functions of the first kind, $Re_m^{(2)}$ and $Ro_m^{(2)}$ denote the even and odd radial Mathieu functions of the second kind, $Re_m^{(4)}$ and $Ro_m^{(4)}$ denote the even and odd radial Mathieu functions of the forth kind, Se_m and So_m denote the angular Mathieu functions, and $H_0^{(2)}$ denotes the Hankel function. The Hankel function can be expanded in series of Mathieu functions [42] according to the formula

$$H_0^{(2)}(k_0 |\vec{\rho} - \vec{c}|) = 4 \sum_{m=0}^{+\infty} \frac{1}{N_m^e} Re_m^{(1)}(q_0, u) Re_m^{(4)}(q_0, u_0) Se_m(q_0, v_0) Se_m(q_0, v) + \sum_{m=0}^{+\infty} \frac{1}{N_m^o} Ro_m^{(1)}(q_0, u) Ro_m^{(4)}(q_0, u_0) So_m(q_0, v) \quad (3.13)$$

$$\begin{aligned}
 E_a &= \sum_{m=0}^{\infty} \left[\left(a_m Re_m^{(1)}(q_1, u) \right) Se_m(q_1, v) \right] + \\
 &+ \sum_{m=1}^{\infty} \left[\left(b_m Ro_m^{(1)}(q_1, u) \right) So_m(q_1, v) \right] \\
 E_b &= \sum_{m=0}^{\infty} \left[\left(c_m Re_m^{(1)}(q_2, u) + d_m Re_m^{(2)}(q_2, u) \right) Se_m(q_2, v) \right] + \\
 &+ \sum_{m=1}^{\infty} \left[\left(e_m Ro_m^{(1)}(q_2, u) + f_m Ro_m^{(2)}(q_2, u) \right) So_m(q_2, v) \right] \\
 E_c &= \sum_{m=0}^{\infty} \left[\left(g_m Re_m^{(4)}(q_3, u) \right) Se_m(q_3, v) \right] + \\
 &+ \sum_{m=1}^{\infty} \left[\left(h_m Ro_m^{(4)}(q_3, u) \right) So_m(q_3, v) \right] - \sum_{i=1}^M \frac{k_0^2 I_i}{4\omega\epsilon_0} H_0^{(2)}(k_0 |\vec{\rho} - \vec{c}|)
 \end{aligned}$$

Figure 3.4: Expressions of the total electric field as series of Mathieu functions inside the different materials of the elliptical model

It is possible to derive the magnetic field starting from the electric field using the relation:

$$\begin{aligned}
 \mathbf{H}(u, v) &= H_u(u, v)\hat{\mathbf{u}} + H_v(u, v)\hat{\mathbf{v}} \\
 &= \frac{j}{\omega\mu d\sqrt{\cosh u^2 - \cos v^2}} \left[u \frac{\partial}{\partial v} - v \frac{\partial}{\partial u} \right] E_z(u, v),
 \end{aligned} \tag{3.14}$$

To have complete information about the spatial distribution of the electric field (and consequently the magnetic field) we need to find the unknown coefficients $a_m, b_m, c_m, d_m, e_m, f_m, g_m$, and h_m . To do that, we need to impose the boundary conditions on the interfaces between different materials: the tangential components of the electric and magnetic fields have to be continuous.

Indicating with D the operator $\frac{\partial}{\partial u}$, for the interface air – skull we have:

$$\begin{aligned}
& \sum_{m=0}^{+\infty} \left[g_m Re_m^{(4)}(q_0, b) Se_m(q_0, v) \right] + \sum_{m=1}^{+\infty} \left[h_m Ro_m^{(4)}(q_0, b) So_m(q_0, v) \right] \\
& - \sum_{m=0}^{+\infty} \left[c_m Re_m^{(1)}(q_b, b) Se_m(q_b, v) + d_m Re_m^{(2)}(q_b, b) Se_m(q_b, v) \right] \\
& - \sum_{m=1}^{+\infty} \left[e_m Ro_m^{(1)}(q_b, b) So_m(q_b, v) + f_m Ro_m^{(2)}(q_b, b) So_m(q_b, v) \right] \\
& = \frac{k_0^2 I_i}{4\omega\epsilon_0} \sum_{i=1}^M I_i \left[4 \sum_{m=0}^{+\infty} \frac{1}{N_m^e} Re_m^{(1)}(q_0, b) Re^{(4)}(q_0, u_i) Se_m(q_0, v_i) Se_m(q_0, v) \right. \\
& \quad \left. + \frac{1}{N_m^0} Ro^{(1)}(q_0, b) Ro_m^{(4)}(q_0, u_i) So_m(q_0, v_i) So_m(q_0, v) \right]
\end{aligned} \tag{3.15}$$

Then, the boundary condition at the interface skull-brain:

$$\begin{aligned}
& \sum_{m=0}^{+\infty} \left[c_m Re_m^{(1)}(q_b, a) Se_m(q_b, v) + d_m Re_m^{(2)}(q_b, a) Se_m(q_b, v) \right] \\
& + \sum_{m=1}^{+\infty} \left[e_m Ro_m^{(1)}(q_b, a) So_m(q_b, v) + f_m Ro_m^{(2)}(q_b, a) So_m(q_b, v) \right] \\
& = \sum_{m=0}^{+\infty} \left[a_m Re_m^{(1)}(q_a, a) Se_m(q_a, v) \right] + \sum_{m=1}^{+\infty} \left[b_m Ro_m^{(1)}(q_a, a) So_m(q_a, v) \right]
\end{aligned} \tag{3.16}$$

we also have 2 more equations, obtained by imposing the boundary conditions on the continuity of the tangential component of the magnetic field. For the interface air-skull:

$$\begin{aligned}
& \sum_{m=0}^{+\infty} \left[g_m DRe_m^{(4)}(q_0, b) Se_m(q_0, v) \right] + \sum_{m=1}^{+\infty} \left[h_m DRo_m^{(4)}(q_0, b) So_m(q_0, v) \right] \\
& - \sum_{m=0}^{+\infty} \left[c_m DRe_m^{(1)}(q_b, b) Se_m(q_b, v) + d_m DRe_m^{(2)}(q_b, b) Se_m(q_b, v) \right] \\
& - \sum_{m=1}^{+\infty} \left[e_m DRo_m^{(1)}(q_b, b) So_m(q_b, v) + f_m DRo_m^{(2)}(q_b, b) So_m(q_b, v) \right] \tag{3.17} \\
& = \frac{k_0^2 I_i}{4\omega\epsilon_0} \sum_{i=1}^M I_i \left[4 \sum_{m=0}^{+\infty} \frac{1}{N_m^e} DRe_m^{(1)}(q_0, b) Re^{(4)}(q_0, u_i) Se_m(q_0, v_i) Se_m(q_0, v) \right. \\
& \quad \left. + \frac{1}{N_m^0} DRo_m^{(1)}(q_0, b) Ro_m^{(4)}(q_0, u_i) So_m(q_0, v_i) So_m(q_0, v) \right]
\end{aligned}$$

At the interface skull-brain

$$\begin{aligned}
& \sum_{m=0}^{+\infty} \left[c_m DRe_m^{(1)}(q_b, a) Se_m(q_b, v) + d_m DRe_m^{(2)}(q_b, a) Se_m(q_b, v) \right] \\
& + \sum_{m=1}^{+\infty} \left[e_m DRo_m^{(1)}(q_b, a) So_m(q_b, v) + f_m DRo_m^{(2)}(q_b, a) So_m(q_b, v) \right] \tag{3.18} \\
& = \sum_{m=0}^{+\infty} \left[a_m DRe_m^{(1)}(q_a, a) Se_m(q_a, v) \right] + \sum_{m=1}^{+\infty} \left[b_m DRo_m^{(1)}(q_a, a) So_m(q_a, v) \right]
\end{aligned}$$

To find the expansion coefficients, as suggested in [20], we use Galerkin's method:

$$\int_0^{2\pi} Se_m(q_i, v) So_n(q_{i+1}, v) dv = 0 \tag{3.19}$$

for any m, n, q_i , and q_{i+1} . We can apply this method multiplying both sides of the equations first by $Se_m(q_i, v)$ and $So_m(q_i, v)$ where q_i represents the q -parameter of one of the materials that is adjacent to the interface of the considered equation. We have to multiply for just one of the adjacent q -parameters and not for both because the integral $\int_0^{2\pi} Se_m(q_i, v) So_n(q_{i+1}, v) dv$ represents the inner product of the two functions $Se_m(q_i, v)$ and $So_n(q_{i+1}, v)$, or equivalently the projection of one function on the functional space of the other: since the Mathieu functions are a complete functional

space basis, the inner product with all the Mathieu functions of one argument is enough to make a complete projection of all the Mathieu functions present in the continuity equations at the interface.

With all the conditions given by this method, we can write the following system of equations:

$$\begin{aligned}
 & g_r Re_m^{(4)}(q_0, b) \int_0^{2\pi} Se_r(q_0, v)^2 dv \\
 & - \sum_{m=0}^{+\infty} \left(c_m Re^{(1)}(q_b, b) + d_m Re_m^{(2)}(q_b, b) \right) \int_0^{2\pi} Se_m(q_b, v) Se_r(q_0, v) dv \quad (3.20a) \\
 & = \frac{k_0^2}{4\omega\epsilon_0} \sum_{i=1}^M I_i \left[4Re^{(1)}(q_0, b) Re_r^{(4)}(q_0, b) Se_r(q_0, v_i) \right]
 \end{aligned}$$

$$\begin{aligned}
 & h_r Ro_m^{(4)}(q_0, b) \int_0^{2\pi} So_r(q_0, v)^2 dv \\
 & - \sum_{m=0}^{+\infty} \left(e_m Ro^{(1)}(q_b, b) + f_m Ro_m^{(2)}(q_b, b) \right) \int_0^{2\pi} So_m(q_b, v) So_r(q_0, v) dv \quad (3.20b) \\
 & = \frac{k_0^2}{4\omega\epsilon_0} \sum_{i=1}^M I_i \left[4Ro^{(1)}(q_0, b) Ro_r^{(4)}(q_0, b) So_r(q_0, v_i) \right]
 \end{aligned}$$

$$\begin{aligned}
 & g_r DRe_m^{(4)}(q_0, b) \int_0^{2\pi} Se_r(q_0, v)^2 dv \\
 & - \sum_{m=0}^{+\infty} \left(c_m DRe^{(1)}(q_b, b) \right. \\
 & \quad \left. + d_m DRe_m^{(2)}(q_b, b) \right) \int_0^{2\pi} Se_m(q_b, v) Se_r(q_0, v) dv \quad (3.20c) \\
 & = \frac{k_0^2}{4\omega\epsilon_0} \sum_{i=1}^M I_i \left[4DRe^{(1)}(q_0, b) Re_r^{(4)}(q_0, b) Se_r(q_0, v_i) \right]
 \end{aligned}$$

$$\begin{aligned}
& h_r D R o_m^{(4)}(q_0, b) \int_0^{2\pi} S o_r(q_0, v)^2 dv \\
& - \sum_{m=0}^{+\infty} \left(e_m D R o^{(1)}(q_b, b) \right. \\
& \quad \left. + f_m D R o_m^{(2)}(q_b, b) \right) \int_0^{2\pi} S o_m(q_b, v) S o_r(q_0, v) dv \\
& = \frac{k_0^2}{4\omega\epsilon_0} \sum_{i=1}^M I_i \left[4 D R o^{(1)}(q_0, b) R o_r^{(4)}(q_0, b) S o_r(q_0, v_i) \right]
\end{aligned} \tag{3.20d}$$

for the interface air-skull, and for the interface skull-brain:

$$\begin{aligned}
& [c_r R e_r(q_b, a) + d_r R e_r(q_b, a)] \int_0^{2\pi} S e_r^2(q_b, v) dv \\
& = \sum_{m=0}^{+\infty} a_m R e_m(q_a, a) \int_0^{2\pi} S e_m(q_a, v) S e_r(q_a, v) dv
\end{aligned} \tag{3.20e}$$

$$\begin{aligned}
& [e_r R o_r(q_b, a) + f_r R o_r(q_b, a)] \int_0^{2\pi} S o_r^2(q_b, v) dv \\
& = \sum_{m=1}^{+\infty} b_m R o_m(q_a, a) \int_0^{2\pi} S o_m(q_a, v) S o_r(q_a, v) dv
\end{aligned} \tag{3.20f}$$

$$\begin{aligned}
& [c_r D R e_r(q_b, a) + d_r D R e_r(q_b, a)] \int_0^{2\pi} S e_r^2(q_b, v) dv \\
& = \sum_{m=0}^{+\infty} a_m D R e_m(q_a, a) \int_0^{2\pi} S e_m(q_a, v) S e_r(q_b, v) dv
\end{aligned} \tag{3.20g}$$

$$\begin{aligned}
& [e_r D R o_r(q_b, a) + f_r D R o_r(q_b, a)] \int_0^{2\pi} S o_r^2(q_b, v) dv \\
& = \sum_{m=1}^{+\infty} b_m D R o_m(q_a, a) \int_0^{2\pi} S o_m(q_a, v) S o_r(q_b, v) dv
\end{aligned} \tag{3.20h}$$

Since the material of the brain is slightly conductive the argument of the Mathieu functions is complex, and algorithms reported in [43] and [12] have been used to compute them.

To evaluate the accuracy of the method, the distribution of the magnetic field in three different geometries has been compared: the 2D analytic solution for two concentric circular cylinders, the 2D analytic solution for two concentric elliptic cylinders, and the cross-section of the head in a 3D numerical solution made by the commercial software XFDTD. The inner cylinder (representing the brain) has permittivity $\epsilon = 53$ and conductivity $\sigma = 0.5$ S/m, while the external one (representing the skull) has thickness equal to 1 cm, permittivity $\epsilon = 35$ and conductivity $\sigma = 0.3$ S/m. The field has been generated by two or four conducting wires positioned parallel to the main axes of the cylinders. The amplitude of the currents is kept constant, and the field distribution deriving by different phase combinations has been explored. The major and minor axes of the elliptic cylinder (20 and 16 cm) match the length of the major axes of the cross section of the head, and the length of the diameter of the circular cylinder changes according to the position of the wires. Consequently, when geometry has 4 wires simulations or more, it is not possible to apply the 2-D circular model since it is not possible to set a unique value of diameter. This is the main advantage of the elliptic model respect to the circular one: we can model our geometry even when the wires are not positioned along only one axis of the head. From Fig. 3.5 we can see that, for all the phase current combinations, using the 2D models it is possible to predict the number and the positions of the spots inside the brain. However, with 2D models we do not have complete knowledge of the field distribution such as the shape of the peaks. The main advantage of the 2D models respect the 3D model is the computation speed: for a simulation with a 4 GB RAM pentium IV PC we need 10 seconds for the 2D circular model, 40 seconds the 2D elliptic model, and 70

minutes for the XFDTD model. Thus, the higher speed makes the 2D models useful in optimization algorithms, or for quick tests during the development process of either a new specific theory or a new algorithm.

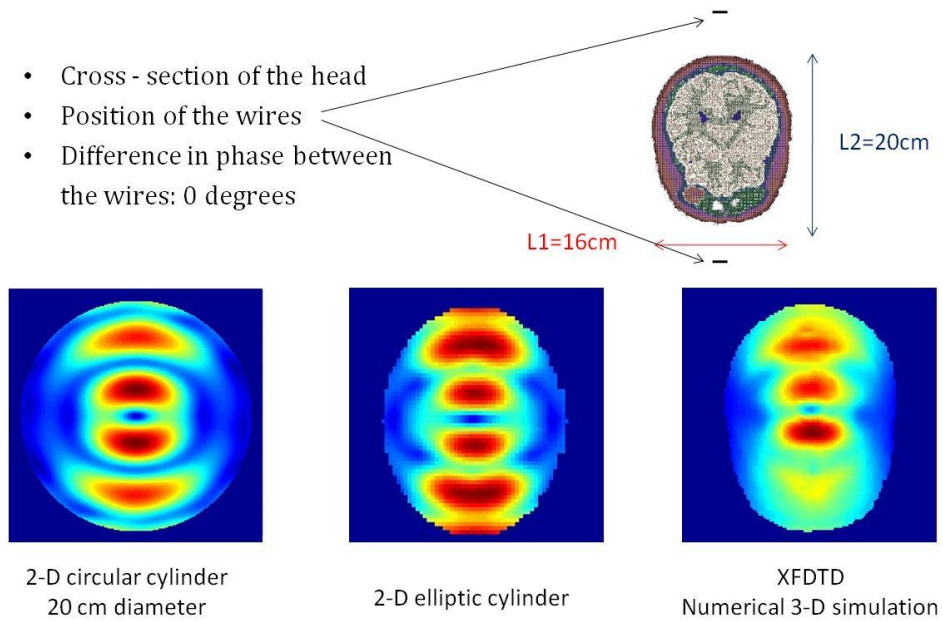


Figure 3.5 (a): Comparison of the magnetic field generated by two wires positioned along the 20 cm axis having 0 degrees in difference in phase.

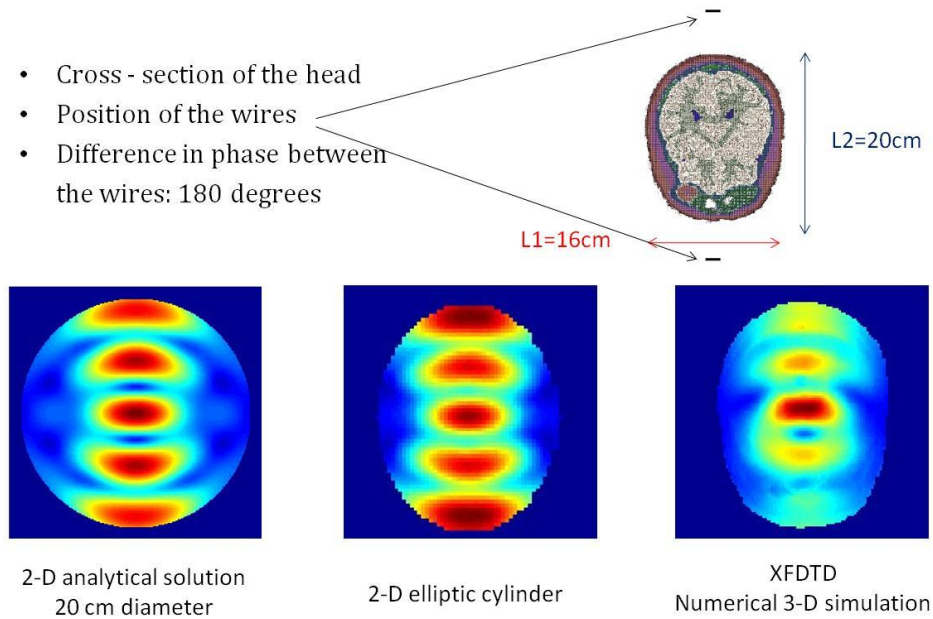


Figure 3.5 (b): Comparison of the magnetic field generated by two wires positioned along the 20 cm axis having 180 degrees in difference in phase.

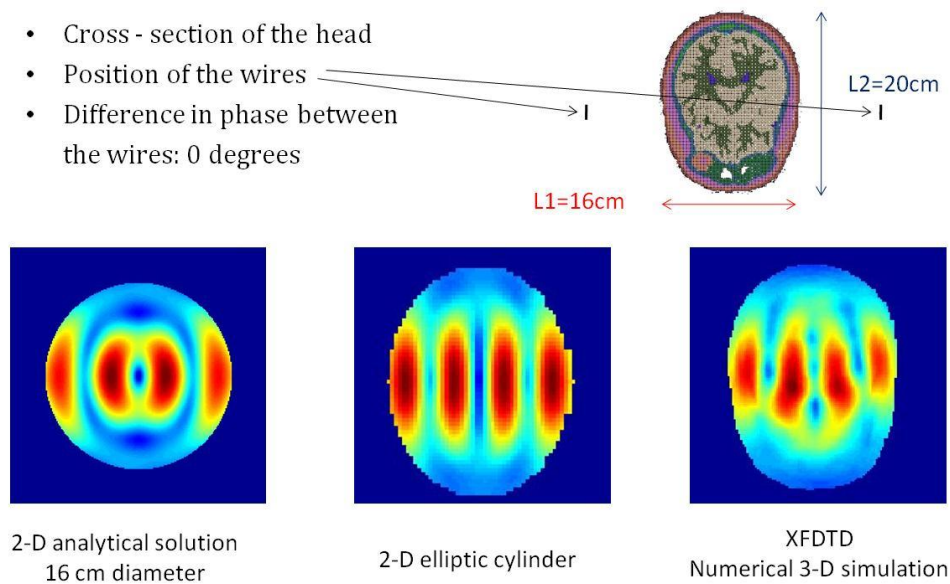


Figure 3.5 (c): Comparison of the magnetic field generated by two wires positioned along the 16 cm axis having 0 degrees in difference in phase.

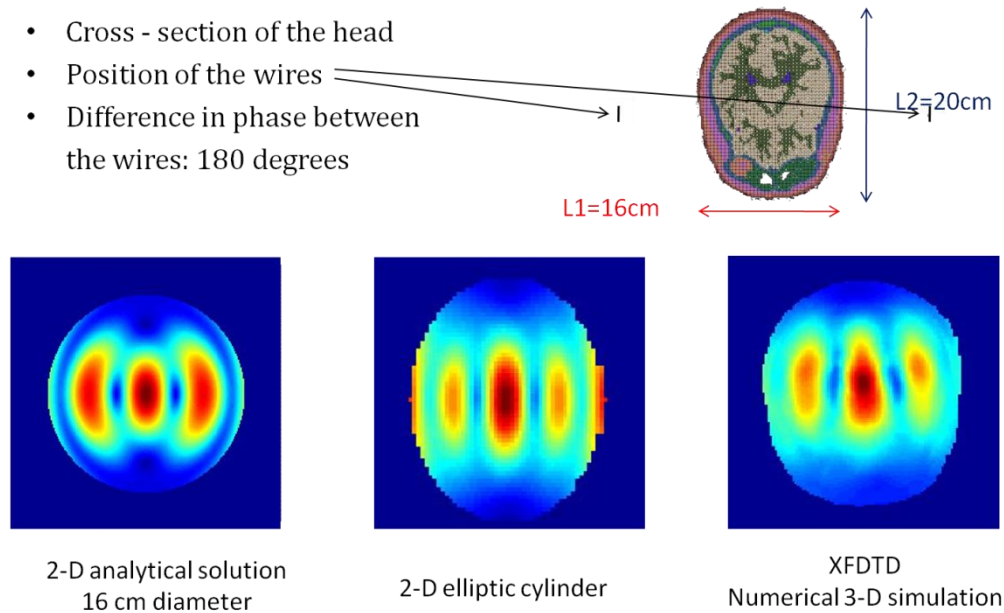


Figure 3.5 (d): Comparison of the magnetic field generated by two wires positioned along the 16 cm axis having 180 degrees in difference in phase.

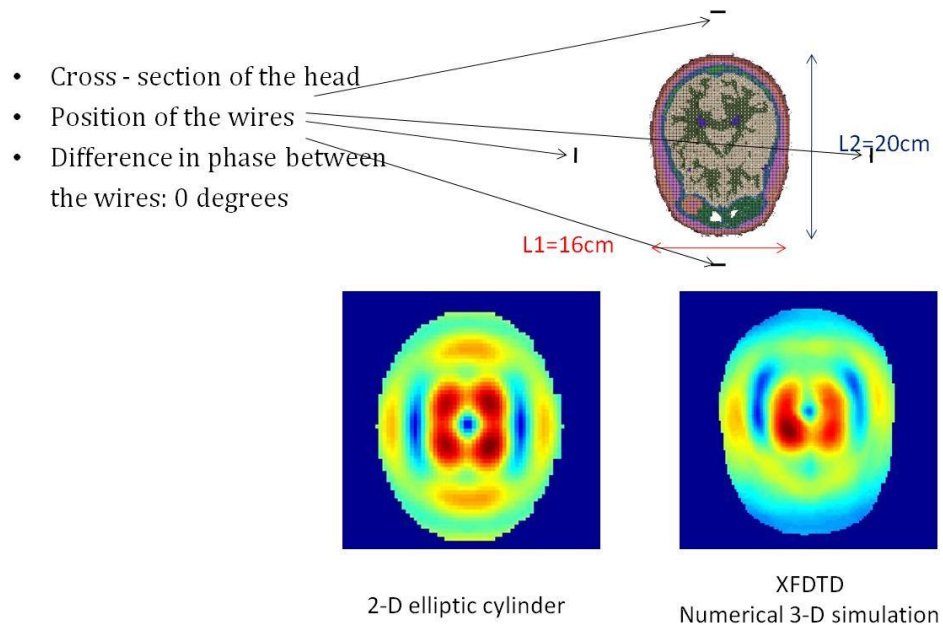


Figure 3.5 (e): Comparison of the magnetic field generated by four wires positioned along the two main axes having 0 degrees in difference in phase.

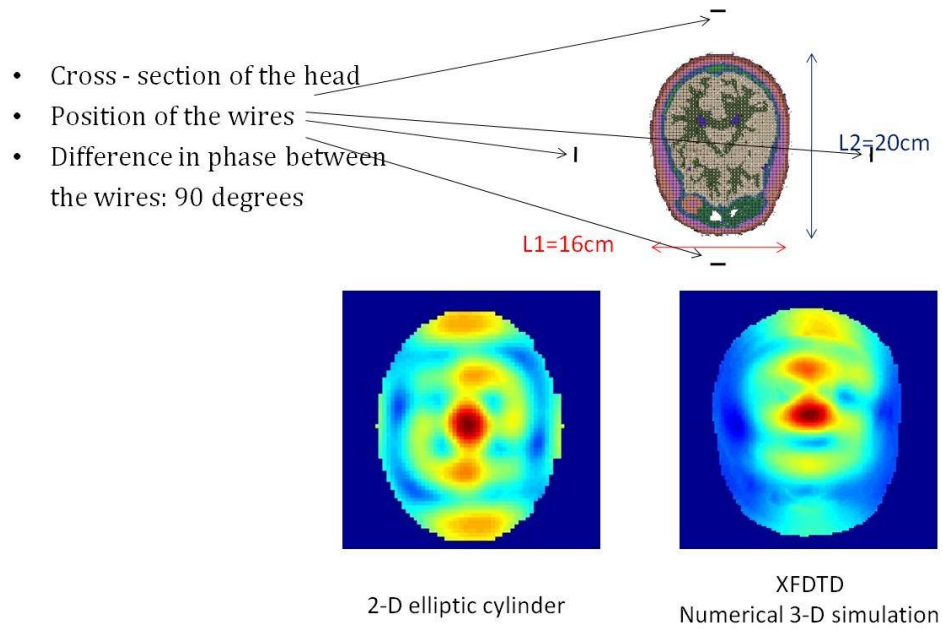


Figure 3.5 (f): Comparison of the magnetic field generated by four wires positioned along the two main axes having 90 degrees in difference in phase.

CHAPTER 4

A FAST ANALYTICAL METHOD TO OPTIMIZE LOCAL TRANSMIT EFFICIENCY

4.1 Introduction

In Chapter 3 we presented two 2-D models to be used in optimization algorithms for RF shimming. Since they are able to predict the position of the peaks of magnetic field given a current scheme, we are focusing on one kind of phased array RF shimming suggested by dr. Ibrahim in [99], that attempts to generate a strong B_1 magnetic field at a specific location. The short computation time of the 2-D models helped to develop an analytical method for the optimization of the field at a specific location. With knowledge of the B_1^+ field distribution generated by each single coil of the transmit array, the optimization method provides the best set of currents to maximize the transmit efficiency for the location of interest, even in presence of strong coupling among the elements of the array.

4.2 The locally optimized B_1 field

For high-field MRI systems, it can be hard to obtain a homogeneous B_1 field in regions having large cross-sections, such as torso or abdomen, while keeping low SAR levels[65]. In some applications it is more advantageous to do RF shimming of the B_1^+ field over a volume smaller than the total volume of the sample: in these cases, the homogeneity of the B_1^+ field is expected to be fairly good across a ROI smaller than about one quarter wavelength. There are several reasons to focus on a localized peak and to not provide a uniform magnetic field B_1 over the cross section:

- 1) It is possible to increase the intensity of the B_1 field in a specific region of interest providing less overall power and in a smaller amount of time.

- 2) It is easier to control the distribution of the SAR in the brain, and consequently it is easier to control the temperature of the patient.

One application of the localized B_1^+ to the prostate has been shown in [89] where a phase-only optimization method has been used. We propose one algorithm that tends not only to force constructive interference between the waves generated by each element of the array but also to optimize the transmit efficiency (magnitude of the B_1^+ field in one specific location over the square root of the transmitted power).

4.3 The optimization of the current phases

Our optimization algorithm is based on the optimization of both phases and amplitudes of the currents of a transmit array. The phases are set to force constructive interference in a specific location among the waves generated by the elements of the array. This can be obtained if the phases of the fields generated by each wire are the same in the location of interest.

Indicating with $B_{1,i,ref}^+$ the circularly polarized component of the B_1 field generated by the i -th element of the transmit array in the ROI at position (x,y,z) when the i -th element is driven with the reference current $I_{i,ref}$, the phase optimization process consists of acquiring the phases of all $B_{1,i,ref}^+$ fields in the position (x,y,z) with a technique of B_1 mapping [120], and adjusting the input phase of the i -th element by an amount equal to the opposite of the measured phase of $B_{1,i}^+$ fields in the position (x,y,z) . The resulting optimal coil current could be written

$$I_i = I_{i,ref} e^{-j\angle B_{1,i,ref}^+(x,y,z)}. \quad (4.1)$$

After this, the phase of $B_1^+(x,y,z)$ from each element will be equal to 0, and all the fields generated by each element of the array will add constructively in the ROI, producing B_1^+ much more efficiently than if destructive interference were to occur there.

4.4 The optimization of the current amplitudes

The phase matching technique for phased arrays reaches maximum efficiency if the spatial amplitude distribution of the field is uniform. In MRI systems the geometry of the problem creates a non-uniform distribution of the amplitude of the magnetic field in the ROI, thus requiring the optimization of the amplitudes of the currents of the transmit array to reach maximum possible efficiency.

If $I_{i,ref}$ is identical for all the elements and equal to I_{ref} , we can write the desired current driving each element of the transmit array as

$$I_i = I_{ref} C A_i e^{-j\angle B_{1,i,ref}^+(x,y,z)}, \quad (4.2)$$

where the optimal current amplitudes A_i are real positive numbers, and C is a normalization factor equal for all the elements of the transmit array. The amplitudes A_i are determined through the optimization of a cost function f that attempts to simultaneously maximize the total B_1^+ field at the desired location (x, y, z) and minimize the transmitted power, which is a parameter that can be measured in an MRI system. By reducing the amount of power required to create a given B_1^+ field in the region of interest, the SAR is reduced, and there is greater flexibility in the imaging parameters (including imaging time) that can be used. It has been observed that limits on local SAR can often be exceeded before those on average SAR will [114]. Interestingly, according to the most recent version of widely-used guidelines [69], when an array of transmit coils is treated as a volume coil there is no limit on local SAR, thus providing another motivation for considering whole body SAR. It is also notable that average SAR is more readily monitored than local SAR [124], making methods to reduce it more amenable to verification in regular use. The value for C can be used to normalize the currents to satisfy, if necessary, some safety requirements such as local average SAR, temperature increase, or to obtain a specific value of flip-angle still keeping the same efficiency in terms of transmitted field B_1^+ and generated power.

The cost function depends on the observables that one is interested in optimizing. In particular, we choose to minimize

$$f = \frac{\sqrt{P_{Tx}}}{|B_1^+(x, y, z)|}. \quad (4.3)$$

where P_{Tx} is the power transmitted through the array. It can be calculated as

$$P_{Tx} = \frac{1}{2} \sum_{k=1}^N \sum_{i=1}^N \text{Re}\{I_i Z_{ik} I_k^*\}, \quad (4.4)$$

where Z_{ik} is the mutual impedance between the i -th and the k -th element, and can be measured with a vector network analyzer.

The definition of the function f contains the square root of the generated power in order to avoid a linear dependence with the currents that generate the fields. We consider two different cases depending upon the coupling among the elements of the transmit array.

4.5 Case 1: negligible mutual coupling.

When the coupling between different elements of the array is small ($|Z_{ik}| \ll |Z_{ii}|$ for all i and all $k \neq i$) the values of the amplitudes that minimize f can be obtained by finding a set of currents that cause the gradient of f to be zero. Specifically, the generated power is approximated as

$$P_{Tx} \approx \frac{1}{2} \sum_{i=1}^N \text{Re}\{Z_{ii}\} |I_i|^2 = \frac{1}{2} C^2 \sum_{i=1}^N \text{Re}\{Z_{ii}\} A_i^2. \quad (4.5)$$

The components of the first derivative are set to 0, yielding

$$\frac{\partial f}{\partial A_i} = \frac{\partial \left(\frac{\sqrt{\frac{1}{2} C^2 \sum_{i=1}^N \text{Re}\{Z_{ii}\} A_i^2}}{\sum_{i=1}^N C A_i B_{1,i}^+} \right)}{\partial A_i} = \sqrt{\frac{1}{2}} \frac{\partial \left(\frac{\sqrt{\sum_{i=1}^N \text{Re}\{Z_{ii}\} A_i^2}}{\sum_{i=1}^N A_i B_{1,i}^+} \right)}{\partial A_i} = 0$$

or equivalently

$$\begin{aligned}
\frac{\partial f}{\partial A_i} &= \sqrt{\frac{1}{2}} \left[\frac{2 \operatorname{Re}\{Z_{ii}\} A_i \sum_{l=1}^N A_l B_{1,l}^+ - B_{1,i}^+ \sqrt{\sum_{l=1}^N \operatorname{Re}\{Z_{ll}\} A_l^2}}{2 \sqrt{\sum_{l=1}^N \operatorname{Re}\{Z_{ll}\} A_l^2} (\sum_{l=1}^N A_l B_{1,l}^+)^2} \right] = 0 \\
\frac{\partial f}{\partial A_i} &= \sqrt{\frac{1}{2}} \left[\frac{\operatorname{Re}\{Z_{ii}\} A_i \sum_{l=1}^N A_l B_{1,l}^+ - B_{1,i}^+ \sum_{l=1}^N \operatorname{Re}\{Z_{ll}\} A_l^2}{\sqrt{\sum_{l=1}^N \operatorname{Re}\{Z_{ll}\} A_l^2} (\sum_{l=1}^N A_l B_{1,l}^+)^2} \right] = 0. \\
A_i &= \frac{B_{1,i,ref}^+}{\operatorname{Re}\{Z_{ii}\}}. \tag{4.6}
\end{aligned}$$

(4.6) is a solution of the equation (4.3).

Therefore, from the measurements of $B_{1,i}^+(x, y, z)$ and Z_{ii} , the optimal amplitudes A_i that minimize the cost function f at the desired location (x, y, z) can be determined immediately. If a value for C is added that brings B_1^+ back to its original strength, a physical interpretation of this solution is seen when observing that the effect is to increase the driving current of the elements that contribute to the B_1^+ field amplitude at (x, y, z) most efficiently and reduce the driving current of the elements that do so least efficiently.

4.6 Case 2: mutual coupling non negligible.

If the coupling among the elements of the array is non negligible, we will use linear algebra operations to solve an equation similar to (4.6) in Case 1 (negligible mutual coupling).

If we call \mathbf{Z} the impedance matrix, \mathbf{A} the currents vector, and \mathbf{B}_1^+ the vector containing the values of the circularly polarized field B_1 generated by each element of the array, we can rewrite eq. (4.3) as

$$f = \frac{\sqrt{\frac{1}{2} \mathbf{A}^{*T} \mathbf{Z} \mathbf{A}}}{|\mathbf{B}_1^{+T} \mathbf{A}|} \tag{4.7}$$

Let us write

$$\mathbf{Z} = \mathbf{Z}_1 + i\mathbf{Z}_2 \quad (4.8)$$

where

$$\mathbf{Z}_1 = \text{Re}\{\mathbf{Z}\} \quad (4.9a)$$

$$\mathbf{Z}_2 = \text{Im}\{\mathbf{Z}\} \quad (4.9b)$$

Since \mathbf{Z} is symmetric, also \mathbf{Z}_1 and \mathbf{Z}_2 are symmetric too, and both \mathbf{Z}_1 and \mathbf{Z}_2 have all real elements.

With the definitions in eq. (4.9a) and (4.9b) we can rewrite eq. (4.7) as

$$f = \frac{\sqrt{\frac{1}{2} \text{Re}\{\mathbf{A}^{*T} \mathbf{Z}_R \mathbf{A} + i \mathbf{A}^{*T} \mathbf{Z}_I \mathbf{A}\}}}{|\mathbf{B}_1^{+T} \mathbf{A}|} = \frac{\sqrt{\frac{1}{2} \text{Re}\{\mathbf{A}^{*T} \mathbf{Z}_R \mathbf{A}\} + \frac{1}{2} \text{Re}\{i \mathbf{A}^{*T} \mathbf{Z}_I \mathbf{A}\}}}{|\mathbf{B}_1^{+T} \mathbf{A}|} \quad (4.10)$$

We can decompose both the matrices \mathbf{Z}_R and \mathbf{Z}_I through the use of the eigenvector matrices \mathbf{Q}_R and \mathbf{Q}_I

$$\mathbf{Z}_R = \mathbf{Q}_R^{-1} \mathbf{D}_R \mathbf{Q}_R \quad (4.11)$$

$$\mathbf{Z}_I = \mathbf{Q}_I^{-1} \mathbf{D}_I \mathbf{Q}_I \quad (4.12)$$

where \mathbf{D}_R and \mathbf{D}_I are diagonal matrices containing the eigenvalues of the matrices \mathbf{Z}_R and \mathbf{Z}_I .

Since \mathbf{Z} is symmetric, \mathbf{Z}_R and \mathbf{Z}_I are symmetric too, and since both \mathbf{Z}_R and \mathbf{Z}_I have all real elements,

$\mathbf{Q}_R^{-1} = \mathbf{Q}_R^{*T}$ and $\mathbf{Q}_I^{-1} = \mathbf{Q}_I^{*T}$. Thus,

$$f = \frac{\sqrt{\frac{1}{2} \text{Re}\{\mathbf{A}^{*T} \mathbf{Z}_R \mathbf{A}\} + \frac{1}{2} \text{Re}\{i \mathbf{A}^{*T} \mathbf{Z}_I \mathbf{A}\}}}{|\mathbf{B}_1^{+T} \mathbf{A}|} = \frac{\sqrt{\frac{1}{2} \text{Re}\{\mathbf{A}^{*T} \mathbf{Q}_R^{*T} \mathbf{D}_R \mathbf{Q}_R \mathbf{A}\} + \frac{1}{2} \text{Re}\{i \mathbf{A}^{*T} \mathbf{Q}_I^{*T} \mathbf{D}_I \mathbf{Q}_I \mathbf{A}\}}}{|\mathbf{B}_1^{+T} \mathbf{A}|} \quad (4.13)$$

We can write $\mathbf{A}^{*T} \mathbf{Q}_R^{*T} = (\mathbf{Q}_R \mathbf{A})^{*T}$ and $\mathbf{A}^{*T} \mathbf{Q}_I^{*T} = (\mathbf{Q}_I \mathbf{A})^{*T}$

$$f = \frac{\sqrt{\frac{1}{2} \text{Re}\{(\mathbf{Q}_R \mathbf{A})^{*T} \mathbf{D}_R (\mathbf{Q}_R \mathbf{A})\} + \frac{1}{2} \text{Re}\{i (\mathbf{Q}_I \mathbf{A})^{*T} \mathbf{D}_I (\mathbf{Q}_I \mathbf{A})\}}}{|\mathbf{B}_1^{+T} \mathbf{A}|} = \frac{\sqrt{\frac{1}{2} \text{Re}\{(\mathbf{Q}_R \mathbf{A})^{*T} \mathbf{D}_R (\mathbf{Q}_R \mathbf{A})\}}}{|\mathbf{B}_1^{+T} \mathbf{A}|} \quad (4.14)$$

because the product $(\mathbf{Q}_I \mathbf{A})^{*T} \mathbf{D}_I (\mathbf{Q}_I \mathbf{A})$ in eq. (4.14) is real since it is a quadratic form and the eigenvalues of \mathbf{D}_I are real. Thus, $i(\mathbf{Q}_I \mathbf{A})^{*T} \mathbf{D}_I (\mathbf{Q}_I \mathbf{A})$ is purely imaginary, and $\text{Re}\{i(\mathbf{Q}_I \mathbf{A})^{*T} \mathbf{D}_I (\mathbf{Q}_I \mathbf{A})\}$ is null.

We can rewrite the denominator of eq. (4.14)

$$|\mathbf{B}_1^{+T} \mathbf{A}| = |\mathbf{B}_1^{+T} \mathbf{I} \mathbf{A}| \quad (4.15)$$

where \mathbf{I} is the identity matrix. By definition of inverse of a matrix

$$|\mathbf{B}_1^{+T} \mathbf{I} \mathbf{A}| = |\mathbf{B}_1^{+T} \mathbf{Q}_R^{-1} \mathbf{Q}_R \mathbf{A}| \quad (4.16)$$

By defining $\mathbf{E} = \mathbf{Q}_R \mathbf{A}$ and $\mathbf{F} = \mathbf{B}_1^{+T} \mathbf{Q}_R^{-1}$, we have

$$f = \frac{\sqrt{\frac{1}{2} \text{Re}\{\mathbf{E}^{*T} \mathbf{D}_R \mathbf{E}\}}}{|\mathbf{F} \mathbf{E}|} \quad (4.17)$$

The minimization of eq. (4.17) is equivalent to what we have done in Case 1, where the new currents vector is the vector \mathbf{E} , the new impedance matrix is given by \mathbf{D} (that is equivalent to an impedance matrix with no coupling since it is a diagonal matrix), and the new vector of the magnetic field is \mathbf{F} . With these new definitions, we can use eq. (4.6) to find the values of \mathbf{E} that minimize eq. (4.17).

Once the \mathbf{E} vector has been determined, the final current vector \mathbf{A} is simply obtained by multiplying

$$\mathbf{A} = \mathbf{Q}^{-1} \mathbf{E} \quad (4.17)$$

4.7 The parameter α

It is possible to visualize the improvement on the magnetic field and on the generated power given by the amplitude optimization respect to the phase-only optimization of the field in the location (x, y, z) by setting the value of the currents as

$$I_i = C \left| \frac{B_{1,i}^+}{\text{Re}\{Z_{ii}\}} \right|^\alpha e^{-j \angle B_{1,i}^+ (x,y,z)} \quad (4.18)$$

By defining the currents as in eq. (4.18) we maintain an intuitive connection to the cases discussed so far: the both amplitude and phase optimization corresponds to the unique solution $\alpha = 1$, while the phase-only optimization corresponds to $\alpha = 0$.

4.8 **Evaluation of the algorithm**

The performance of this algorithm was compared with two other methods to compute the coil currents: 1) the distribution for a birdcage coil in ideal mode 1 resonance and 2) a phase-only optimization published previously [89]. Comparisons included examinations of the magnitude of the B_1^+ field in the ROI for a given P_{Tx} , and also of the P_{Tx} required to produce a given B_1^+ , for both the negligible and the non negligible coupling cases. In all cases, the field distributions and impedance matrices were computed numerically at 300 MHz for a body-sized 8-element array of stripline elements spaced equidistantly on the surface of a cylinder within a large cylindrical shield and loaded with a human body model positioned with its heart near the center of the array (Fig. 4.1). All numerical simulations were performed using a commercially available full-wave electromagnetic field simulator (XFDTD; Remcom, Inc.; State College, PA; USA). In the comparisons, the optimized coil currents were normalized by changing the value of the constant C in eq. (4.2) so that either P_{Tx} or B_1^+ (as desired) in the ROI was the same for all three cases.

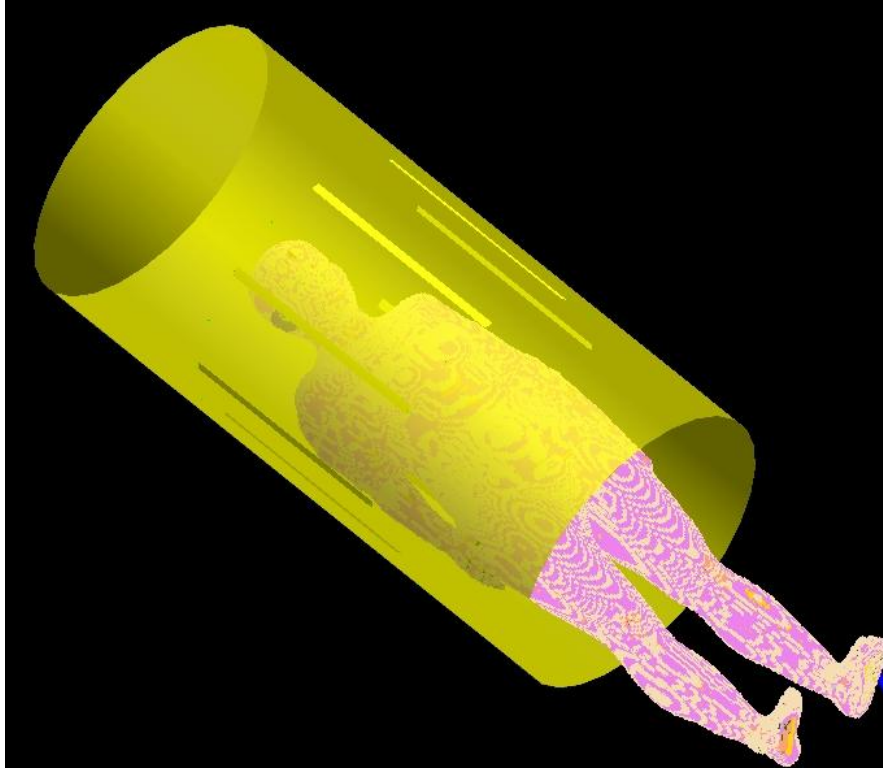


Figure 4.1: Geometry of the model used in simulations: a body-sized 8-element array of stripline elements spaced equidistantly on the surface of a cylinder within a large cylindrical shield and loaded with a human body model positioned with its heart near the center of the array.

For the uncoupled case, fields were used as computed and as if the coupling matrix was the identity matrix. For the case with significant coupling, the calculated fields were coupled with an arbitrarily selected coupling matrix (Fig. 4.2). The comparisons were performed considering a cubic ROI 5mm on each side placed both in the heart (centrally located) and in the arm (peripherally located).

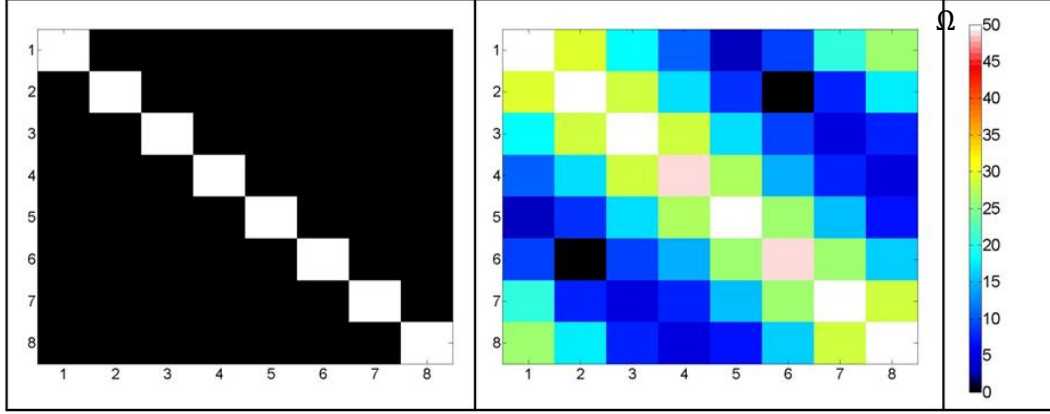


Figure 4.2: Plot of the amplitude of the impedance matrix of the transmit array in case of weak coupling (left) and strong coupling (right).

When there is negligible coupling among the elements, Table (4.1) gives $|B_1^+|$ for each target ROI in each of three current distributions normalized to produce a power P_{Tx} of 1 kW. For an ROI near the heart, the proposed algorithm for optimizing transmit efficiency considering both amplitude and phase of each current element produces a $|B_1^+|$ field having amplitude 2.20 times larger than that of the birdcage coil and 1.07 times larger than that of the phase-only optimization. For an ROI in the arm, the proposed algorithm produces a $|B_1^+|$ field having amplitude 2.50 times larger than that of the birdcage coil and 1.79 times larger than that of the phase-only optimization.

	$ B_1^+ $ for a ROI near heart (μT)	$ B_1^+ $ for ROI in shoulder (μT)
Birdcage coil	0.082	0.280
Phase-only Optimization	0.169	0.391
Optimization with phase and amplitude	0.180	0.699

Table 4.1. Magnitude of the B_1^+ field produced by three different current distributions including optimizations for an ROI near the heart and in the shoulder for a transmit array having negligible coupling among its elements. In each case P_{Tx} is about 1kW.

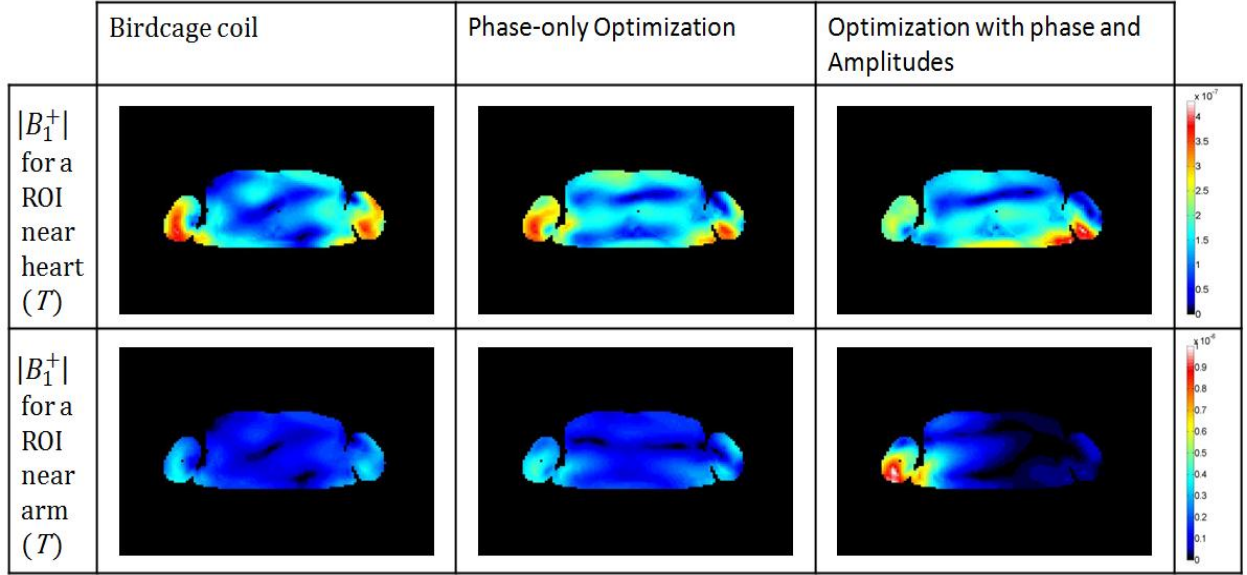


Figure 4.3: Comparison of the spatial distribution of the magnetic field $|B_1^+|$ obtained with the transmit array having all the elements weakly coupled among them, and with the driving currents equal to the three compared methods. For the same location of interest, the three $|B_1^+|$ field distributions have been normalized so that the total generated power by the transmit array is the same.

When the coupling among the array elements must be accounted for, Table 4.2 gives the $|B_1^+|$ for each target ROI in each of three current distributions normalized to produce the same P_{Tx} . For an ROI near the heart, the proposed algorithm for optimizing transmit efficiency considering both amplitude and phase of each current element produces a $|B_1^+|$ field having amplitude 1.92 times larger than that of the birdcage coil and 1.81 times larger than that of the phase-only optimization. For an ROI in the arm, the proposed algorithm produces a $|B_1^+|$ field having amplitude 2.36 times larger than that of the birdcage coil and 1.71 times larger than that of the phase-only optimization.

	$ B_1^+ $ for a ROI near $heart_t$ (μT)	$ B_1^+ $ for ROI in shoulder (μT)
Birdcage coil	0.100	0.331
Phase-only Optimization	0.163	0.456
Optimization with phase and amplitude	0.192	0.780

Table 4.2. Magnitude of the B_1^+ field produced by three different current distributions including optimizations for an ROI near the heart and in the shoulder for a transmit array having non negligible coupling among its elements. In each case P_{Tx} is about 1kW.

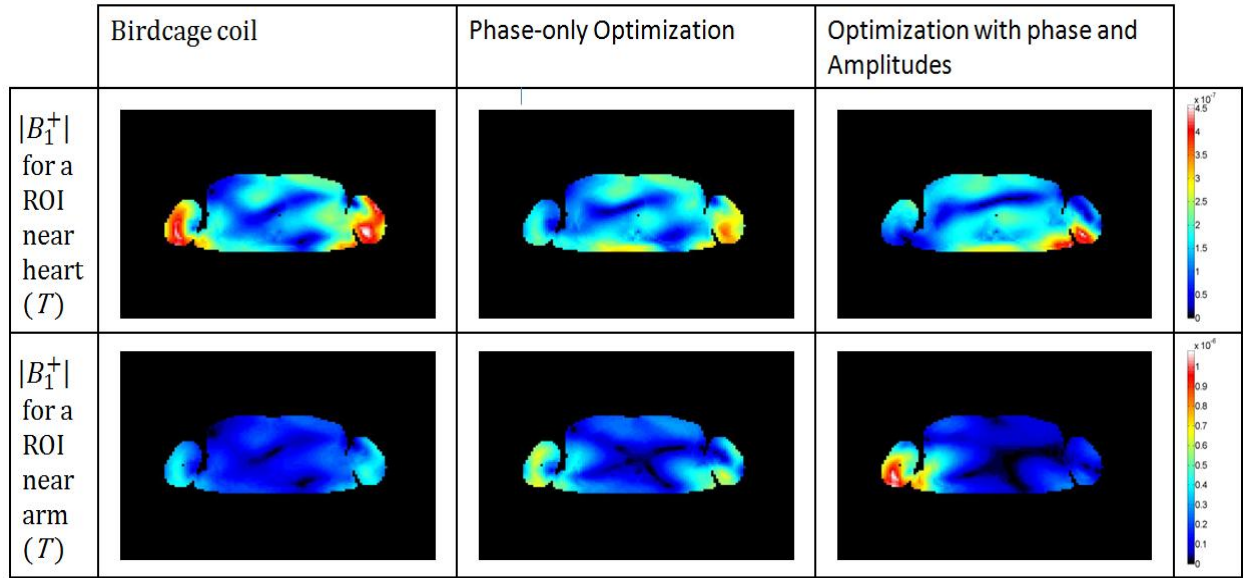


Figure 4.4: Comparison of the spatial distribution of the magnetic field $|B_1^+|$ obtained with the transmit array having all the elements strongly coupled among them, and with the driving currents equal to the three compared methods. For the same location of interest, the three $|B_1^+|$ field distributions have been normalized so that the total generated power by the transmit array is the same.

Using these same numbers it is also possible to determine the power required to produce a given $|B_1^+|$ in each case. In the case of negligible coupling, for an ROI near the heart, the proposed algorithm will require 0.207 times the power required by a birdcage coil and 0.877 times the power required by the phase-only optimization, while it will require 0.271 times the power required by a

birdcage coil and 0.846 times the power required by the phase-only optimization for the case of non negligible coupling.

For an ROI in the shoulder, when the coupling is negligible, the proposed algorithm will require 0.160 times the power required by a birdcage coil and 0.312 times the power required by the phase-only optimization, while it will require 0.183 times the power required by a birdcage coil and 0.342 times the power required by the phase-only optimization when the coupling needs to be accounted for.

Fig. 4.3 and Fig. 4.4 show the spatial distribution of the B_1^+ field of the current schemes described in Table 4.1 and Table 4.2. In regions near the center of the torso this method is seen to perform slightly better than a previously published analytically-based phase-only optimization. Away from the center of the array and sample the improvement over the phase-only optimization is more dramatic. This is to be expected, as far from the center of the array some elements are likely to transmit much more efficiently than others, increasing the value of magnitude-and-phase optimization. Nonetheless, Fig. 4.5 shows the gain in percentage that is possible to obtain for the selected geometry with our proposed optimization algorithm, respect to the birdcage coil for all the voxels of the cross section of the sample.

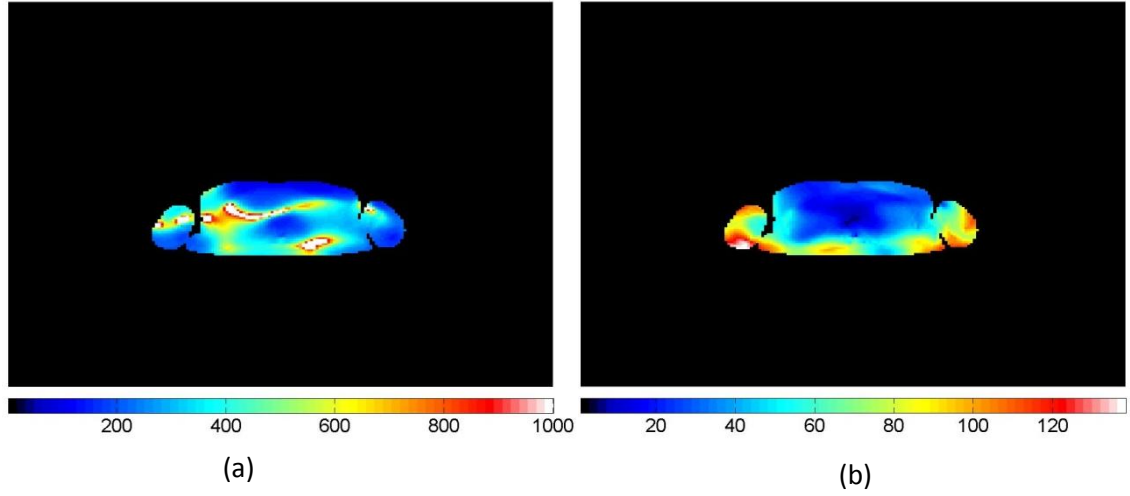


Figure 4.5: Comparison of the maximum gain in percentage obtainable with the optimization of both amplitudes and phases respect the birdcage coil (a), and the phase-only optimization (b).

In addition, it is interesting to notice that when the coupling among the elements of the array is non negligible the algorithm provides a set of phases of the elements of the array different from the ones obtained by the method described in [89] that only tends to force a constructive interference among the fields. On the contrary, since the algorithm tends to maximize the power considering the mutual coupling among the elements of the array, the optimum phases are different from the ones that guarantee maximum constructive interference.

4.9 Comparisons using the parameter α

It is also possible to compare the phase-only and the amplitude optimization methods analyzing how the $|B_1^+|$ field, the transmitted power, and consequently the cost function f , change using the α parameter defined in eq. (4.18): $\alpha = 0$ corresponds to the phase-only optimization, and $\alpha = 1$ corresponds to the both amplitude and phase optimization. It is interesting to notice that for low values of α the power decreases while the B_1^+ field increases. This power decreasing is due to

the reduction of the values of the currents that contribute the least to the field in the interested location. For larger values of α the power increases more quickly than the field because it has a quadratic dependence on the current amplitudes. As already shown, the optimum value is reached for $\alpha = 1$.

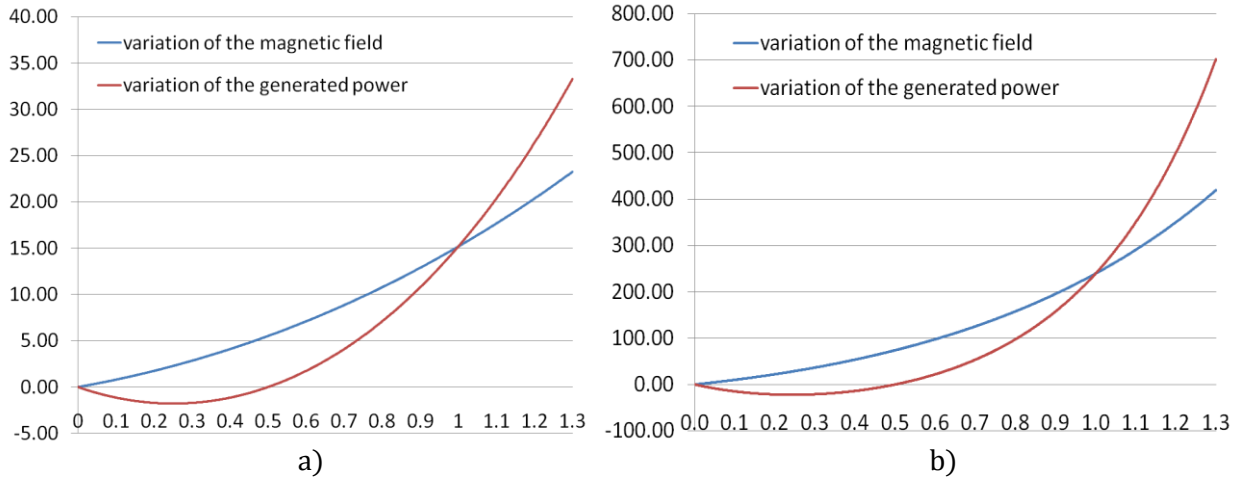


Figure 4.6: Percentage variation of the \mathbf{B}_1^+ field (blue) and the generated power (red) respect to parameter α in eq. (4.18) for an optimized location close to the heart (a), and close to the arm (b).

It is also interesting to notice that, keeping the intuitive interpretation of the result found in Case 1, eq. (4.6) allows to find a value of the currents in presence of strong coupling among the elements of the array (Case 2) close to the optimum in eq. (4.17), with a simple optimization of only one parameter, the parameter α , avoiding the diagonalization method explained in Case 2. In fact, with a simple exhaustive search of the parameter α , requiring less than 0.1s on an ordinary desktop computer with no special optimization of the routine for speed, it was seen that the final result for the cost function was never worse than that obtained with the analytical matrix method by more than 0.1%. For both ROIs, the final value for α was found to be within a few percent of 1.0 (Fig.

(4.7)). This is an additional confirmation of the physical interpretation given to the analytical results of the optimization method.

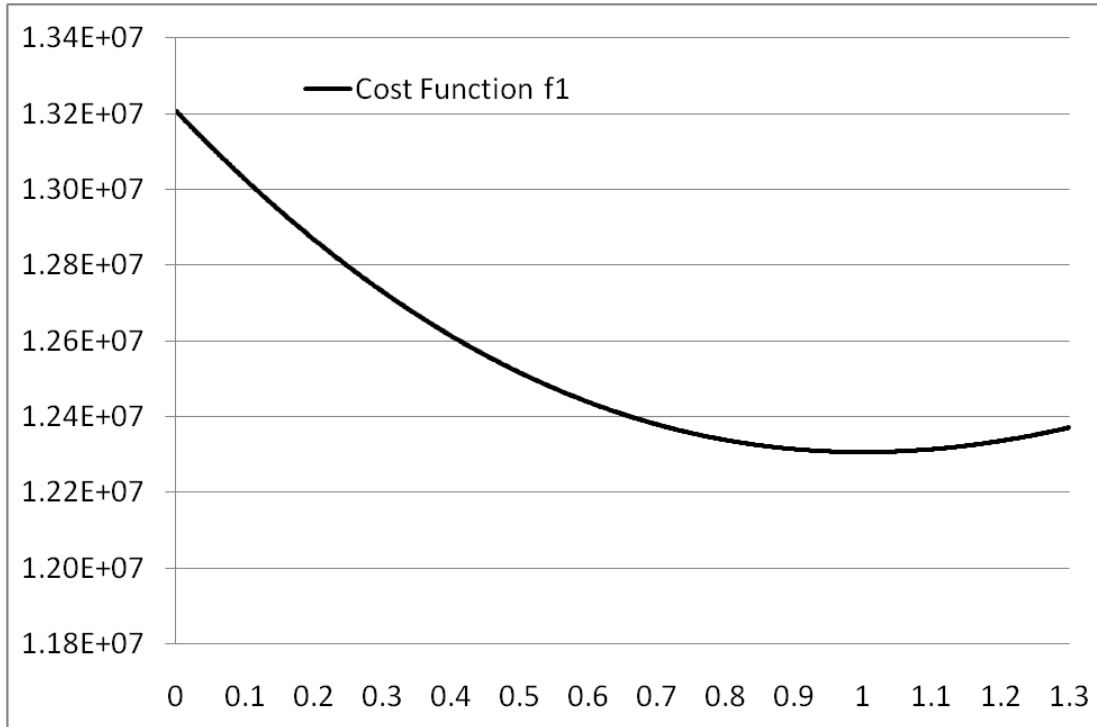


Figure 1.7: Plot of the variation of the cost function f respect to the parameter α for a location close to the heart. It is possible to see the improvement in the cost function when α becomes closer to 1 respect to the case of the phase-only optimization that corresponds to $\alpha=0$.

4.10 The factor C

In eq. (4.2) the factor C has been defined as a normalization constant able to set a specific value of flip angle, or able to satisfy some safety requirements still keeping the same efficiency in terms of optimum $|B_1^+|$ field and generated power given by the method explained in this Chapter. In the next Chapters we will focus in examining in more detail some of the safety requirements for RF

fields in MRI systems and we will present a new fast algorithm able to predict temperature increase in the body given a SAR distribution.

CHAPTER 5

A METHOD TO COMPUTE LOCAL AVERAGE SAR BASED ON ADAPTIVE SPHERICAL MASKS

5.1 Introduction

In the next two Chapters we will focus on some safety limits that an MRI system needs to satisfy. Specifically in Chapter 5 a new method on computing local average SAR is presented, while a new method in computing temperature increase is introduced in Chapter 6. For the local average SAR, compared to the method implemented in most of the commercially available RF simulators for biological applications, our method uses a spherical adaptive mask: spherical to provide higher accuracy because closer voxels are included in the averaging volume, and adaptive to avoid discontinuities in the results when the center voxels are close to the air boundaries.

5.2 Safety requirements

Exposure of body tissues to radiofrequency fields may increase their temperature. The heat is generated by the induced currents due to the interactions between the electromagnetic fields and the materials. These interactions are estimated by a parameter called specific energy absorption rate (SAR) expressed as W per kg of tissue mass. For each location r , it is possible to compute the SAR using the formula

$$SAR(r) = \frac{\sigma(r)|E(r)|^2}{\rho(r)} \quad (5.1)$$

where σ is the conductivity, E the electric field and ρ the mass density.

In MRI systems, the RF fields used to generate the B_1 field need to satisfy some safety requirements to prevent drastic change in temperature in body tissues that may cause serious

damages. Some limits have been imposed to SAR values to indirectly control the possible temperature increase into the body: these limits involve the local peak of SAR, the peak of the averaged SAR on a tissue volume of either 1 gram or 10 grams mass, the total absorbed SAR. Additional limits are also imposed to local maximum temperature increase. These safety limits also change according to the kind of coil used to generate the B_1 field, and which tissue is exposed to RF fields[69].

Thus, given a B_1 field distribution, it is necessary to know if it exceeds the safety requirements, and this can be mainly done either by analyzing the electric fields distribution computed by numerical simulators [32]. In case of presence of transmit arrays that require optimizations based on SAR monitoring, a compression method able to reduce the number of voxels to monitor SAR while changing the currents scheme has been presented in [83, 48]. This is particularly useful in case of SAR average monitor because the averaging operation is time consuming, especially for transmit arrays design. Local average SAR limits are imposed mainly because:

- average operations bevel the spatial edges of the SAR distribution, and temperature distribution is similar to the smoothed original SAR distribution. Thus, local averaged SAR is correlated to the temperature increase distribution due to SAR deposition.
- unaveraged SAR is highly influenced by the meshgrid resolution. Hence, it is easier to impose safety limits on volumes that include more voxels, overcoming the difference in meshgrid resolution.

5.3 The cubical average SAR

Some of the commercially available RF numerical simulators (for example XFDTD (Remcom, Inc.; State College, PA; USA)) have built-in algorithms able to compute the local n-gram average SAR. These algorithms are based on the method presented in [68], where a cubical volume

centered in the location of interest is expanded in all directions until a cubical volume including n -grams mass (with an error of less than 5%) is reached. If the cubical volume has no surface boundaries extending beyond the most exterior surface of the body the method marks the center voxel as valid, and all the other voxels included in the averaging volume as used. On the contrary, if the cubical volume has surface boundaries extending the surface of the body, the assigned value of the SAR average is equal to the maximum SAR average value of the valid voxels whose cubical averaging volume includes the location of interest. In case a voxel is not part of any valid averaging process (i.e. it was never marked as used), it is marked as “unused” and a proper cubical volume is built around that voxel that expands until it finds the total required mass, regardless of the amount of air enclosed in that.

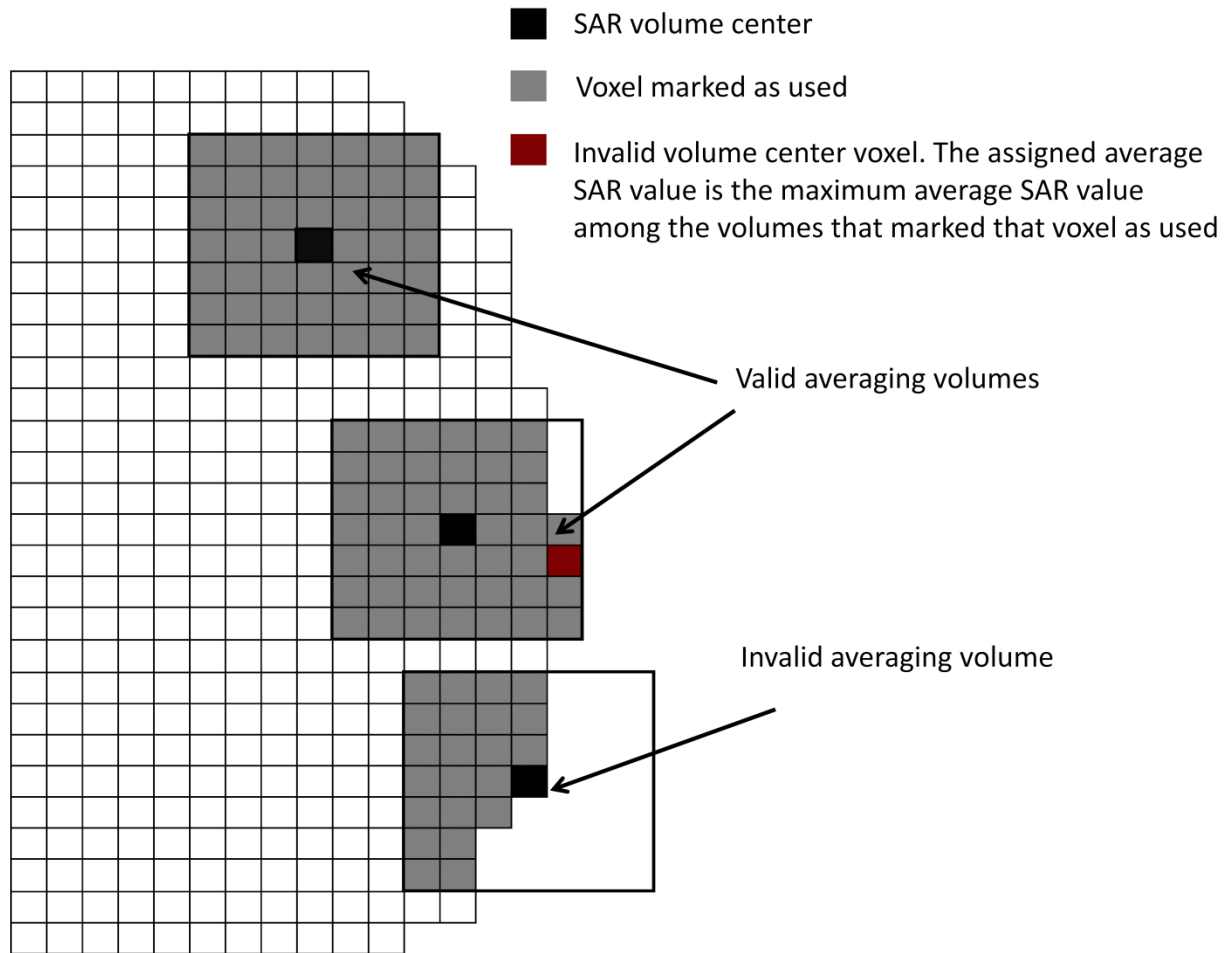


Figure 5.1: Examples of averaging volumes. In the upper square the average SAR is calculated using the gray voxels and the calculated value is assigned to the center volume in black. In the middle square the average SAR is calculated using the cubical volume built around the black voxel and it is also assigned to the voxel in red because it is not possible to build a cubical volume centered in the red voxel and that does not have a boundary surface with at least one voxel internal to the body. In the bottom square the built volume is invalid because it has an external surface with no voxels internal to the body.

The described average SAR method is applied to the SAR distribution generated by a birdcage coil on a box of water. The fields distribution is computed with the numerical simulator XFDTD, having a meshgrid size of $2 \times 2 \times 2 \text{ mm}^3$. The results are shown in Fig. 5.5(a).

It is evident that the computed averaged SAR is not continuous: this is due to the structure of the average method, which assigns to the most external voxels the highest value of the “valid” averaged volumes. This is problematic when the method is applied to large average mass volumes (i.e. 10 g average), due to the big size of the averaging mask, resulting in more voxels being assigned an averaged SAR volume that is not centered on them. This may cause lack of accuracy, especially in the external voxels, which are the most relevant for safety, because they are the closest voxels to the coils and, consequently, the most exposed to high RF fields.

5.4 The spherical average SAR

To overcome the described problem, we proposed a new method to compute the average SAR. In designing the new method, we decided:

- to change the shape of the averaging volumes from cubical to spherical (a pixelated sphere) to minimize the distance between the voxels of the volume and the center. This provides a higher accuracy in the averaging method because the closest voxels to the location of interest are part of the averaging volume.
- to use adaptive geometry masks. They are obtained not imposing any condition on the surfaces of the averaging volumes. They are expanded unconditionally with spherical shapes until the volume includes the required mass: during the expansion, the voxels external to the tissues are simply excluded by the averaging mask. In this way, we are able to overcome the limit of the traditional method of the average SAR computation when the voxel is close to the boundaries of the body (the most relevant locations for safety analysis), because for each voxel an adaptive n-grams mask is built around the interested location.

The algorithm sequentially increases the radius of a spherical mask around the interested voxel: the mask calculates the mass and the SAR of all the voxels of the most external layer. When the total weight (external layer + inner ones) is bigger than n-grams, the algorithm stops, and the

SAR of the external layer is weighted to reach exactly the desired n -grams mass. Indicating with n_{out} the mass of the external layer, with n_{in} the mass of the internal layer, and with n the required averaging mass, the average SAR is given by:

$$SAR_{ng} = \frac{\left(\frac{n - n_{in}}{n_{out}}\right) \sum(SAR \text{ in external voxels}) + \sum(SAR \text{ in internal voxels})}{\left(\frac{n - n_{in}}{n_{out}}\right) \sum(\text{number external voxels}) + \sum(\text{number internal voxels})} \quad (5.2)$$

For example, if we are interested in computing the 10 g average SAR, the mass of the internal layers is 9 grams, and the mass of the most external layer is 4 grams, only the 25 % of the SAR in the external layer contributes to the average SAR, so that the 25 % of the mass of the external layer, summed to the 9 grams of the internal layers, completes the required mass.

$$SAR_{10g} = \frac{\frac{1}{4} \sum(SAR \text{ in external voxels}) + \sum(SAR \text{ in internal voxels})}{\frac{1}{4} \sum(\text{number external voxels}) + \sum(\text{number internal voxels})} \quad (5.3)$$

In the count of both the internal and the external voxels, only the voxels belonging to the body are considered.

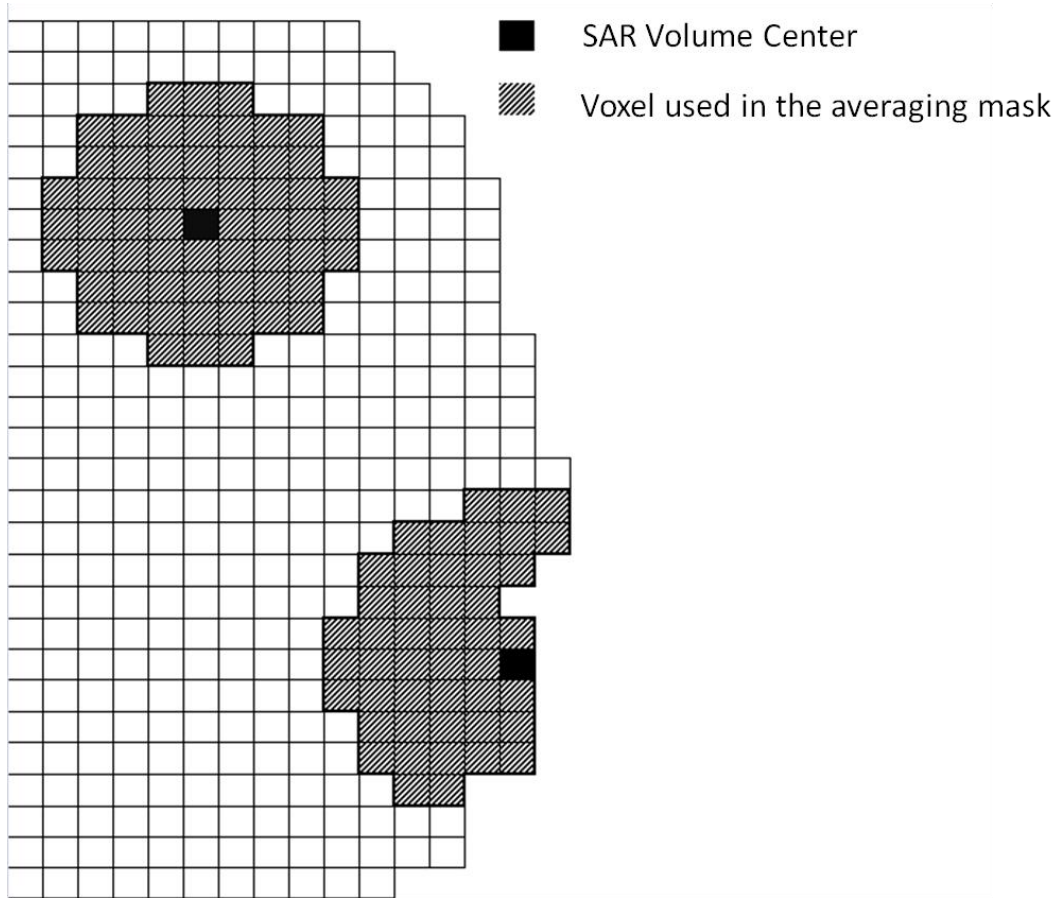


Figure 5.2: examples of averaging volumes. In the upper volume center the average SAR is calculated using the gray voxels and the calculated value is assigned to the center volume in black. In the lower volume square the average SAR is calculated using the expanding spherical volume in the sample, built around the black voxel. In this way, we are able to adapt the mask of the object to the geometry of the sample, and each voxel of the sample is potentially a valid average SAR Volume Center.

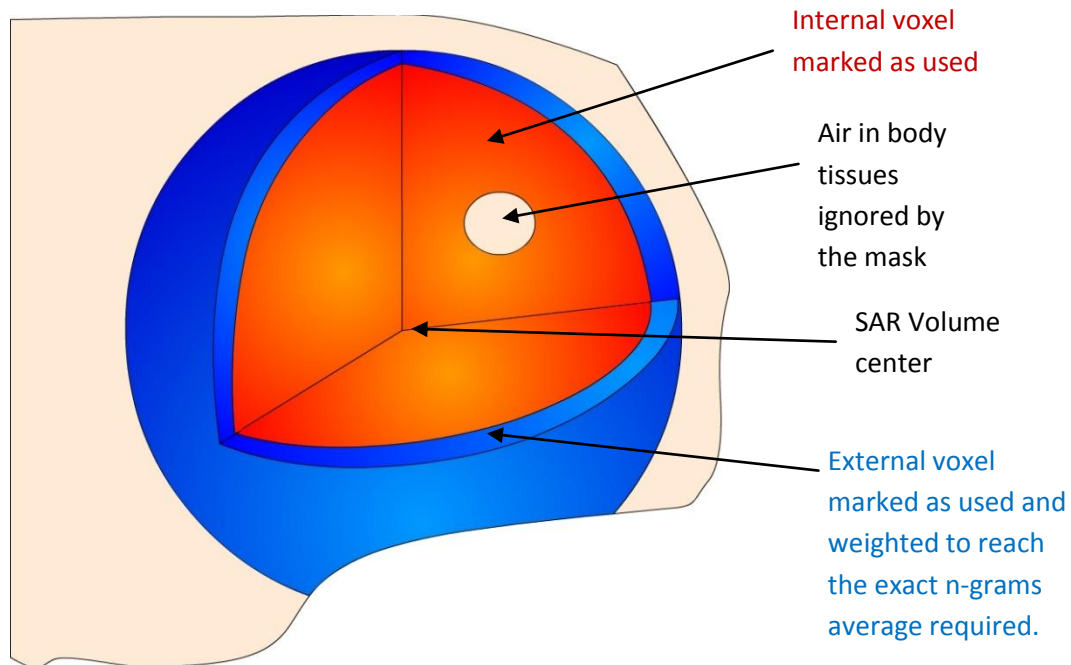


Figure 5.3: 3-D section of the spherical averaging mask applied on the border of a body tissue. The red voxels are used in the averaging method, while the external voxels in blue will be weighted if necessary, as explained in eq. (5.2), to reach the required n-grams averaging mass.

It is possible to appreciate the smoothness of the averaging process of the proposed method when applied to the geometry of Fig. 5.4 where the discontinuities have been reduced and, as expected, a larger and more conservative value of average SAR is obtained at the borders of the sample, close to the peaks of the unaveraged SAR distribution. This is clearly shown in Figure (5.5).

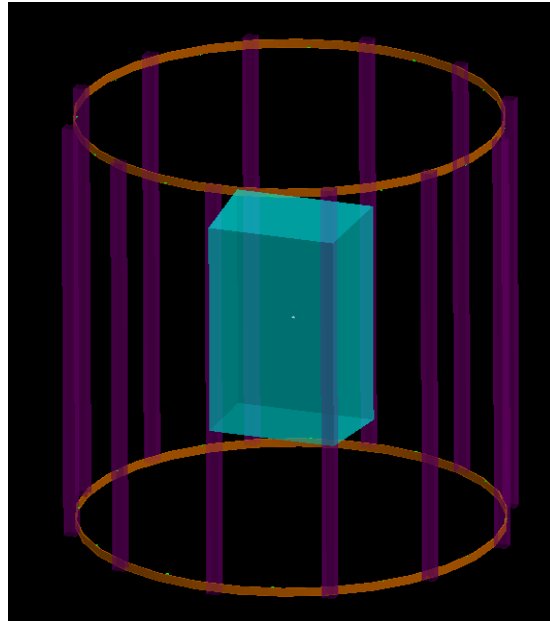


Figure 5.4: Geometry of the model used in simulations: a 16-element birdcage coil loaded with a cubical water sample positioned near the center of the volume coil.

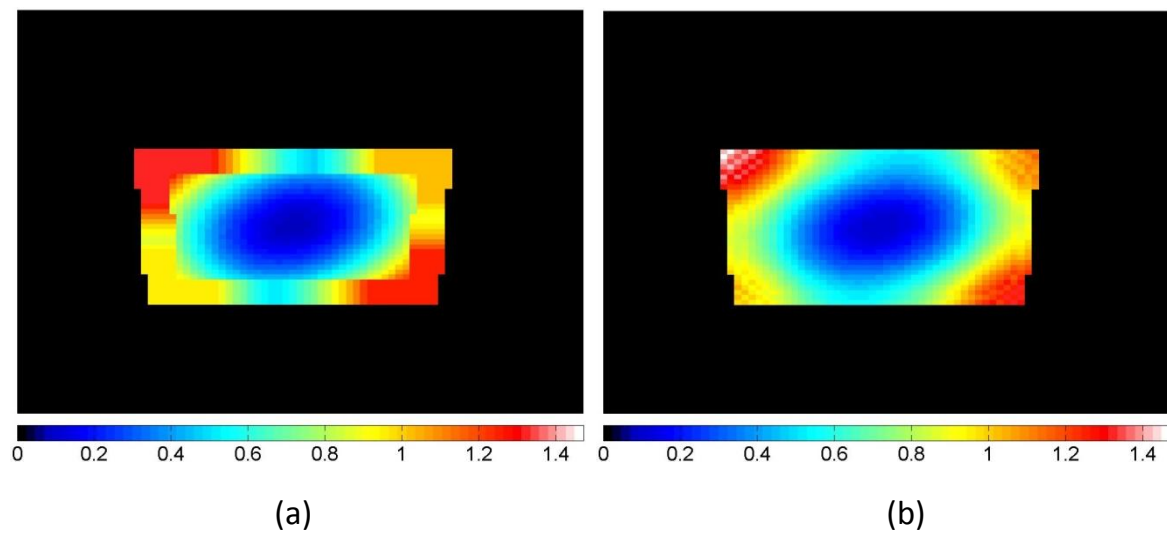


Figure 5.5: For a cube of water plots of (a) the 10 g averaged SAR distribution computed by commercial software, (b) the 10 g averaged SAR distribution computed with the algorithm proposed in this Chapter based on spherical masks.

The method has been implemented as a tool for the PSUdo MRI simulator of the CNMRR Research group of Penn State at Hershey[91]. A Graphic Interface with MATLAB (The Mathworks, MA, USA) has been developed for the simulator, able to load SAR files either from:

1. SAR data from the PSUdo MRI simulator.
2. XFDTD unaveraged SAR files.
3. XFDTD electric field files along with the XFDTD geometry files containing both the conductivity and density distribution data.

The tool has the capability of parallel computation in presence of a multi-core CPU, making averaging computation faster. An illustration of the GUI is in Fig. 5.6.

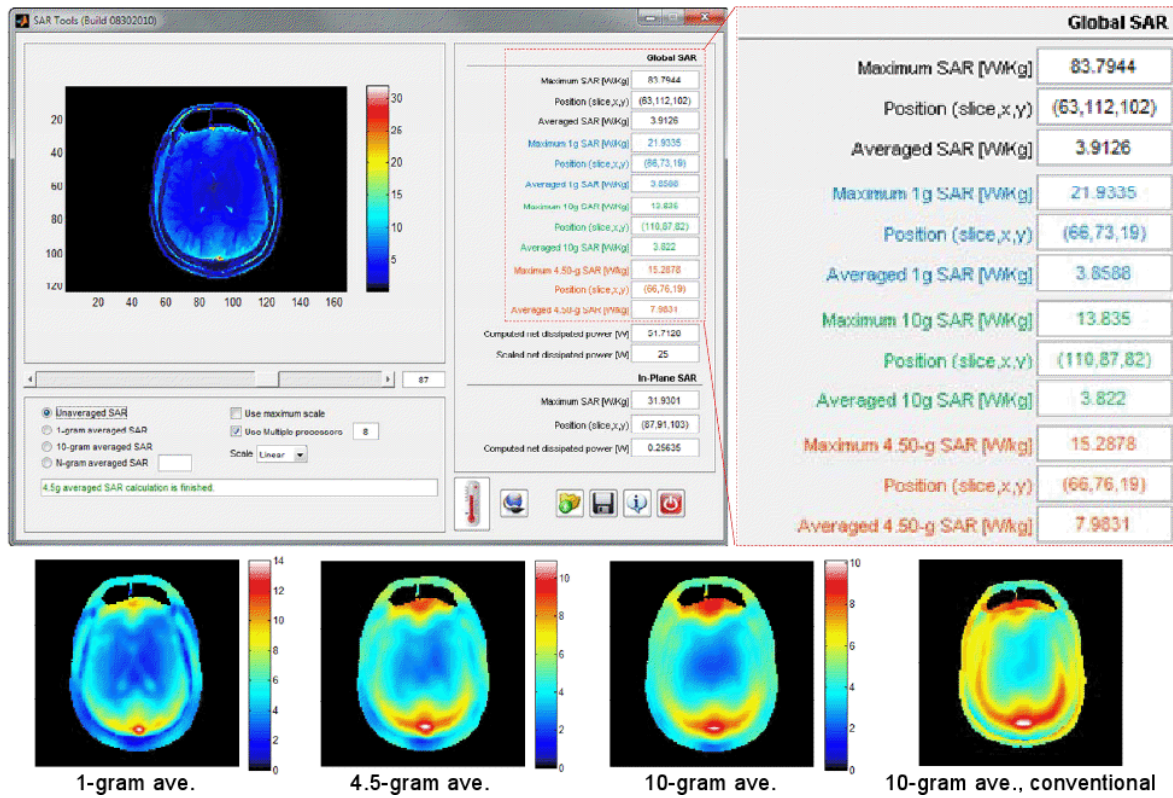


Figure 5.6: GUI of the SAR calculation tool with unaveraged SAR displayed and (right) detail of the displayed SAR data. Bottom: SAR distributions from the proposed method for 1g, 4.5g, and 10g averaged SAR as well as 10g average SAR calculated with the conventional cubical method.

CHAPTER 6

A FAST ALGORITHM TO COMPUTE TEMPERATURE INCREASE DUE TO SAR ABSORPTION

6.1 Introduction

In Chapter 5 we presented a new method to compute with higher accuracy the local average SAR. Currently, 10g local average SAR is the quantity used most often to assess safety of MRI sequences and coils with respect to local heating, although it is cumbersome and time-consuming to calculate and by itself is a quantity with limited direct relation to risk. While temperature increase has a much more intuitive and direct relationship to risk it is typically not calculated at all due to the associated complexity and time requirements, even though in transmit arrays applications where the field distributions can change, it would be valuable to quickly predict the temperature change. In this Chapter we present a method for estimating SAR-induced temperature increase, based on the sequential application of a digital filter, that is many times faster than existing methods for calculating either temperature increase or local average SAR. We set the parameters of the filter and validate the results with a more rigorous Finite Difference method for temperature estimation.

6.2 SAR and temperature estimation

The main reason to include SAR averaging processes in the safety limits is linked to the relationship between the SAR and the temperature increase in body tissues. SAR absorption is cause of temperature increase, and the resulting temperature distribution is similar to a smoothed SAR distribution due to the heat conductivity of the materials. For example, if some power is absorbed in a specific location, the temperature distribution will have its peak on that location, but

it will spatially increase smoothly around. The averaging process is one basic way to partially describe this spatial smoothing, because the spatial average operation bevels the original heat source distribution. Hence, for long exposure-time 10-grams averaged SAR is correlated to temperature increase distribution due to SAR deposition [59]. One widely used relation able to describe with higher accuracy the heat conductivity effect and also able to take into account the contribution of the blood perfusion rate is the Pennes' bioheat equation [95]

$$\rho c \frac{\partial T}{\partial t} = \nabla \cdot (k \nabla T) - W \rho_{bl} c_{bl} (T - T_{bl}) + Q + \rho SAR \quad (6.1)$$

where c is the heat capacity, W the blood perfusion rate, k the thermal conductivity, ρ material density, the subscript $_{bl}$ indicates values for blood, and Q the heat generated by metabolism.

There are some existing FD methods able to compute eq. (6.1) with accurate estimations of temperature increase, but requiring long computation time. The first term on the right-hand side ($\nabla \cdot (k \nabla T)$), related to thermal conduction, is the main responsible for the high complexity and time consuming of the temperature calculations. In applications such as transmit arrays in MRI systems, where the field distributions can change while the patient is in the magnet, there is need for methods of meaningful real-time safety assessment. Hence, fast algorithms to predict temperature increase depending on SAR distribution are desired.

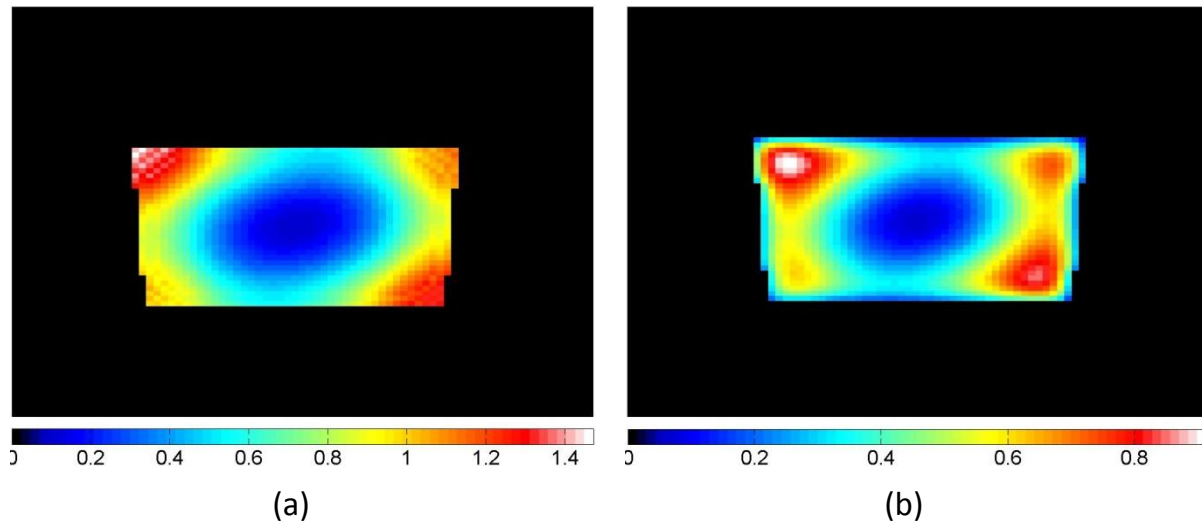


Figure 6.1: For a cube of water plots of (a) the 10 g averaged SAR distribution, (b) temperature increase calculated with an FD method (5 minutes heating time).

6.3 The low-pass filter

Starting from the idea of the correlation between SAR average and temperature, we propose a method to improve the accuracy between a smoothed SAR and temperature increase introducing the idea of the application of a low-pass filter to the SAR distribution: spatial average can be considered, in fact, as a special kind of low-pass filter that saves only the continuous component in a localized volume. However, a more specific low-pass filter may be able to provide a better accuracy in estimating the temperature increase. We based the design of the filter on the analysis of the structure of eq. (6.1) and on the results provided by a Finite Difference (FD) code able to solve eq. (6.1).

Material Tissue	$W, \text{ml} \cdot 100 \text{g}^{-1} \cdot \text{min}^{-1}$	$\rho, \text{kg/m}^3$	$c, \text{J} \cdot \text{kg}^{-1} \cdot ^\circ\text{C}^{-1}$	$k, \text{W} \cdot \text{m}^{-1} \cdot ^\circ\text{C}^{-1}$	$Q_m, \text{W/m}^3$
Air	0	1.3	1006	0.026	0
Blood	1000	1057	3600	0.51	0
Cancellous bone	3	1080	2110	0.65	26.1
Cerebellum	45.2	1035.5	3640	0.534	11600
Cerebrospinal fluid	0	1007	3800	0.50	0
Cortical bone	1.35	1850	1300	0.65	26.1
Esophagus	40	1.126	3720	0.527	697
Eye: sclera/cornea	0	1076	3000	0.40	0
Eye: vitreous humor	0	1009	4200	0.594	0
Fat	2.8	916	2300	0.25	302
Gray matter	67.1	1035.5	3680	0.565	15575
Tendon	3.8	1151	3500	0.4975	0
Muscle	3.8	1041	3720	0.4975	697
Skin	12	1100	3150	0.342	1100
White matter	23.7	1027.4	3600	0.503	5192

Table 6.1: Material properties of the body tissues: w (perfusion blood), ρ (material density), c (heat capacity), k , heat conductivity, Q (heat of metabolism).

The spatial smoothness of induced temperature is affected by the heat conductivity values of body tissues. Higher heat conductivity values correspond to smoother spatial temperature change (Fig. 6.2). Thus, for each single tissue there is a specific filter able to describe heat conductivity effect. However, the low variance between the heat conductivity values in body tissues allows to reach high accuracy by using only a single low-pass filter. Values of the heat conductivity for each specific body tissue can be found in Table 6.1 [37].

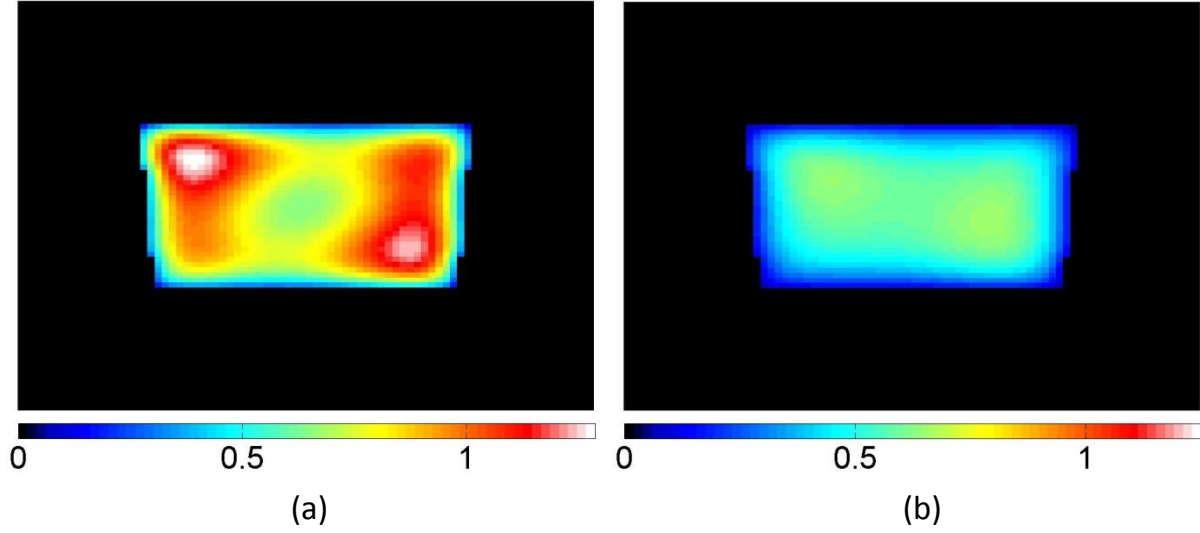


Figure 6.2: for a phantom cube, temperature increase distributions for a phantom having heat conductivity $k=0.6$ (a), and one with $k=2$ (b). Both temperature distributions have been computed with an FD solver for a 15 minutes heating time.

6.4 The low-pass filter applied to a simple geometry

A first filter for a simple geometry was designed for the cube of water used previously to test the new method to compute average SAR in Chapter 5. For this sample the eq. (6.1) reduces to

$$\rho c \frac{\partial T}{\partial t} = k \nabla^2 T + \rho SAR \quad (6.2)$$

because the sample has neither blood perfusion rate nor heat generated by metabolism. Given the second derivative dependence for the spatial variables in eq. (6.2), a second order filter was chosen. In addition to the two cutoff frequencies, the exponents of the poles of the filter were added as optimizing parameters. In the frequency domain the equation of the filter is

$$F(\lambda_x, \lambda_y, \lambda_z) = \frac{1}{\left(1 + \frac{i\lambda_x}{p_{x1}}\right)^{\alpha_{x1}} \left(1 + \frac{i\lambda_x}{p_{x2}}\right)^{\alpha_{x2}} \left(1 + \frac{i\lambda_y}{p_{y1}}\right)^{\alpha_{y1}} \left(1 + \frac{i\lambda_y}{p_{y2}}\right)^{\alpha_{y2}} \left(1 + \frac{i\lambda_z}{p_{z1}}\right)^{\alpha_{z1}} \left(1 + \frac{i\lambda_z}{p_{z2}}\right)^{\alpha_{z2}}} \quad (6.3)$$

where $\lambda_x, \lambda_y, \lambda_z$ are respectively the spatial variables in the Fourier domain of the x, y, z direction; p_{x1}, p_{y1}, p_{z1} are respectively the first cutoff frequencies for the spatial variables $\lambda_x, \lambda_y, \lambda_z$, and p_{x2}, p_{y2}, p_{z2} the second cutoff frequencies in the Fourier directions. In addition $\alpha_{x1}, \alpha_{y1}, \alpha_{z1}$ are the orders of the first cutoff frequencies, and $\alpha_{x2}, \alpha_{y2}, \alpha_{z2}$ the orders of the second cutoff frequencies.

The parameters of the filter ($p_{x1}, p_{x2}, p_{y1}, p_{y2}, p_{z1}, p_{z2}$ and the orders $\alpha_{x1}, \alpha_{x2}, \alpha_{y1}, \alpha_{y2}, \alpha_{z1}, \alpha_{z2}$) have been determined by minimizing the norm of the difference between the temperature predicted by our algorithm and the temperature predicted by the FD code (less than 15 %). A different heating time exposure requires a different set of parameters.

The filter can be adapted to different meshgrid sizes and different sizes of the matrix containing the SAR distribution. In fact, in case of a different meshgrid of the sample, using the properties of the FFT transform, the cutoff frequencies in eq. (6.3) are scaled to fit with the matrix size of the sample, because the position of the cutoff frequency is proportional to the size of the matrix and to the meshgrid dimensions. Thus, indicating with $M_{m \times n \times p}$ the matrix containing the information of the sample, and a, b, c the dimensions of the grid in the x, y, z directions the parameters of the filter in eq. (6.3) are

$$\begin{aligned}
p_{x1} &= p_{x1s} \frac{m}{m_s} \frac{a}{a_s} \\
p_{x2} &= p_{x2s} \frac{m}{m_s} \frac{a}{a_s} \\
p_{y1} &= p_{y1s} \frac{n}{n_s} \frac{b}{b_s} \\
p_{y2} &= p_{y2s} \frac{n}{n_s} \frac{b}{b_s} \\
p_{z1} &= p_{z1s} \frac{p}{p_s} \frac{c}{c_s} \\
p_{z2} &= p_{z2s} \frac{m}{p_s} \frac{c}{c_s}
\end{aligned} \tag{6.4}$$

where $p_{x1s}, p_{x2s}, p_{y1s}, p_{y2s}, p_{z1s}, p_{z2s}$ are the computed optimum cutoff frequencies for a sample matrix $M_{sm_s \times n_s \times p_s}$ with a meshgrid resolution $a_s \times b_s \times c_s$.

The temperature calculations were based on the SAR distributions obtained through electromagnetic simulations, shown in the previous Chapter.

The performance of the algorithm was compared with two algorithms: the FD method and the 10 g averaged SAR. Comparisons included examinations of both the temperature increase distribution and the necessary computation time. Since 10 g averaged SAR does not compute temperature values, the averaged SAR is scaled so that the norm of the difference with the temperatures predicted by the FD code is minimized

Parameters	$t_{int} = 30 \text{ s}$	$t_{int} = 60 \text{ s}$	$t_{int} = 120 \text{ s}$
$p_{x1s}, p_{y1s}, p_{z1s}$	32.40	13.85	6.24
$p_{x2s}, p_{y2s}, p_{z2s}$	40.56	28.12	21.49
$\alpha_{x1}, \alpha_{y1}, \alpha_{z1}$	0.96	0.2	0.22
$\alpha_{x2}, \alpha_{y2}, \alpha_{z2}$	0.29	1.03	0.96

Table 6.2: Values of the optimum parameters of the filter for a two minutes heating time, for a sample matrix $\mathbf{M}_{s_{250x250x250}}$ with a meshgrid resolution of $2 \times 2 \times 2 \text{ mm}^3$.

The first results are shown in Fig. 6.3 and show strong accuracy between the temperature predicted by the FD code and the one obtained applying the low-pass filter, not only in terms of spatial distribution, but also quantitative measure of the temperature increase. In fact, a weak point of the SAR average method to partially estimate temperature is that it does not provide a quantitative measure of the temperature (average SAR is measured in W/kg while temperature is in $^{\circ}\text{C}$), but only some correlation. On the contrary, with the generic low-pass filter approach it is possible to estimate specifically temperature values.

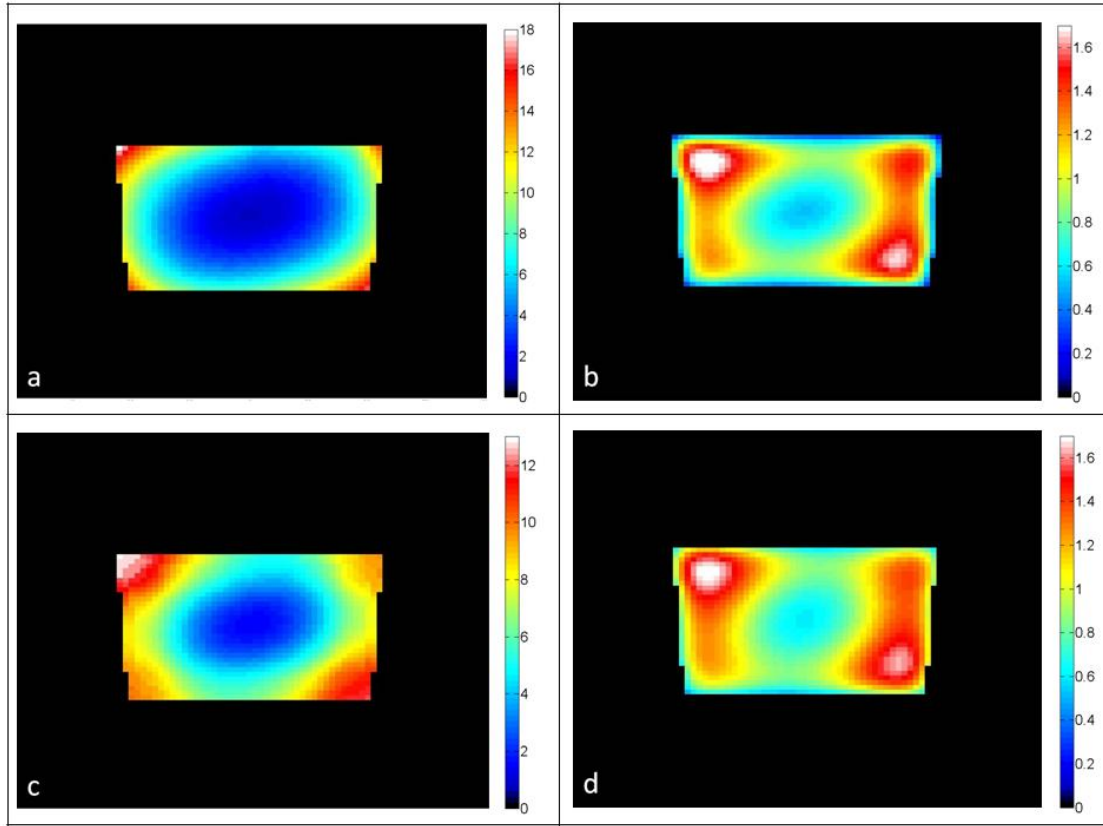


Figure 6.3: For a cube of water plots of (a) the unaveraged SAR distribution, (b) temperature increase calculated with a rigorous finite difference algorithm (15 minutes heating time), (c) 10 g average SAR distribution, (d) temperature increase calculated with the proposed rapid digital filter algorithm (15 minutes heating time).

The algorithm can be simply described as follows:

Step 1: Calculate FFT of the SAR distribution: $F_{SAR} = FFT(SAR)$.

Step 2: Apply the filter in eq. (6.3) to the distribution F_{SAR} , obtaining the matrix LPF_{SAR}

Step 3: Compute the Inverse FFT of the matrix LPF_{SAR} : $T = FFT^{-1}(LPF_{SAR})$.

The result of the Step 3, T , is the temperature increase distribution.

Thus, this method is extremely fast because it requires only the time to calculate the 3-D FFT and the Inverse FFT, leading to a total computation time more than 60 times faster than the FDTD method and more than 20 times faster than SAR averaging.

Then, a deeper analysis of the properties of the designed filter has been achieved to correlate the parameters of the filter with the properties of the sample. First, the SAR distribution was changed keeping the same filter with the parameters optimized for only one SAR distribution. The scheme of the test is shown in Fig. (6.4) where, starting from a given SAR distribution and applying the FD method, a transfer function was found to be applied directly to other SAR distributions without running again FD methods.

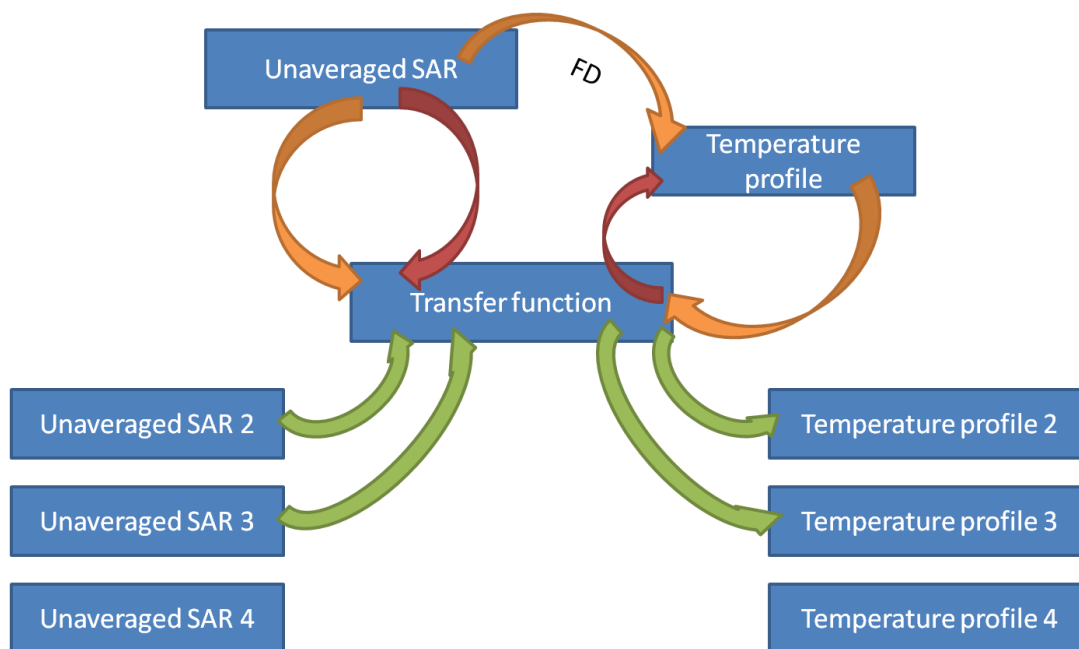


Figure 6.4: Scheme of the determination of the transfer function to estimate Temperature profile from unaveraged SAR. Running only once the FD code allows obtaining a temperature profile. From the unaveraged SAR and the computed FD profile, it is possible to calculate the transfer function of the filter. Then, the obtained transfer function is used to estimate temperature profiles from several SAR profiles without to run again the FD code.

The test was successful because, while changing the value of the SAR distributions, we still kept an error lower than 15 %. This result is very significant because, since the SAR distribution is not correlated with the parameters of the filter, the method explained in Fig. 6.4 can be used in optimization routines of transmit arrays due to its high speed, because it is necessary only a repeated application of the same filter with different SAR distributions as input. Four different SAR distributions and the corresponding temperature estimated with the FD code and the low-pass filter are shown in Fig. 6.5.

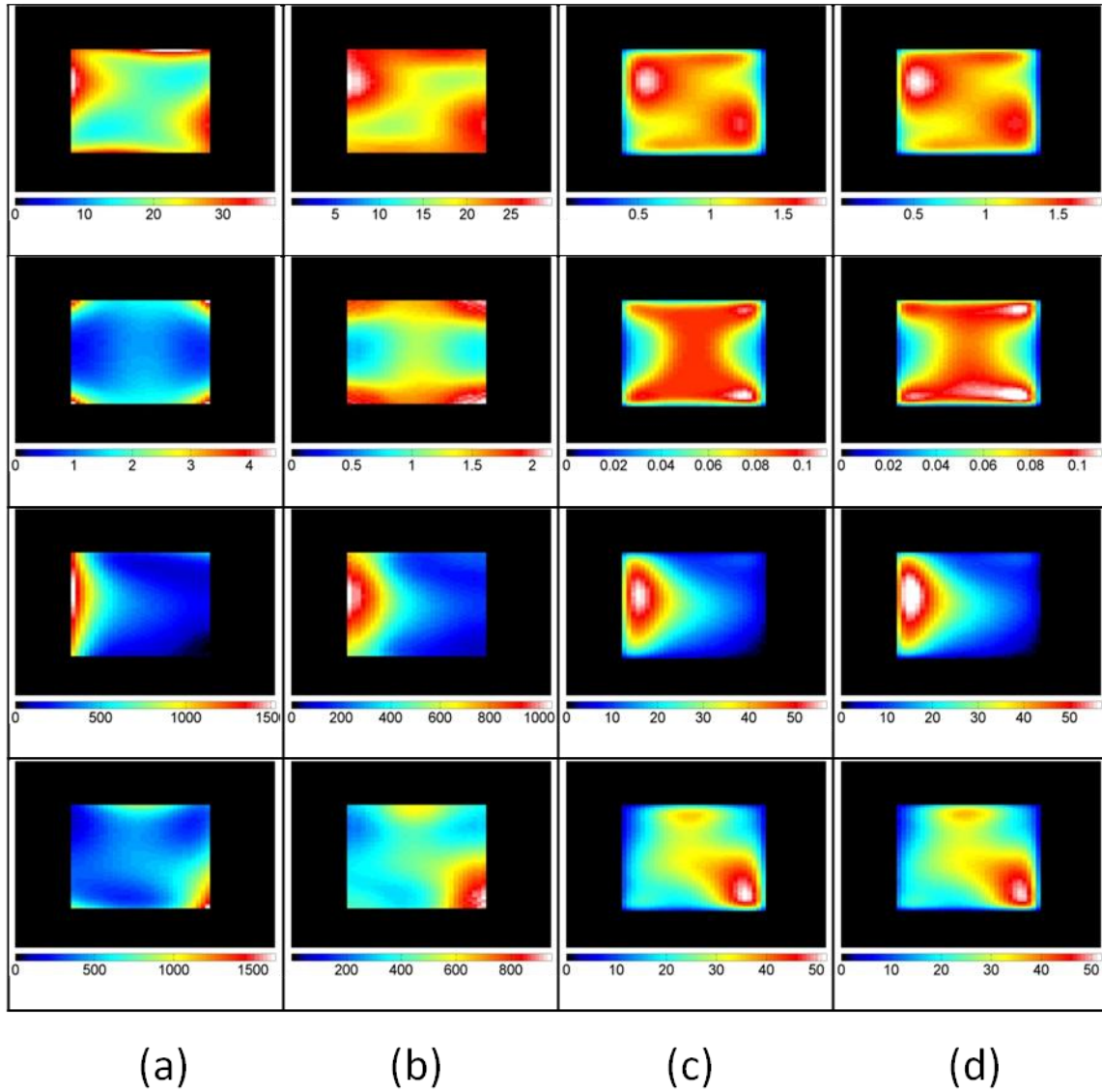


Figure 6.5: for a cube of water, starting from four unaveraged SAR distributions (a), the corresponding 10 g average SAR distributions (b), the temperature increase calculated with a rigorous finite difference algorithm (15 minutes heating time) (c), temperature increase calculated with the proposed rapid digital filter algorithm (15 minutes heating time) (d).

After testing the relation between SAR and filter, the same filter has been applied to different geometries of phantoms containing water, to find the connection between the parameters of the filter and the geometry of the sample. Also in this case, it was found low error between the

temperatures estimated with the FD code and the ones obtained applying the same filter to different shapes, as shown in Fig. 6.6. This seems to indicate that the parameters of the filter are independent of the shape of the sample.

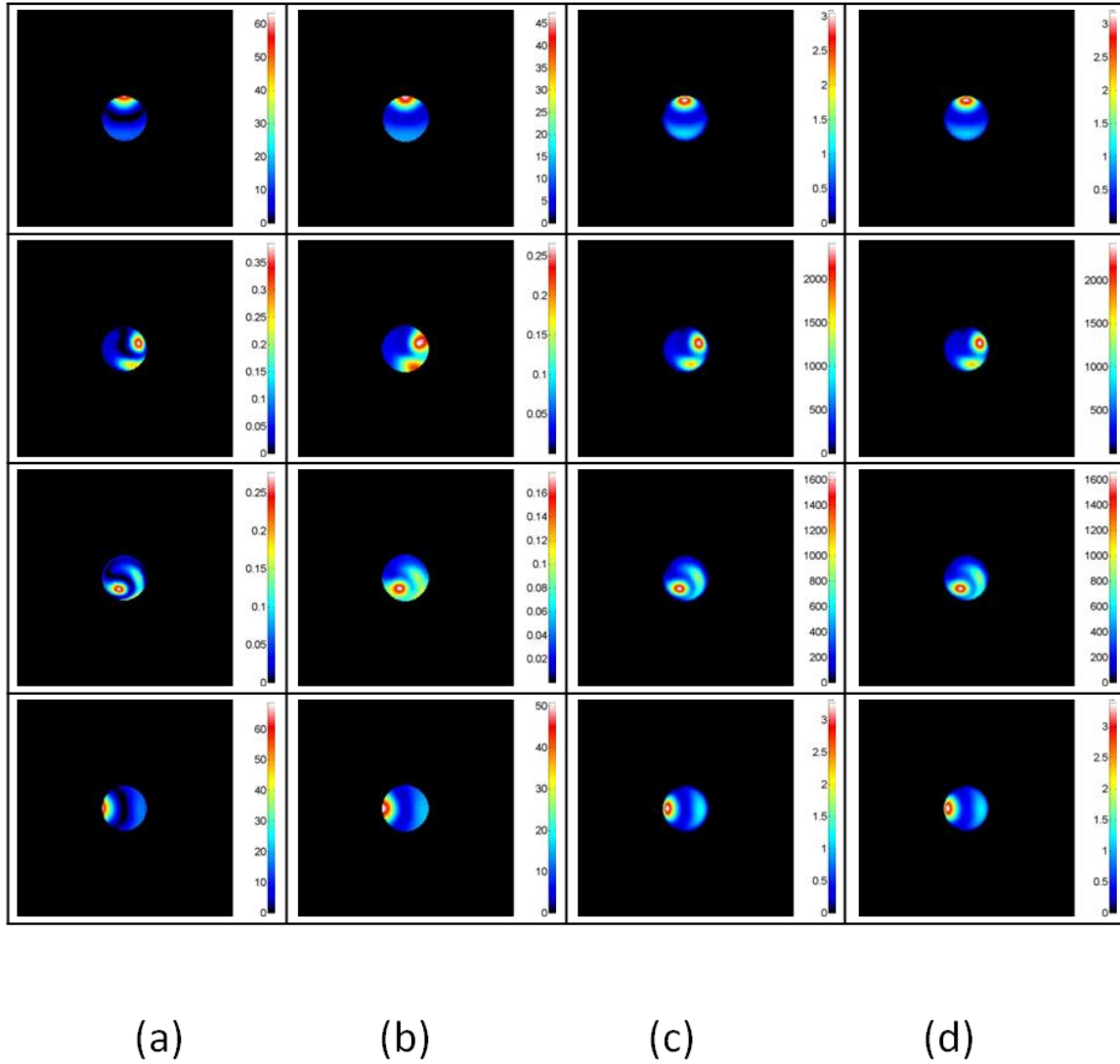


Figure 6.6: for a sphere of water, starting from four unaveraged SAR distributions (a), the corresponding 10 g average SAR distributions (b), the temperature increase calculated with a rigorous finite difference algorithm (15 minutes heating time) (c), temperature increase calculated with the proposed rapid digital filter algorithm (15 minutes heating time) (d).

Then, the relation between the heat conductivity of the sample and the parameters of the filter was tested. On the contrary, in this case applying the same filter to phantoms having materials with different heat conductivities it was not possible to find the same temperature values, as in Fig. 6.2. Discrepancy is also found when applying the same filter to different heating times, as shown in Fig. 6.7.

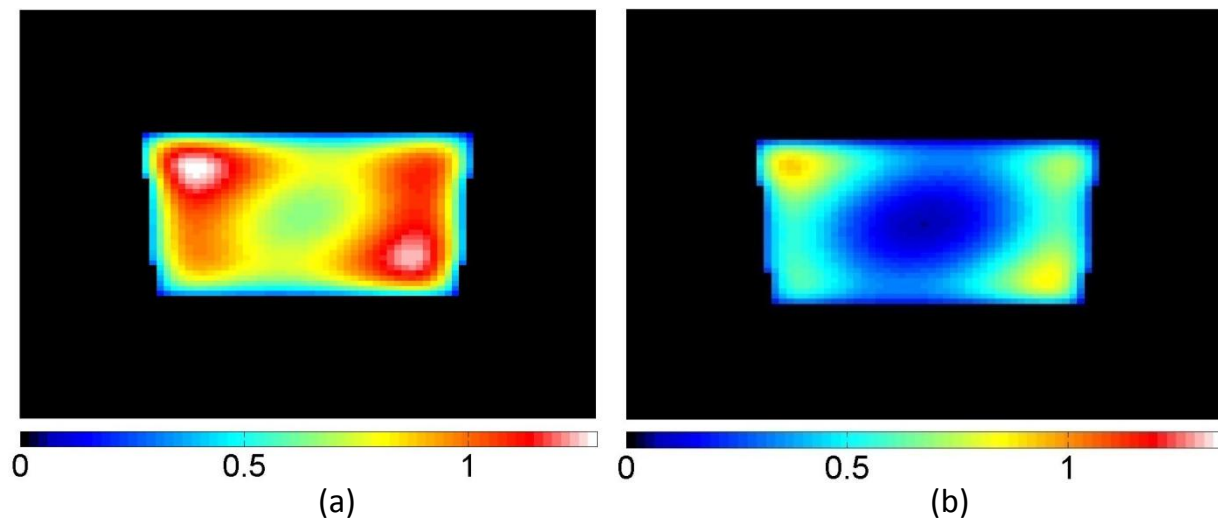


Figure 6.7: for a cube of water, plots of temperature distributions with 15 minutes heating time (a), and with 5 minutes heating time (b). The strong difference between them does not allow to find one single filter for both.

Summarizing, the same filter can be used in case of different

- SAR distribution;
- shape of the sample.

The parameters of the filter needs to be changed in case of different

- heat conductivity of the material;
- heating time.

6.5 The low-pass filter applied to more complex geometries

After the application of the filter for a simple geometry, the efficiency of the filter has been evaluated when applied to more complex geometries such as the human head. In case of human tissues, each geometry has several materials with different heat conductivities and, compared to the previously examined cube of water, also different perfusion blood rates and heat generated by metabolism for each material.

It can be noticed that eq. (6.1) can be simplified in

$$\rho c \frac{\partial T}{\partial t} = \nabla \cdot (k \nabla T) - W \rho_{bl} c_{bl} T + \rho SAR \quad (6.5)$$

where the terms Q , T_{bl} have been excluded because they determine the steady state value of the temperature T_{st} in absence of SAR absorption. Due to the linearity of eq. (6.1), the total temperature is then given by

$$T = T_{st} + T_i \quad (6.6)$$

Supposing that the heat generated by metabolism is steady also during SAR absorption, with eq. (6.6) it can be excluded from the computation of the temperature increase, because metabolism only contributes to the steady state value of the temperature.

Applying the low-pass filter, as in the previous section, to the SAR distribution obtained with a quadrature surface coil about the occipital lobe, the computed temperature increase is very different from the one that is computed with an FD code (Fig. 6.8).

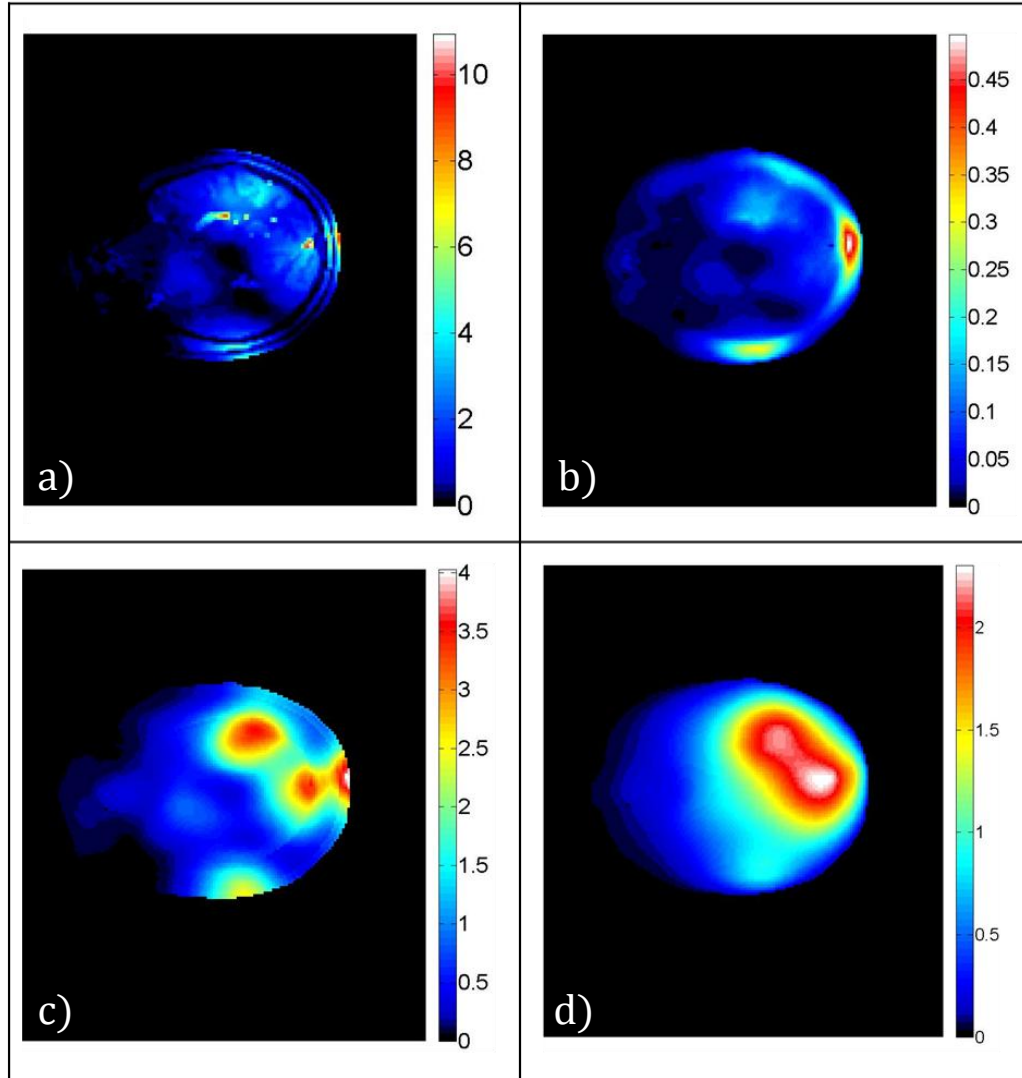


Figure 6.8: For a quadrature surface about the occipital lobe, plots of (a) the unaveraged SAR distribution, (b) temperature increase calculated with a rigorous finite difference algorithm (1 hour heating time), (c) 10 g average SAR distribution, (d) temperature increase calculated with the filtered SAR without considering the contribution of the blood perfusion rate (1 hour heating time).

Even though the effect of the low-pass filter is to emulate in eq. (6.5) the contribution of the heat conductivity (the term $\nabla \cdot (k \nabla T)$), the contribution of the blood perfusion rate (the term $-W\rho_{bl}c_{bl}T$) to the final temperature increase has not been included yet in the filter algorithm. In

addition, especially in tissues such as the white and the grey matter, blood perfusion rate is a relevant contribution, as reported in Table (6.1).

Our solution to the problem is to apply the low-pass filter not to the SAR distribution (as it was done in SAR averaging processes), but to the solution of the differential eq. (6.7) where the contribution of the heat conductivity in eq. (6.5) has been neglected.

$$\rho c \frac{\partial T_i}{\partial t} = -W \rho_{bl} c_{bl} T_i + \rho SAR \quad (6.7)$$

In this way it is first considered the contribution of the perfusion blood rate, and later the neglected heat conductivity applying the low pass filter. It should be noticed that this solution is also consistent with the simpler cases examined before. In fact, in case W were null, eq. (6.7) becomes

$$\rho c \frac{\partial T}{\partial t} = \rho SAR, \quad (6.8)$$

whose solution is

$$\Delta T = \frac{1}{c} SAR \Delta t, \quad (6.9)$$

that shows a linear proportionality between temperature increase and SAR. Thus, the application of a low-pass filter to the temperature in eq. (6.9) is exactly equivalent (except for a proportionality constant) to the application of a low-pass filter to the SAR distribution.

Given a heating time t_{int} , the solution of eq. (6.7) is equal to

$$T_i(t_{int}) = \frac{SAR \rho}{WC_{bl}R_{bl}} \left(1 - e^{-\frac{WC_{bl}R_{bl}}{\rho} t_{int}} \right) + T_{initial} e^{-\frac{WC_{bl}R_{bl}}{\rho} t_{int}} \quad (6.10)$$

where $T_{initial}$ is the initial temperature. The possibility to find a solution starting from an initial temperature is an important feature of this approach, because it allows to overcome one of the two limits that was pointed out in the previous section: the necessity of designing a filter for each different heating time. In fact, if the final solution of the temperature increase computation (i.e. after applying the low-pass filter) can be considered the initial temperature for a new temperature increase process, a long heating time exposure can be considered as the sequential application of shorter heating time temperature increase computation of length t_{int} . Hence, in a sequential

algorithm in multiple stages or intervals n such that $T_{n+1} = T_n + T_i$ it is possible to rewrite eq. (6.10) so that the initial temperature $T_{initial}$ is T_n , and the temperature $T_i(t_{int})$ the temperature T_{n+1} .

$$T_{n+1}(t_{int}) = \frac{SAR \rho}{WC_{bl}R_{bl}} \left(1 - e^{-\frac{WC_{bl}R_{bl}}{C\rho} t_{int}} \right) + T_n e^{-\frac{WC_{bl}R_{bl}}{C\rho} t_{int}} \quad (6.11)$$

In other words, the complete algorithm can be described as follows:

- Step 1: compute the temperature increase in a given time interval solving Pennes' bioheat equation (6.5) neglecting heat conductivity: eq. (6.7). The solution T_{n+1} is simply given by eq. (6.11) where t_{int} is the time duration of the short time intervals where the filter is applied.
- Step 2: compute FFT of the temperature distribution T_{n+1} of Step 1: $F_{T_n} = FFT(T_n)$.
- Step 3: apply the filter in eq. (6.3) to the distribution F_{T_n} , obtaining the matrix LF_{T_n} .
- Step 4: compute inverse FFT of the matrix LF_{T_n} : $T_{n+1} = FFT^{-1}(LF_{T_n})$.
- Step 5: go to Step 1 using T_{n+1} in Step 4 as initial temperature T_n .

This process has to be repeated $N = \frac{T_t}{t_{int}}$ times, where T_t is the total heating time. The final temperature distribution will be the matrix T_N in Step 4 from the last executed cycle of the algorithm.

This structure of the method is not too far from numerical FD methods: the main difference between the two algorithms is that a low-pass filter works on the whole data matrix and not voxel by voxel like FD methods do, reducing drastically the computation time.

The other difference is that using only a low-pass filter some accuracy is lost due to the different heat conductivity values in different body tissues. However, looking at the values of k for the materials in our body (Table 6.1), we can see that they are very close: hence, even though several materials are present in the inspected geometry, this should not affect drastically the

accuracy of the result. The other source of inaccuracy can be found at the boundaries: the air is analyzed as a tissue having null SAR, density, heat capacity and blood perfusion rate. Since the filter operates in the Fourier domain, due to the continuity of the Inverse Fourier Transform, the smoothing effect leads to some small temperature changes in the air too.

With this sequential algorithm, it is possible to estimate temperature increase even for complex geometries.

Fig. (6.9) shows the unaveraged SAR distribution and the corresponding temperature distribution for the three different algorithms: it shows strong similarities between the FD method and our algorithm. On the contrary, the 10 g mass-averaged SAR, even if it is scaled to have similar values to the other two temperature distributions, shows a distribution not similar. The main reason is due to its inability to consider the contribution of the blood perfusion rate, that especially in tissues such the gray matter is very significant.

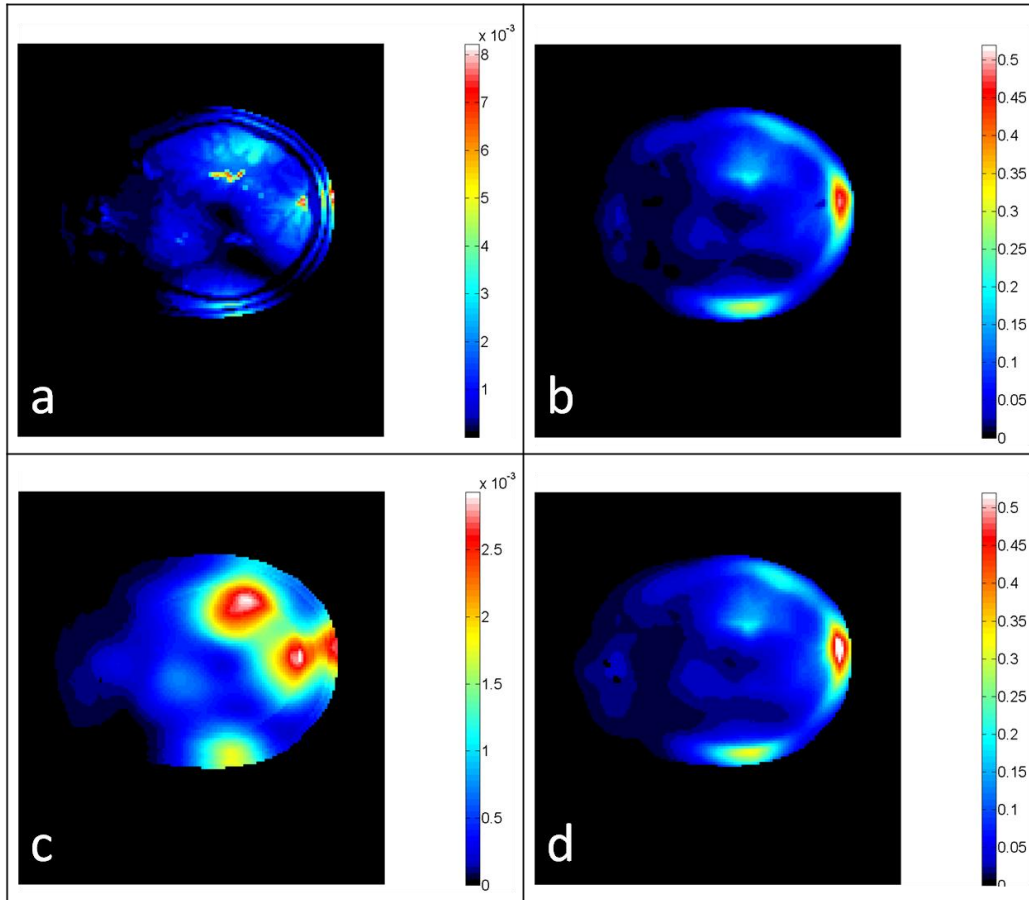


Figure 6.9: For a quadrature surface about the occipital lobe, plots of (a) the unaveraged SAR distribution, (b) temperature increase calculated with a rigorous finite difference algorithm (1 hour heating time), (c) 10 g average SAR distribution, (d) temperature increase calculated with the filtered SAR considering the contribution of the blood perfusion rate (1 hour heating time).

For the case shown in Fig. 6.9, the required computation time for the FDTD method with a 4 GB RAM pentium IV PC was 75 minutes, for the average SAR method it was 18 minutes, and only 2 minutes for the digital filter. Thus, with the filter in a much shorter amount of time we can get a result very similar to the one obtained with the more time consuming FDTD method.

6.6 Conclusions

This thesis was intended to improve the B_1 field distribution in a localized region of interest, and to propose a faster algorithm and a deeper understanding of temperature increase in body tissues due to SAR absorption from electromagnetic exposure in MRI experiments.

The necessity to focus on a region of interest smaller than the total cross-section comes from the current trend in MRI towards higher B_0 fields and consequently higher B_1 field frequencies. The shorter wavelength of the B_1 fields affects the quality of the final images, and transmit arrays RF shimming techniques are nowadays widely used to model the B_1 field distribution to compensate the stationary waves due to wave reflections across the interfaces between different materials. However, since it is not always possible to achieve high uniformity of the flip-angle while keeping low SAR levels, which is necessary in order to not overheat the patient, we focused on a reduced volume of interest with a diameter comparable with half-wavelength in the medium, trying to obtain strong uniform fields and more easily control the power deposition. An analytical method to optimize both the amplitudes and phases of the currents of the elements of the transmit array has been presented in this thesis. The method has been developed with the help of two 2-D analytical solutions presented in Chapter 3, where a circular and an elliptical base infinitely long cylinder, representing the brain, was surrounded by a shell, representing the skull: both the objects were located in the xy plane. The excitation field was produced by a system of M wires parallel to the z axis and located around the cylinder representing the legs of a birdcage coil. From the analysis of the field distributions, when compared with more exact numerical simulations involving the use of a hi-fi head model, we concluded that the 2-D analytical solutions can help to estimate the number and the location of the spots of magnetic field B_1 concentration for a given current scheme in a very short time. Due to their short computation time and their accuracy to predict the location of the field peaks, they were used in the development process of the analytical optimization method presented in Chapter 4: given the magnetic field distribution generated by each element of the

transmit array, and the impedance matrix of the transmit array, the method provides a simple formula to achieve the best set of magnitudes and phases for the currents of the array to maximize the magnetic field B_1 in the volume of interest, and to minimize the generated power. In our simulations, for a transmit array operating at 300 MHz, when compared with the fields obtained by a classical birdcage coil, our method produced a B_1 field in magnitude more than 2 times larger generating the same amount of power, and when compared to an algorithm that optimizes only the phases of the elements of the array, it provided a small improvement for internal tissues (about 10 % improvement), and a large improvement for external ones (about 100 %). It is relevant to notice that the optimization method is not affected by the operating frequency range and by the geometry of the elements of the RF transmit array, thus yielding also with future developments of the hardware responsible of the B_0 field and with new designs of RF coils for the B_1 field.

The optimization method tried to minimize the generated power to make easier to satisfy safety limits imposed to MRI systems by IEC. Due to their relevance in RF coils design, safety regulations problems have been also explored in this dissertation: specifically in Chapter 5 has been presented a method able to compute average SAR with adaptive spherical masks. The spherical masks guarantee the minimum distance from the used voxels and the centered one, providing higher accuracy in estimating the effect of SAR absorption in a localized region respect to the classic algorithms that use cubical shaped masks. The geometry adaptive property helps to overcome problems linked to the definition of the masks in regions close to air boundaries, commonly resulting in discontinuities of the fields around those areas. The presented results show a higher continuity of the average SAR profiles respect to classic algorithms implemented in commercial numerical electromagnetic simulators for biological applications. In addition, a digital filter has been presented in Chapter 6 able to compute temperature increase in body tissues by SAR absorption. The obtained results are very promising because the algorithm can provide with a reasonable error (less than 15 %) results very similar to more accurate FD methods in a time more

than 60 times shorter. Several results have been presented in the dissertation, involving simple and complex geometries such as the human head where blood perfusion rates in tissues such as white and grey brain matter are significant. This fast algorithm opens new scenarios and future works such as real-time optimization algorithms of transmit arrays in MRI systems, where the field distributions can change while the patient is in the magnet, routines impossible to run in a reasonable short time with classic FD methods.

REFERENCES

- [1] Abragam A., "Principles of Nuclear Magnetism", *Oxford University Press*, 1961.
- [2] Abraham R., Ibrahim T., "Proposed radiofrequency phased-array excitation scheme for homogeneous and localized 7-T whole-body imaging based on full-wave numerical simulations", *Magnetic Resonance in Medicine*, vol. 57, pp. 235-242, 2007.
- [3] Abramowitz M., Stegun L.A., "Handbook of Mathematical Functions", 1965
- [4] Adair E. R., Berglund L. G., "On the thermoregulatory consequences of NMR imaging", *Magnetic Resonance Imaging*, vol. 4, pp. 321-333, 1986.
- [5] Balanis C., "Advanced Engineering Electromagnetics", *John Wiley & Sons*, 1989.
- [6] Balasubramaniam T. A., Bowman H. F., "Thermal Conductivity and Thermal Diffusivity of Biomaterials: A Simultaneous Measurement Technique", *Journal of Biomechanical Engineering*, vol. 99, pp. 148-154, 1977.
- [7] Baker L., "Mathematical function handbook", *McGraw-Hill*, 1992.
- [8] Bendall M. R., "Surface Coil Technology", *Magnetic Resonance Imaging 2nd ed.*, vol.2, pp. 1183-1199, 1988.
- [9] Benoit-Cattin H., Collewet G., Belaroussi B., Saint-Jalmes H., Odet C., "The SIMRI project: a versatile and interactive MRI simulator", *Journal of Magnetic Resonance*, vol. 173, pp. 97-115, 2005.
- [10] Bickley W.G., McLachlan N.W., "Mathieu Functions of Integral Order and their Tabulation", *Mathematical Tables and Other Aids to Computation*, vol. 2, no. 13, pp. 1-11, 1946.
- [11] Blanch G., "On the Computation of Mathieu Functions", *Journal of Mathematics and Physics*, vol. 25, no. 1, 1946
- [12] Blanch G., Clemm D. S., "Mathieu's Equation for Complex Parameters: Tables of Characteristic Values." *Aerospace Research Laboratories*, 1969.
- [13] Blanch G., Rhodes I., "Tables of characteristic values of Mathieu's equation for large values of the parameter", *J. Washington Academy of Sciences*, vol. 45, no. 6, pp. 166-196, 1955.
- [14] Bianchini E., "Studio e progettazione di un sistema di demodulazione digitale per segnali di Risonanza Magnetica.", *Tesi di Laurea Specialistica*, Università di Pisa, 2004.
- [15] Bottomley P. A., Redington R. W., Edelstein W. A., Schenck J. F., "Estimating radiofrequency power deposition in body nmr imaging", *Magnetic Resonance in Medicine*, vol. 2, pp. 336-349, 1985.

REFERENCES(continued)

- [16] Bowman, J. J., Senior T. B. A., Uslenghi P. L. E., "Electromagnetic and acoustic scattering by simple shapes", *New York: Hemisphere Publishing*, 1987.
- [17] Broquetas A., Romeu J., Rius J. M., Elias-Fuste A. R., Cardama A., Jofre L., "Cylindrical geometry: A further step in active microwave imaging", *IEEE Transactions Microwave Theory Tech.*, vol. 39, pp. 836-844, 1991.
- [18] Brunner D. O., Pruessmann K. P., "Optimal design of multiple-channel RF pulses under strict power and SAR constraints", *Magnetic Resonance in Medicine*, vol. 63, pp. 1280-1291, 2010.
- [19] Bussey H. E., Richmond J. H., "Scattering by a lossy dielectric circular cylindrical multilayer, numerical values", *IEEE Transactions Antennas Propagation*, vol. AP-23, pp. 723-725, 1975.
- [20] Caorsi S., Pastorino M., Raffetto M., "Electromagnetic Scattering by a Multilayer Elliptic Cylinder Under Transverse-Magnetic Illumination: Series Solution in Terms of Mathieu Functions", *IEEE Transactions On Antennas And Propagation*, vol. 45, no. 6, 1997.
- [21] Carlson J.W., "Radiofrequency Field Propagation in Conductive NMR Samples", *Journal of Magnetic Resonance*, vol 78, pp. 563-573, 1988.
- [22] Carluccio G., Erricolo D., "Exact analytic 2D solution to obtain optimal B1 excitation field in ultra-high field MRI applications," in *Digest of National Radio Science Meeting*, Boulder, CO, USA, 2008.
- [23] Carluccio G., Erricolo D., "Exact analytic 2D solution to obtain optimal B1 excitation field in ultra-high field MRI applications," in *XXIX General Assembly of the International Union of Radio Science*, Chicago, IL, USA, 2008.
- [24] Carluccio G., Collins C. M., Erricolo D., "A fast algorithm to optimize transmit efficiency for local excitation with a transmit array", in *Proceedings of the 19th Annual Meeting of ISMRM*, p. 3856, Montreal, Canada, 2011.
- [25] Carluccio G., Oh S., Collins C. M., "Ultra-Fast Calculation of SAR-induced Temperature Increase", in *Proceedings of the 19th Annual Meeting of ISMRM*, p. 3844, Montreal, Canada, 2011.
- [26] Chato J. C., "Measurement of Thermal Properties of Biological Materials", *Heat Transfer in Medicine and Biology*, pp. 167-192, 1985.
- [27] Chen W. C., "Waves and Fields in Inhomogeneous Media", *IEEE Press*, 1995.
- [28] Charny C. K., "Mathematical models of bioheat transfer", in *Advances in Heat Transfer*, pp. 19-155.

REFERENCES(continued)

- [29] Cho Z. H., Joie P. J., Manbir S., "Foundations of Medical Imaging", *Wiley-Interscience Publication*, 1993.
- [30] Clemm D. S., "Algorithm 352 Characteristic values and associated solutions of Mathieu's differential equation", *Communication ACM*, vol. 13, no. 12, pp. 399-407, 1969.
- [31] Collins C. M., Liu W. Z., Schreiber W., Yang Q. X., Smith M. B., "Central brightening due to constructive interference with, without, and despite dielectric resonance," *Journal of Magnetic Resonance Imaging*, vol. 21, no. 2, pp. 192-196, 2005.
- [32] Collins C. M., "Calculations of RF Magnetic Fields and SAR Experienced by the Human Body during MRI", *PhD Thesis*, The University of Pennsylvania, USA, 1999.
- [33] Collins C. M., Liu W., Swift B. J., Smith M. B., "Combination of optimized transmit arrays and some receive array reconstruction methods can yield homogeneous images at high frequencies", *Magnetic Resonance in Medicine*, vol. 54, pp. 1327-1332, 2005.
- [34] Collins C.M., Li S., Smith M.B., "SAR and B1 field distributions in a heterogeneous human head model within a birdcage coil. Specific energy absorption rate." *Magnetic Resonance in Medicine*, vol. 40, no. 6, pp. 847-856, 1998.
- [35] Collins C. M., Wang Z., Mao W., Fang J., Liu W., Smith M. B., "Array-optimized composite pulse for excellent whole-brain homogeneity in high-field MRI", *Magnetic Resonance in Medicine*, vol. 57, pp. 470-474, 2007.
- [36] Collins C. M., Liu W., Wang J., Gruetter R., Vaughan J. T., Ugurbil K., Smith M. B., "Temperature and SAR Calculations for a Human Head Within Volume and Surface Coils at 64 and 300 MHz", *Journal of Magnetic Resonance Imaging*, vol. 19, pp. 650-656, 2004.
- [37] Collins C. M., Smith M. B., Turner R., "Model of local temperature changes in brain upon functional activation", *Journal Appl. Physiol*, vol. 97, pp. 2051-2055, 2004.
- [38] DePoorter J., DeWagter C., DeDeene Y., Thomsen C., Stahlberg F., and Achten E., "The proton-resonance-frequency-shift method compared with molecular diffusion for quantitative measurement of two-dimensional time-dependent temperature distribution in a phantom", *Journal of Magnetic Resonance*, vol. 103B, pp. 234-241, 1994.
- [39] DePoorter J., "Noninvasive MRI thermometry with the proton resonance frequency method: study of susceptibility effects", *Magnetic Resonance in Medicine*, vol. 34, pp. 359-367, 1995.
- [40] Dorri B., Vermilyea M. E., "Passive Shimming of MR magnets: algorithm, hardware, and results", *IEEE Transactions Appl. Superconductivity*, vol. 3, no. 1, pp. 131-135, 1985.

REFERENCES(continued)

- [41] Duong T. Q., Yacoub E., Adriany G., Hu X.P., Ugurbil K., Kim S. G., "Microvascular BOLD contribution at 4 and 7 T in the human brain: Gradient-echo and spin-echo fMRI with suppression of blood effects," *Magnetic Resonance in Medicine*, vol. 49, no. 6, pp. 1019–1027, 2003.
- [42] Erricolo D., "Acceleration of the Convergence of Series Containing Mathieu Functions Using Shanks Transformation", *IEEE Transactions On Antennas And Propagation*, vol. 2, pp. 58-61, 2003.
- [43] Erricolo D., "Algorithm 861: Fortran 90 Subroutines for Computing the Expansion Coefficients of Mathieu Functions Using Blanch's Algorithm", *ACM Transactions on Mathematical Software*, Vol. 32, No. 4, pp. 622–634, 2006.
- [44] Farrar T., Becker E., "Pulse and Fourier Transform NMR", *San Diego: Academic Press*, 1971.
- [45] Franklin G. F., Powell J. D., "Digital Control of Dynamical Systems", *Addison-Wesley, California*, 1981.
- [46] Fried M. P., Morrison P. R., Hushek S. G., Kernahan G. A., Jolesz F. A., "Dynamic T1-weighted magnetic resonance imaging of interstitial laser photocoagulation in the liver: observations on in vivo temperature sensitivity", *Laser in surgery and medicine*, vol. 18, pp. 410-4194, 1996.
- [47] Gabriel S., Lau R.W., Gabriel C., "The dielectric properties of biological tissues: II. Measurements in the frequency range 10 Hz to 20 GHz," *Phys. Med. Biol.*, vol. 41, pp. 2251–2269, 1996.
- [48] Gebhardt M., Diehl D., Adalsteinsson E., Wald L. L., Eichfelder G., "Evaluation of maximum local SAR for parallel transmission (pTx) pulses based on pre-calculated field data using a selected subset of "Virtual Observation Points", in *Proceedings of 18th Annual Meeting of ISMRM*, Stockholm, Sweden, 2010.
- [49] Gilbert J. C., Rubinsky B., Wong T. S., Brennan K. M., Pease G. R., Leung P. P., "Temperature determination in the frozen region during cryosurgery of rabbit liver using MR image analysis", *Magnetic Resonance Imaging*, vol. 15, pp. 657-667, 1997.
- [50] Glover G.H., Hayes C.E., Pelc N.J., Eldestein W.A., Mueller O.M., Hart H.R., Hardy C.J., O'Donnell M., Barber W.D., "Comparison of Linear and Circular Polarization for Magnetic Resonance Imaging", *Journal of Magnetic Resonance*, vol. 64, pp. 255-270, 1985.
- [51] Grandolfo M., Vecchia P., Gandhi O. P., "Magnetic resonance imaging: calculation of rates of energy absorption by a human-torso model", *Bioelectromagnetics*, vol. 11, pp. 117-128, 1990.
- [52] Hahn E. L., "Spin Echoes", *Physics Review*, vol. 80, pp. 580-594, 1950.

REFERENCES(continued)

- [53] Hamming R., "Digital Filters", *Prentice-Hall*, 1983.
- [54] Harrington R.F., "Time-Harmonic Electromagnetic Fields", *Wiley-Interscience*, 2001.
- [55] Hayes C. E., "An end-cap birdcage resonator for quadrature head imaging. Work in progress", *5th Annual Scientific Meeting Society of Magnetic Resonance in Medicine*, pp. 39-40, 1986.
- [56] Hayes C. E., Edelstein W. A., Schenck J. F., Mueller O. M., Eash M., "An efficient, highly homogeneous radiofrequency coil for whole-body NMR imaging at 1.5 T", *Journal of Magnetic Resonance*, vol 63, pp. 622-628, 1985.
- [57] Hayt H. William, "Engineering Electromagnetics", Fifth Edition, *McGraw-Hill*, 1989.
- [58] Hestenes, M. R., Stiefel E., "Methods of Conjugate Gradients for Solving Linear Systems", *Journal of Research of the National Bureau of Standards*, 1952.
- [59] Hirata A., Shiozawa T., "Correlation of Maximum Temperature Increase and Peak SAR in the Human Head Due to Handset Antennas", *IEEE Transactions on Microwave Theory and Techniques*, vol. 51, pp. 1834-1841, 2003.
- [60] Hornak J. P., Szumowski J., Bryant R. G., "Magnetic field mapping", *Magnetic Resonance in Medicine*, vol. 6, pp. 158-163, 1988.
- [61] Hornak J.P., "The basics of MRI", 2008 (<http://www.cis.rit.edu/htbooks/mri/>)
- [62] Hoult D., "The principle of Reciprocity in Signal Strength Calculations-A Mathematical Guide." *Concepts in Magnetic Resonance*, vol 12, pp. 173-187, 2000.
- [63] Hoult D., Phil D., "Sensitivity and Power Deposition in a High-Field Imaging Experiment", *Journal of Magnetic Resonance Imaging*, vol 12, pp. 46-67, 2000.
- [64] Huda W., Slone R., "Review of Radiologic Physics", *Williams and Wilkins, Baltimore*, 1995.
- [65] Ibrahim T. S., Lee R., Baertlein B. A., Abdujalil A. M., Zhu H., Robitaille P. L., "Effect of RF coil excitation on field inhomogeneity at ultra high fields: A field optimized TEM resonator", *Magnetic Resonance Imaging*, 19, pp. 1339-1347, 2001.
- [66] Ibrahim T. S., Lee R., Baertlein B. A., Kangaru A., Robitaille P., "Magnetic fields homogeneity and SAR issues for high-field MRI", in *Proceedings of the International Society for Magnetic Resonance in Medicine 6th Annual Meeting Sydney*, p. 2048, 1998.
- [67] Insko E. K., Bolinger L., "Mapping of the radiofrequency field", *Journal of Magnetic Resonance*, vol. 103A, pp. 82-85, 1993.

REFERENCES(continued)

- [68] IEEE Standard C95.3-2002, Annex E, "IEEE Recommended Practice for Measurements and Computations of Radio Frequency Electromagnetic Fields With Respect to Human Exposure to Such Fields, 100 kHz-300 GHz", *IEEE Standards*, 2002.
- [69] International Electrotechnical Commission, "Medical electrical equipment-Part 2-33: particular requirements for the basic safety and essential performance of magnetic resonance equipment for diagnosis, IEC60601-2-33, edition 3.0". *IEC Press*, Geneva, 2010.
- [70] Jin J., "Electromagnetic Analysis and Design", *CRC Press*, 1999.
- [71] Jin J., Chen J., "On the SAR and field inhomogeneity of birdcage coils loaded with the human head", *Magnetic Resonance in Medicine*, vol. 38, pp. 953-963, 1997.
- [72] Joseph P. M., Fishman J. E., "Design and evaluation of a radio frequency coil for nuclear magnetic resonance imaging of fluorine and protons", *Med. Phys.*, vol. 12, pp. 679-683, 1985.
- [73] Kahn T., Harth T., Kiwit J. C. W., Schwarzmaier H., Wald C., Modder U., "In vivo MRI thermometry using a phase-sensitive sequence: preliminary experience during MRI-guided laser-induced interstitial thermotherapy of brain tumors", *Journal of Magnetic Resonance Imaging*, vol. 8, pp. 160-164, 1998.
- [74] Kakogiannos N. B., Roumeliotis J. A., "Electromagnetic scattering from an infinite elliptic metallic cylinder coated by a circular dielectric one", *IEEE Transactions Microwave Theory Tech.*, vol. 38, pp. 1660-1666, 1990.
- [75] Kangarlou A., Baertlein B.A., Lee R., Ibrahim T. S., Yang L.N., Abduljalil A. M., Robitaille E.M.L., "Dielectric resonance phenomena in ultra high field mri," *Journal of Computer Assisted Tomography*, vol. 23, no. 6, pp. 821-831, 1999.
- [76] Katscher U., Bornert P., "Parallel RF transmission in MRI", *NMR Biomed.*, vol. 19, pp. 393-400, 2006.
- [77] Katscher U., Bornert P., Leussler C., van den Brink J. S., "Transmit SENSE", *Magnetic Resonance in Medicine*, vol. 49, pp. 144-150, 2003.
- [78] Krahn A., Priller U., Emsley L., Engelke F., "Resonator with reduced sample heating and increased homogeneity for solid-state NMR", *Journal of Magnetic Resonance*, vol. 191, pp. 78-92, 2008.
- [79] Kress R., "A Comparative Analysis of Thermal Blood Perfusion Measurement Techniques", *Journal of Biomechanical Engineering*, vol. 109, pp. 218-225, 1987.
- [80] Kunz K. S., Luebbers R. J., "The Finite Difference Time Domain Method for Electromagnetics", *CRC Press*, 1993.

REFERENCES(continued)

- [81] Kurpad K. N., Boskamp E. B., Wright S. M., "Implementation of coil integrated RF power MOSFET as a voltage controlled current source in a transmit phased array coil", in *Proceedings of the 12th Annual Meeting of ISMRM*, Kyoto, Japan, p. 1585, 2004.
- [82] Larsen T.M., Erricolo D., Uslenghi P.L.E., New method to obtain small parameter power series expansions of Mathieu radial and angular functions", *Mathematics of Computation*, vol. 78, 2008.
- [83] Lee J., Gebhardt M., Wald L. L., Adalsteinsson E., "Generalized model compression method for peak local SAR estimation", in *Proceedings of the 19th Annual Meeting of ISMRM*, Montreal, Canada, 2011.
- [84] Ljunggren S., "A Simple Graphical Representation of Fourier-based Imaging method", *Journal of Magnetic Resonance*, vol. 54, pp. 338-343, 1983.
- [85] Mathieu E. L., "Memoire sur le mouvement vibratoire d'une membrane de forme elliptique", *Journal de Mathematique Pures et Appliquees (Journal de Liouville)*, vol. 13, no. 137, 1868.
- [86] Mao, W., Smith M.B., Collins C.M., "Exploring the Limits of RF Shimming for High-Field MRI of the Human Head", *Magnetic Resonance in Medicine*, vol. 56, pp. 918-922, 2006.
- [87] Marks R. J., "Handbook of Fourier Analysis and its Applications", *Oxford University Press*, 2009.
- [88] McLachlan, N. W., "Theory and application of Mathieu functions", *Dover Publications, New York*, 1962.
- [89] Metzger G.J., Snyder C., Akgun C., Vaughan T., Ugurbil K., Van de Moortele P. F., "Local B₁⁺ shimming for prostate imaging with transceiver arrays at 7T based on subject-dependent transmit phase measurements," *Magnetic Resonance in Medicine*, vol. 59, no. 2, pp. 396-409, 2008.
- [90] Ogawa S., Lee T. M., Nayak A. S., Glynn P., "Oxygenation-sensitive contrast in magnetic resonance image of rodent brain at high magnetic fields", *Magnetic Resonance in Medicine*, vol. 14, no. 1, pp. 68-78, 1990.
- [91] Oh S., Carluccio G., Collins C. M., "Method and Tool for Improved, Rapid N-gram Average SAR Determination", in *Proceedings of the 19th Annual Meeting of ISMRM*, p. 3868, Montreal, Canada, 2011.
- [92] Oh S., Sylvie G., Collins C. M., "Array-optimized Composite Excitation Pulse for Simultaneous Homogeneous Excitation and Low SAR in a Human-Body Transmit-Array at 3.0 T", in *Proceeding of the 15th Annual Meeting of ISMRM*, Toronto, Canada, 2008.

REFERENCES(continued)

- [93] Park B., "Development of RF Coils and Pulsing Methods for NMR/MRI", *PhD Thesis*, Pennsylvania State University, USA, 2009.
- [94] Pascone R. J., Garcia B. J., Fitzgerald T. M., Vullo T., Zipgan R., Cahill P. T., "Generalized electrical analysis of low-pass and high-pass birdcage resonators", *Magnetic Resonance in Imaging*, vol. 9, pp. 395-408, 1991.
- [95] Pennes H. H., "Analysis of tissue and arterial blood temperature in the resting human forearm", *Journal of applied physiology*, pp. 93-122, 1948.
- [96] Pozar D.M., "Microwave Engineering", *John Wiley & Sons*, 1996.
- [97] Raichle M. E., Mintun M. A., "Brain Work and Brain Imaging", *The Annual Review of Neuroscience*, 2006.
- [98] Richmond J. H., "Scattering by a conducting elliptic cylinder with dielectric coating", *Radio Science*, vol. 23, pp. 309-314, 1965.
- [99] Robitaille P.M., Berliner L., "Ultra High Field Magnetic Resonance Imaging", *Springer*, vol. 26, 2006.
- [100] Robitaille PM, Abduljalil AM, Kangarlu A. "Ultra high resolution imaging of the human head at 8 tesla: 2K x 2K for Y2K.", *Journal of Computer Assisted Tomography*, vol. 24, pp. 2-8, 2000.
- [101] Rosen B., Wald L., Magnetic Resonance Analytic, Biochemical, and Imaging Techniques Course Notes HST.584J, Spring 2006 (<http://ocw.mit.edu/NR/rdonlyres/Health-Sciences-and-Technology/HST-584JSpring-2006/DAC23C7E-D4AE-4706-877A-A7C6AA686933/0/coursenotes.pdf>)
- [102] Saekho S., Yip C., Noll D. C., Boada F. E., Stenger V. A., *Magnetic Resonance in Medicine*, vol. 51, pp. 775-784, 2004.
- [103] Schwan H. P., Piersol G. M., "The absorption of electromagnetic energy in body tissues: a review and critical analysis, *Am. Journal Physics Medicine*, vol. 33, pp. 371-404.
- [104] Shannon C. E., "Communication in the presence of noise", *Proc. Institute of Radio Engineers*, vol. 37, no. 1, pp. 10-21, 1949.
- [105] Shaw D., "Fourier Transform NMR Spectroscopy", *New York: Elsevier Scientific*, 1971.
- [106] Stratton J. A., "Electromagnetic theory", *McGraw-Hil, NewYork*, 1941.
- [107] Stuart C., "Functional MRI : Methods and Applications.", *PhD Thesis*, University of Nottingham, 1997.

REFERENCES(continued)

- [108] Taflove A., Hagness S.C., "Computational Electrodynamics: The Finite-Difference Time-Domain Method", *Artech House*, third edition, 2005.
- [109] Tropp J., "The theory of the birdcage resonator", *Journal of Magnetic Resonance*, vol. B 104, pp. 143-147, 1994.
- [110] Van den Berg C. A. T., van den Bergen B., van de Kamer J. B., Raaymakers B. W., Kroeze H., Bartels L. W., Lagendijk J. J. W., "Simultaneous B₁+ Homogenization and Specific Absorption Rate Hotspot Suppression Using a Magnetic Resonance Phased Array Transmit Coil", *Magnetic Resonance in Medicine*, vol. 57, pp. 577-586, 2007.
- [111] Van De Moortele P.F., Akgun C., Adriany G., Moellerand S., Ritter J., Collins C. M., Smith M.B., Vaughan J. T., Ugurbil K., "B-1 destructive interferences and spatial phase patterns at 7 T with a head transceiver array coil," *Magnetic Resonance in Medicine*, vol. 54, no. 6, pp. 1503–1518, 2005.
- [112] Vaughan T., DelaBarre L., Snyder C., Tian J., Akgun C., Shrivastava D., Liu W., Olson C., Adriany G., Strupp J., Andersen P., Gopinath A., Van de Moortele P.F., Garwood M., Ugurbil K., "9.4 T Human MRI: Preliminary Results", *Magnetic Resonance in Medicine*, vol. 56, pp. 1274-1282, 2006.
- [113] Versluis M. J., Kan H. E., van Buchem M. A., Webb A. G., "Improved Signal to Noise in Proton Spectroscopy of the Human Calf Muscle at 7 T Using Localized B₁ Calibration", *Magnetic Resonance in Medicine*, vol. 63, pp. 207-211, 2010.
- [114] Wang Z., Lin J. C., Mao W., Liu W., Smith M. B., Collins C. M., "SAR and temperature: simulations and comparison to regulatory limits for MRI", *Journal of Magnetic Resonance Imaging*, vol. 26, pp. 437-441, 2007.
- [115] Wlodarczyk W., Boroschewski R., Hentschel M., Wust P., Monich G., Felix R., "Three-dimensional monitoring of small temperature changes for therapeutic hyperthermia using MR", *Journal of Magnetic Resonance Imaging*, vol. 8, pp. 165-174, 1998.
- [116] Yacoub E., Shmuel A., Pfeuffer J., Van de Moortele P.F., Adriany G., Andersen P., Vaughan J. T., Merkle H., Ugurbil K., Hu X. P., "Imaging brain function in humans at 7 tesla," *Magnetic Resonance in Medicine*, vol. 45, no. 4, pp. 588–594, 2001.
- [117] Yang Q.X., Mao W., Wang J., Smith M.B., Lei H., Zhang X., Ugurbil K., Chen W., "Manipulation of Image Intensity Distribution at 7.0 T: Passive RF Shimming and Focusing With Dielectric Materials", *Journal of Magnetic Resonance in Medicine*, vol. 24, pp. 197-202, 2006

REFERENCES(continued)

- [118] Yang Q.X., Wang J., Zhang X., Collins C.M., Smith M.B., Liu H., Zhu X.H., Vaughan J.T., Ugurbil K., Chen W., "Analysis of wave behavior in lossy dielectric samples at high field." *Magnetic Resonance in Medicine*, vol. 47, no.5, pp. 982-989, 2002.
- [119] Yariv A., Yeh P., "Photonics", *Oxford University Press*, 6th ed., 2006
- [120] Yarnikh V. L., "Actual Flip-Angle Imaging in the Pulsed Steady State: A Method for Rapid Three-Dimensional Mapping of the Transmitted Radiofrequency Field", *Magnetic Resonance in Medicine*, vol. 57, pp. 192-200, 2007.
- [121] Yee K. S., "Numerical solution of initial boundary value problems involving Maxwell's equations in isotropic media", *IEEE Transactions Antenna Propagation*, vol. 14, pp. 302-307, 1966.
- [122] Zelinski A. C., Setsompop K., Alagappan V., Gagoski B. A., Angelone L. M., Bonmassar G., Fontius U., Schmitt F., Adalsteinsson E., Wald L. L., "Pulse design methods for reduction of specific absorption of specific absorption rate in parallel RF excitation", in *Proceedings of ISMRM*, p. 1698, 2007.
- [123] Zhang S., Jin J., "Computation of Special Functions", *Wiley, New York*, 1996.
- [124] Zhu Y., "In Vivo RF Power and SAR Calibration for Multi-Port RF Transmission", *Proc. Intl. Soc. Mag. Reson. Med.*, 2009.
- [125] Zhu Y., "Parallel excitation with an array of transmit coils", *Magnetic Resonance in Medicine*, vol. 51, pp. 775-784, 2004.

VITA

Name: Giuseppe Carluccio

Education: Laurea, Ingegneria Elettronica,
Politecnico di Milano, Milano, Italy, 2005

Courses in Philosophy and Human Sciences,
Residenza Universitaria Torrescalla, Milano, Italy, 2005

Courses in advanced Math and Physics for Engineers,
Residenza Universitaria Torrescalla, Milano, Italy, 2005

Laurea Specialistica, Ingegneria Elettronica,
Politecnico di Milano, Milano, Italy, 2010

M. S., Electrical and Computer Engineering,
University of Illinois at Chicago, Chicago, IL, 2011

Ph.D., Electrical and Computer Engineering,
University of Illinois at Chicago, Chicago, IL, 2011

Professional

Experience: Research Assistant,
University of Illinois at Chicago, Chicago, IL, 2007 - 2010

Teaching Assistant,
University of Illinois at Chicago, Chicago, IL, 2008-2011

Staff Engineer,
Pennsylvania State University, Hershey, PA, 2010-2011

Awards: Fellowship "Ti meriti di piu",
Politecnico di Milano, Italy, 2002-2006

Graduate Student Council Travel Award,
University of Illinois at Chicago, Chicago, IL, 2011

Provost and Deiss Award,
University of Illinois at Chicago, Chicago, IL, 2011

VITA (continued)

Journal

Publications:

1. G. Carluccio, D. Erricolo, C. M. Collins, "An Approach to Rapid Calculation of Temperature Change in Tissue Using Spatial Filters to Approximate Effects of Thermal Conduction", in preparation.
2. D. Erricolo, G. Carluccio, "Fortran 90 subroutines to compute Mathieu functions for complex values of the parameter", *ACM Transactions on Mathematical Software*, in preparation.
3. G. Carluccio, C. M. Collins, D. Erricolo, "A Fast, analytically-based method to optimize local transmit efficiency for a transmit array", *Journal of Magnetic Resonance Imaging*, in submission.

Conference

Publications:

1. G. Carluccio, C. M. Collins, D. Erricolo, "A Fast Algorithm to Optimize Transmit Efficiency for Local Excitation with a Transmit Array", in *ISMRM Annual Meeting in Montréal, Québec, Canada, 7-13 May 2011*.
2. G. Carluccio, C. M. Collins, S. Oh, "Ultra-Fast Calculation of SAR-Induced Temperature Increase", in *ISMRM Annual Meeting in Montréal, Québec, Canada, 7-13 May 2011*.
3. S. Oh, G. Carluccio, C. M. Collins, "Method and Tool for Improved, Rapid N-gram Average SAR Determination", in *ISMRM Annual Meeting in Montréal, Québec, Canada, 7-13 May 2011*.
4. G. Carluccio, C. M. Collins, D. Erricolo, "A Fast Algorithm to Optimize Transmit Efficiency for Local Excitation with a Transmit Array", in *Digest of National Radio Science Meeting, Boulder, CO, USA, Jan. 5-9 2011*.
5. S. Oh, G. Carluccio, C. M. Collins, "Method and Tool for Improved, Rapid N-gram Average SAR Determination", in *RF Heating of the Human in MRI workshop, Stillwater, MN, USA, 15-17 Oct. 2010*.

VITA (continued)

6. G. Carluccio, C. M. Collins, D. Erricolo, "A Fast Algorithm to Optimize Transmit Efficiency for Local Excitation with a Transmit Array", in *RF Heating of the Human in MRI workshop*, Stillwater, MN, USA, 15-17 Oct. 2010
7. G. Carluccio, C. M. Collins, S. Oh, "Ultra-Fast Calculation of SAR-Induced Temperature Increase", in *RF Heating of the Human in MRI workshop*, Stillwater, MN, USA, 15-17 Oct. 2010
8. G. Carluccio, D. Erricolo, "2D analytic solution to obtain optimal B1 excitation field in ultra-high field MRI applications", in *Digest of National Radio Science Meeting*, Boulder, CO, USA, Jan. 3-6 2009.
9. G. Carluccio, D. Erricolo, "Exact analytic 2D solution to obtain optimal B1 excitation field in ultra-high field MRI applications," in *XXIX General Assembly of the International Union of Radio Science*, Chicago, IL, USA, 7-17 Aug. 2008.
10. G. Carluccio, D. Erricolo, "Exact analytic 2D solution to obtain optimal B1 excitation field in ultra-high field MRI applications," in *Digest of National Radio Science Meeting*, Boulder, CO, USA, Jan. 3-6 2008.